Biophysical Journal
Article

Biophysical Society

Molecular simulations and NMR reveal how lipid fluctuations affect membrane mechanics

Milka Doktorova,[1,*] George Khelashvili,[2,3] Rana Ashkar,[4,5] and Michael F. Brown[6,7,8,*]

[1]Department of Molecular Physiology and Biological Physics, University of Virginia School of Medicine, Charlottesville, Virginia; [2]Department of Physiology and Biophysics, Weill Cornell Medical College of Cornell University, New York, New York; [3]Institute of Computational Biomedicine, Weill Cornell Medical College of Cornell University, New York, New York; [4]Department of Physics, Virginia Tech, Blacksburg, Virginia; [5]Center for Soft Matter and Biological Physics, Virginia Tech, Blacksburg, Virginia; [6]Department of Chemistry and Biochemistry, University of Arizona, Tucson, Arizona; [7]Department of Physics, University of Arizona, Tucson, Arizona; and [8]Program in Applied Mathematics, University of Arizona, Tucson, Arizona

ABSTRACT Lipid bilayers form the main matrix of functional cell membranes, and their dynamics underlie a host of physical and biological processes. Here we show that elastic membrane properties and collective molecular dynamics (MD) are related by the mean-square amplitudes (order parameters) and relaxation rates (correlation times) of lipid acyl chain motions. We performed all-atom MD simulations of liquid-crystalline bilayers that allow direct comparison with carbon-hydrogen (CH) bond relaxations measured with NMR spectroscopy. Previous computational and theoretical approaches have assumed isotropic relaxation, which yields inaccurate description of lipid chain dynamics and incorrect data interpretation. Instead, the new framework includes a fixed bilayer normal (director axis) and restricted anisotropic motion of the CH bonds in accord with their segmental order parameters, enabling robust validation of lipid force fields. Simulated spectral densities of thermally excited CH bond fluctuations exhibited well-defined spin-lattice (Zeeman) relaxations analogous to those in NMR measurements. Their frequency signature could be fit to a simple power-law function, indicative of nematic-like collective dynamics. Moreover, calculated relaxation rates scaled as the squared order parameters yielding an apparent κ_C modulus for bilayer bending. Our results show a strong correlation with κ_C values obtained from solid-state NMR studies of bilayers without and with cholesterol as validated by neutron spin-echo measurements of membrane elasticity. The simulations uncover a critical role of interleaflet coupling in membrane mechanics and thus provide important insights into molecular sites of emerging elastic properties within lipid bilayers.

SIGNIFICANCE The lipid make-up of a bilayer determines its measurable properties, but how the motions of individual molecules combine to produce these properties remains unclear. By exploiting the synergy between NMR spectroscopy and molecular dynamics (MD) simulations, we show that the lipid dynamics in a bilayer are collective yet segmental in nature and contribute directly to bilayer elasticity. Comparison between MD simulations and NMR entails an improved theoretical framework that allows the two techniques to be directly related. This study provides novel insights into the inner workings of lipid membranes while delivering a new tool for validating computational approaches against experimental data.

INTRODUCTION

Lipid membranes are ubiquitous in biology—they exhibit a large spectrum of physical properties which allows them to serve a multitude of functions (1,2). As the subjects of both experimental and theoretical investigations, they are justifiably of great contemporary interest (3–7). Their rich behavior is enabled by the large diversity of lipid molecules and their distinct mixing properties (8–11). The resulting structural features of the membranes such as bilayer thickness and lipid packing have been studied extensively and are known to influence membrane permeability, elasticity, and protein-membrane interactions (12–17). Lipid molecules also undergo constant thermal motions in the form of orientational fluctuations and segmental dynamics. Viewed in this context, solid-state NMR is one of the few experimental techniques that can detect and quantify these thermal motions at the level of individual lipid molecules (18–23). It is sensitive to the fluctuations of the lipid acyl

Submitted September 3, 2022, and accepted for publication December 2, 2022.

*Correspondence: md4xm@virginia.edu or mfbrown@u.arizona.edu

Editor: Richard Pastor.

https://doi.org/10.1016/j.bpj.2022.12.007

chains, in particular the carbon-hydrogen (CH or deuterium) bonds. By measuring the frequency dependence of bond reorientations, i.e., their power spectrum or spectral density, analysis of the bilayer fluctuations is possible through the combination of NMR lineshape and relaxation time measurements. The NMR lineshape directly reveals the various degrees of motional averaging of the molecules and quantifies the order parameters of the carbons along the lipid chains (24–26). At the same time, measurements of the rate of nuclear spin relaxation of each carbon provide information on correlated CH bond fluctuations over multiple time scales (27).

Currently an extensive body of NMR data points to collective dynamics of the lipid molecules that are linked to bilayer mechanical properties (23). However, these results have been challenged by theoretical arguments stemming from the convoluted nature of the spectral density obtained from NMR relaxation measurements. One approach that has the potential to resolve this dilemma is molecular dynamics (MD) simulations. Indeed, acyl chain order parameter profiles obtained from NMR have been historically used to validate the simulation force-field parameters (7,28–30). These parameters govern the forces exerted on the atoms in an MD simulation that drive their dynamics, rendering comparisons between theory and experiments particularly informative. While NMR-derived order parameter profiles describe the time-averaged structural properties of the lipid molecules (31), the corresponding relaxation measurements hold the key to understanding the connection between local lipid dynamics and bilayer properties (29,32–34). In particular, the CH bond dynamics show both slow and fast motions, but the origins of this emerging hierarchy of motions remain hidden in the data and pose new questions. For example, are they a result of the reorientations of the individual molecules, as detailed by a so-called molecular model, or rather the concerted motions of larger lipid assemblies—in other words, collective dynamics (23,35)? And if the motions are indeed collective, do they resemble those of nematic liquid crystals where the different segments of the lipid chains reorient collectively, or smectic liquid crystals where the identity of the lipids is lost in the dynamical modes of a fluctuating two-dimensional (2D) surface? The answers to these questions will not only illuminate the relationship between lipids and bilayer dynamics but also inform the correspondence of NMR observables with various experimental techniques that measure global bilayer fluctuations, such as flicker spectroscopy (36). Experimentally validated MD simulations thus present an ideal platform for replicating NMR observables and investigating their molecular origins (29,32,37–39).

Here we use molecular simulations to analyze the nature of bilayer dynamics, the relationship between the magnitude of CH bond fluctuations and their relaxation rates, and the resultant elastic moduli as measured with NMR spectroscopy. To facilitate comparison with solid-state NMR data, we first develop a theoretical framework for calculating spin-lattice relaxation rates from the simulations that overcomes shortcomings of existing numerical approaches. The lipid orientational dynamics are considered for in vitro and in silico systems, together with the inherent anisotropic motion of the CH bond fluctuations. For validation, we simulated a set of experimentally well-characterized model membranes composed of 1,2-dimyristoyl-*sn*-glycero-3-phosphocholine (DMPC) and cholesterol (40–42). Using NMR-based protocols, we calculate the spectral densities of the lipid CH bond fluctuations from the simulation trajectories and show they can be modeled by a simple power-law function. Lastly, we evaluate the simulation-derived carbon-specific order parameters and relaxation rates, which we find to follow a square-law dependence related to bilayer elasticity. Our theoretical findings validate and further clarify interpretations of NMR data while presenting a novel approach for calculating bending moduli of simulated bilayers. Importantly, the simulations identify a previously overlooked region of the bilayer where the two leaflets interdigitate that holds a key to membrane mechanics. Our methodology thus opens new avenues for the validation of lipid force fields in terms of underlying theoretical concepts of membrane elasticity for liquid-crystalline bilayers (5,38,43,44).

MATERIALS AND METHODS

Bilayer construction

Bilayers containing DMPC with 0, 20, 33, and 50 mol % cholesterol were constructed with the CHARMM-GUI web server (45–49). Each bilayer contained 100 lipids per leaflet and was hydrated with 45 water molecules per lipid with no added salt. The systems thus ranged from 46,000 to 50,000 atoms.

Simulation protocol

Each system was initially relaxed with the CHARMM-GUI 6-step equilibration protocol using NAMD version 2.12 (50) and the CHARMM36 force field for lipids (29,51). The simulation temperature was set to 317 K (44°C), the same value as used in the cognate experimental studies (34,41,52). This initial equilibration was proceeded with 1 ns of simulation following the CHARMM-GUI simulation production protocol employing a 2-fs time step, 10- to 12-Å Lennard-Jones potential with the NAMD *vdwForceSwitching* option enabled, and *rigidbonds* set to all. The particle mesh Ewald (PME) method was used for treatment of the electrostatic interactions with a grid spacing of 1 Å, and a constant temperature (317 K) and pressure (1 atm) were maintained with a Langevin thermostat and a Nose-Hoover Langevin piston, respectively. The systems were then transferred to the Summit computer cluster at Oak Ridge National Laboratory, where they were simulated for a total of 2 μs each with the OpenMM software (53). These production simulations implemented PME for electrostatic interactions and were performed at a temperature of 317 K under an NPT ensemble with semi-isotropic pressure coupling. The simulation runs utilized a 2-fs time step and Langevin dynamics with a *friction* parameter set to 1.0 per picosecond. Additional parameters included: *EwaldErrorTolerance*, 0.0005; *rigidwater*, True; *constraints*, HBonds; and *ConstraintTolerance*, 0.000001. The van der Waals interactions were calculated applying a

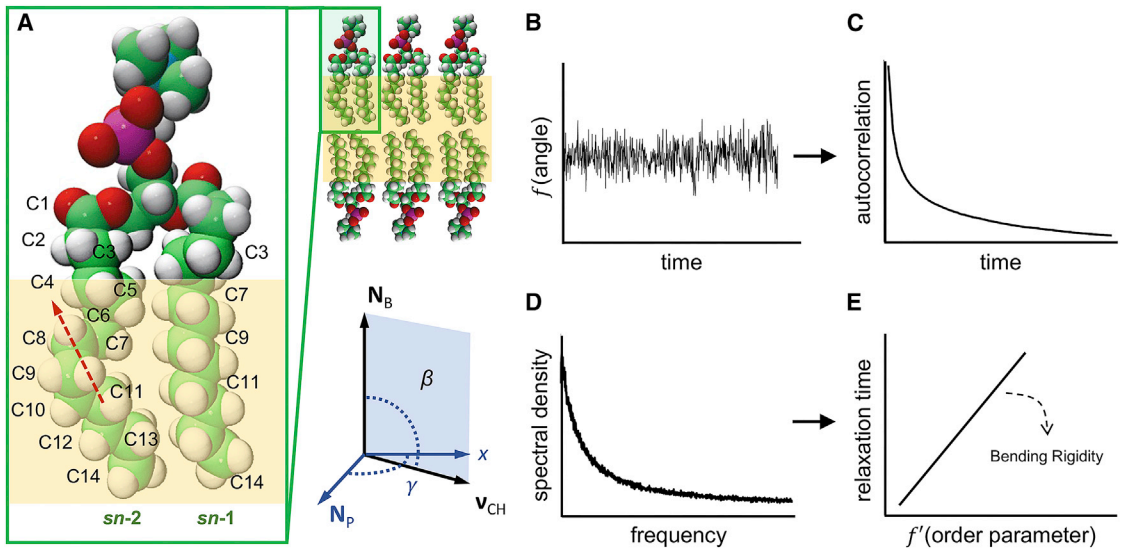

FIGURE 1 Schematic representation of the simulation methodology. (*A*) Lipid bilayer and structure of 1,2-dimyristoyl-*sn*-glycero-3-phosphocholine (DMPC). Labels indicate carbons C3, C7, C9, C11, and C14 on the *sn*-1 chain and all carbons on the *sn*-2 chain of the lipid. Carbon atoms are shown in green, hydrogen in white, oxygen in red, and phosphorus in purple. Red dashed arrow shows a representative local director vector spanning carbons C8 and C11 on the *sn*-2 chain. Yellow shading outlines the part of the lipid chains (in the absence of cholesterol) where the fluctuations of the CH bonds follow a square-law dependence. Shown also is an example of the angle β between a CH bond vector $\mathbf{v}_{CH}$ on the lipid chain and the bilayer normal $\mathbf{N}_B$ (director axis), as well as the angle γ describing rotation of $\mathbf{v}_{CH}$ around $\mathbf{N}_B$. (*B*) Fluctuations of β and γ over time are analyzed to obtain (*C*) their autocorrelation function averaged across all lipids and time. Fourier transformation of the autocorrelation function gives (*D*) the spectral density from which (*E*) the NMR relaxation rate is obtained. Multiple carbon atoms on the lipid chains are used together with their respective order parameters to calculate the bilayer bending modulus. See text for details. To see this figure in color, go online.

cutoff distance of 12 Å and switching the potential from 10 Å. Use of the Langevin integrator for modulating the temperature in the simulations can alter the dynamics of the molecules (i.e., decrease the diffusivity) by introducing friction, which adds artificial thermal noise to the movement of the atoms, as noted in (54). The small 1.0/ps friction used here, however, is expected to have minimal effects on the fluctuations of the CH bonds and, consequently, their calculated relaxation rates.

Simulation analysis

All post-processing analysis was performed with VMD (55), MATLAB, and in-house tcl and MATLAB scripts. Unless otherwise noted, calculations were done on all trajectory frames totaling more than 50,000 with an output frequency corresponding to a 40-ps time step. Each bilayer system was first centered so that in every frame the average position of the terminal methyl carbons of all lipid acyl tails (carbons C14 on the *sn*-1 and *sn*-2 chains, Fig. 1 *A*) was set at $(x,y,z) = (0,0,0)$. The average area per lipid $\langle A_L \rangle$ was calculated by dividing the average lateral area of the simulation box by 100, i.e., the number of lipids in one leaflet, including cholesterol. The acyl chain order parameter (S_{CD}) at each carbon, defined as the second-rank Wigner rotation matrix element $D_{00}^{(2)}(\Omega)$ where $\Omega = (\alpha, \beta, \gamma)$ are the Euler angles (56), was obtained with the formula

$$S_{CD} = \left\langle D_{00}^{(2)}(\Omega) \right\rangle = \frac{1}{2}\left\langle 3\cos^2\beta - 1 \right\rangle, \qquad (1)$$

where $\beta \equiv \beta(t)$ is the time-dependent angle between a CH bond at this carbon and the bilayer normal (i.e., the z-dimension of the simulation box). Likewise, $\Omega \equiv \Omega(t)$ represents the time-dependent Euler angles, and the angular brackets $\langle \cdots \rangle$ denote an ensemble average over all lipids in the bilayer and all trajectory frames.

Calculation of autocorrelation functions from simulation trajectories

Autocorrelation functions of the lipid CH bond fluctuations were calculated from the trajectories as follows (Fig. 1, *A–C*). First, the direction of each $CH_{l,s}^{(n,i)}$ vector in the bilayer was computed as a function of time, where $1 \le l \le N_L$ denotes an individual DMPC lipid, $2 \le n \le 14$ is the carbon number on the *sn*-1 ($s = 1$) or *sn*-2 ($s = 2$) chain, and $i = (1,2)$ is the hydrogen atom. These data were used to calculate three individual time series for each $CH_{l,s}^{(n,i)}$ vector $\mathbf{v}_{CH} = (v_x, v_y, v_z)$, corresponding to the second-rank Wigner rotation matrix elements $D_{0p}^{(2)}(\Omega)$ with $p \in [0, \pm 1, \pm 2]$, as defined in (56):

$$D_{00}^{(2)}(\Omega;t) = \frac{1}{2}\left(3\cos^2\beta(t) - 1\right), \qquad (2)$$

$$D_{01}^{(2)}(\Omega;t) = \sqrt{\frac{3}{2}}\sin\beta(t)\cos\beta(t)e^{-i\gamma(t)}, \qquad (3)$$

$$D_{02}^{(2)}(\Omega;t) = \sqrt{\frac{3}{8}}\sin^2\beta(t)e^{-2i\gamma(t)}. \qquad (4)$$

The other matrix elements are given by the relation $D_{0-p}^{(2)}(\Omega;t) = (-1)^p D_{0p}^{(2)*}(\Omega;t)$ where the asterisk means the complex conjugate (Eq. 4.22 of (57)). In Eqs. 2–4, we have that $D_{0p}^{(2)}(\Omega;t) \equiv D_{0p}^{(2)}(\Omega_{PL};t)$ is a function of the Euler angles $\Omega_{PL} = (\alpha_{PL}, \beta_{PL}, \gamma_{PL})$ describing the transformation from the principal axis system to the laboratory frame (see Fig. S1). From this point on, the subscript PL will be suppressed but implied for brevity, unless otherwise noted. Furthermore, the product of $D_{0p}^{(2)}(\Omega;t)$ and its complex conjugate is invariant to the sign of the projection index

p (i.e., the result is the same regardless of whether the director vectors for the two leaflets point in the same or opposite directions), and therefore we consider only the elements with non-negative p values (see Eq. 12 below and Eq. 4.31 in (57)). The angle $\beta(t)$ is the angle between $\mathbf{v}_{CH}$ and the bilayer normal $\mathbf{N}_B = (0, 0, \pm 1)$ (where $+1$ is for the lipids in the top leaflet and -1 for the lipids in the bottom leaflet) at time t, and $\gamma(t)$ is the time-dependent angle describing the rotation of the $CH_{l,s}^{(n,i)}$ bond with respect to the bilayer normal (see Fig. 1 *A*). Thus, $\gamma(t)$ was calculated (in Cartesian coordinates) as the angle between the normal to the plane defined by the cross product of $\mathbf{v}_{CH}$ and $\mathbf{N}_B$, i.e., $\mathbf{N}_p = \mathbf{v}_{CH} \times \mathbf{N}_B$, and the x-axis of the simulation box $\mathbf{N}_x = (1, 0, 0)$:

$$\gamma(t) = \operatorname{atan2}\left(\left|\mathbf{N}_p \times \mathbf{N}_x\right|, \mathbf{N}_p \cdot \mathbf{N}_x\right). \tag{5}$$

The autocorrelation function of each time series was then obtained as

$$G_{p,l,s}^{(n,i)}(k) = \frac{1}{N_F - k}\left[\sum_{t=0}^{N_F-k-1} D_{0p}^{(2)*}(\Omega; t) D_{0p}^{(2)}(\Omega; t+k)\right] - \left|\left\langle D_{0p}^{(2)}(\Omega)\right\rangle\right|^2, \tag{6}$$

where N_F is the total number of frames and $0 \le k \le N_F/2$ is the lag time (see also Eq. 13 below). Note that the second term on the right in Eq. 6, the square of the mean, vanishes for $p = [1, 2]$ and it is thus nonzero only for the $D_{00}^{(2)}(\Omega)$ matrix element. Furthermore, for the special case of lag time $k = 0$, Eq. 6 becomes the variance of $D_{0p}^{(2)}(\Omega)$, given by

$$G_{p,l,s}^{(n,i)}(0) = \left\langle\left|D_{0p}^{(2)}(\Omega)\right|^2\right\rangle - \left|\left\langle D_{0p}^{(2)}(\Omega)\right\rangle\right|^2 = \operatorname{var}\left[D_{0p}^{(2)}(\Omega)\right]. \tag{7}$$

For every carbon $C_{l,s}^{(n)}$, the autocorrelation function from Eq. 6 was averaged over its two covalently bound hydrogen atoms and all DMPC lipids in the bilayer to yield the autocorrelation function for that carbon atom:

$$G_{p,s}^{(n)}(k) = \frac{1}{2N_L}\sum_l \sum_i G_{p,l,s}^{(n,i)}(k). \tag{8}$$

Theoretical framework for calculation of NMR relaxation rates from molecular dynamics trajectories

The lipid bilayer in the MD simulations corresponds to a membrane patch whose director axis can be assumed to be the average lamellar normal, i.e., a vector parallel to the z-dimension of the simulation box. Hence, the spectral densities of the CH bond fluctuations within this director frame need to first be transformed into the so-called laboratory reference system to correspond to the experimental NMR relaxation rates, which are measured in the presence of a magnetic field (see supporting material and Fig. 4 in (58)). The director-frame spectral density functions, $J_p^{dir}(\omega)$, are Fourier transforms of the correlation functions that characterize the internal motions within the membrane. In an NMR experiment, typically one can assume that the relaxation rates are orientationally averaged, because for the case of lipid multilamellar dispersions the molecules undergo rapid translational diffusion over all director orientations of the curved surfaces during the relaxation ($\approx$50–100 ms and longer). Furthermore, if one assumes unrestricted isotropic motion with a single correlation time (the solution NMR limit), the relaxation rate R_{1Z} simplifies to

$$R_{1Z} = \frac{3}{20}\pi^2\chi_Q^2\left[j(\omega_0) + 4j(2\omega_0)\right]. \tag{9}$$

Here $j(\omega) = 2\tau_C/(1 + \omega^2\tau_C^2)$ is a Lorentzian reduced spectral density where τ_C is the correlation time, χ_Q is the static quadrupolar coupling constant, and $\omega_0 = 2\pi\nu_0$ is the Larmor frequency of the NMR measurement (24,35) (see Eq. S21 and discussion).

However, in a simulation trajectory for a bilayer run with periodic boundary conditions and semi-isotropic pressure coupling, the lamellar normal (director) remains fixed—the assumption for unrestricted isotropic motion and, thus, Eq. 9, does not hold. Instead, to compare the simulation results to the experimental ones, the orientationally averaged but anisotropic spin-lattice relaxation rate needs to be expressed in terms of the director-frame spectral densities (see discussion and supporting material for details of the derivation):

$$R_{1Z} = \frac{3}{20}\pi^2\chi_Q^2\left\{J_0^{dir}(\omega_0) + 4J_0^{dir}(2\omega_0) + 2\left[J_1^{dir}(\omega_0) + 4J_1^{dir}(2\omega_0)\right] + 2\left[J_2^{dir}(\omega_0) + 4J_2^{dir}(2\omega_0)\right]\right\}, \tag{10}$$

where

$$J_p^{dir}(\omega) = \mathrm{Re}\int_{-\infty}^{\infty} G_p^{dir}(t) e^{-i\omega t} dt, \tag{11}$$

and

$$G_p^{dir}(t) = \left\langle\left[D_{0p}^{(2)}(\Omega_{PD}; t) - \left\langle D_{0p}^{(2)}(\Omega_{PD})\right\rangle\right]^* \times \left[D_{0p}^{(2)}(\Omega_{PD}; 0) - \left\langle D_{0p}^{(2)}(\Omega_{PD})\right\rangle\right]\right\rangle. \tag{12}$$

The value of the numerical pre-factor in Eq. 10 is $(3\pi^2/20)(1.70 \times 10^5\ s^{-1})^2 = 4.2785 \times 10^{10}\ s^{-2}$ (see supporting material), and the spectral density $J_p^{dir}(\omega)$ is defined as the two-sided Fourier transform of the correlation function $G_p^{dir}(t)$. The latter decays to a zero value because the fluctuations are expressed relative to the average values of the Wigner rotation matrix elements. The director-frame correlation functions can also be written by subtracting the modulus squared of the average value to read

$$G_p^{dir}(t) = \left\langle D_{0p}^{(2)*}(\Omega_{PD}; t) D_{0p}^{(2)}(\Omega_{PD}; 0)\right\rangle - \left|\left\langle D_{0p}^{(2)}(\Omega_{PD})\right\rangle\right|^2. \tag{13}$$

Note that for a cylindrically symmetric distribution, the last term on the right becomes $\left|\langle D_{0p}^{(2)}(\Omega_{PD})\rangle\right|^2\delta_{0p}$ where δ_{0p} is the Kronecker delta function. For completeness, the orientationally averaged relaxation rates can also be expressed in terms of the spherical-harmonic correlation functions. The equivalent results in terms of the spherical-harmonic correlation functions and spherical-harmonic spectral densities can be found in the supporting material.

Calculation of relaxation rates from the simulation trajectories

Eqs. 10–13 provide the essential framework for calculating the relaxation rates from the simulation trajectories. Note that the autocorrelation function $G_{p,s}^{(n)}(k)$ for the MD simulation trajectories in Eq. 8 is the same as the

correlation function $G_p^{\mathrm{dir}}(t)$ in Eq. 13. We can thus take its discrete Fourier transform to arrive at an expression for the spectral density $J_{p,s}^{(n)}(\omega)$ of the $\mathrm{CH}_s^{(n)}$ bond fluctuations from the simulations:

$$J_{p,s}^{(n)}(\omega) \;=\; \sum_{k\,=\,0}^{(N_{\mathrm{F}}/2)\,-\,1} G_{p,s}^{(n)}(k)\cos\,\omega t_k \Delta t\,. \qquad (14)$$

In Eq. 14 $\omega = 2\pi\nu$ with ν being the Larmor frequency ($\nu = \nu_0$), Δt is the sampling time interval, and $t_k = k\Delta t$ is the time at lag k.

Eq. 14 is a one-sided Fourier transform while the continuous Fourier integral in Eq. 11 goes from $[-\infty, +\infty]$. We therefore need to multiply the former by a factor of two but without overcounting the element at $k = 0$, which thus reads

$$J_{p,s}^{(n)}(\omega) \;=\; 2\left[\sum_{k\,=\,1}^{N_{\mathrm{F}}/2} G_{p,s}^{(n)}(k)\cos\,\omega t_k \Delta t\right] + G_{p,s}^{(n)}(0)\Delta t\,. \qquad (15)$$

As mentioned above, the $t = 0$ element of the correlation function $G_{p,s}^{(n)}(0)$ is the variance of the $D_{0p}^{(2)}(\Omega)$ matrix element (Eq. 7). Accordingly, the second term in Eq. 15 represents a constant equal to $\{\mathrm{var}[D_{0p}^{(2)}(\Omega)]\}\Delta t$ which is added to $J_{p,s}^{(n)}(\omega)$ at every frequency. Estimation of the spectral density from the simulations thus exhibits a strong dependence on the discrete time step Δt (sampling interval). Normally, Δt could be as small as the time step with which atomic coordinates are written out during the simulation if every single frame is used for analysis (in our case $\Delta t = 40$ ps). Alternatively, if every nth frame is used instead, then the sampling time interval would be $n\Delta t$. Note that the simulations are run with a 2-fs time step which puts a lower bound on Δt, but such frequent output is in general impractical for microsecond-long simulations.

Having this Δt-dependent constant would result in an unrealistic shift of the spectral density and, consequently, the relaxation rates. Thus, to remove this apparent dependence on Δt and recover the analytical result in Eq. 11, which is in the limit of $\Delta t \to 0$ (see discussion), we first fit $G_{p,s}^{(n)}(k)$ to a well-defined function, and then use the fit to resample the correlation function at a much smaller $\Delta t_{\mathrm{fit}} \ll \Delta t$. For all CH bonds, the time series of the second-rank Wigner rotation matrix elements from Eqs. 2–4 follow a power law of the form: $ax^b + c$ (see Figs. 2 *A* and S2–S4). We therefore fit $G_{p,s}^{(n)}(k)$ for $k \geq 1$ to a power-law function and use the best fit $G_{p,s,\mathrm{fit}}^{(n)}(k)$ together with the variance $G_{p,s}^{(n)}(0)$ at $k = 0$ to resample the correlation function at a smaller Δt_{fit} interval and recover the spectral density:

$$J_{p,s}^{(n)}(\omega) \;=\; 2\left[\sum_{\hat{k}\,=\,1}^{N_{\mathrm{F,fit}}} G_{p,s,\mathrm{fit}}^{(n)}(\hat{k})\cos\,\omega t_{\hat{k}} \Delta t_{\mathrm{fit}}\right] + G_{p,s}^{(n)}(0)\Delta t_{\mathrm{fit}}\,. \qquad (16)$$

Note that Eq. 16 is calculated at $\omega = c_0 2\pi/T$ (or, equivalently, $\nu = c_0/T$) where $5 \leq c_0 \leq T/(2\Delta t)$ is an integer and $T = \Delta t(N_{\mathrm{F}}/2) = \Delta t_{\mathrm{fit}} N_{\mathrm{F,fit}}$ is the total sampled time of the autocorrelation function in accord with the Nyquist-Shannon sampling theorem. The choice of Δt_{fit} is constrained by the variance of $D_{0p}^{(2)}(\Omega)$ which is the first and largest $G_{p,s}^{(n)}(k)$ matrix element. Therefore, to ensure the smoothness of the reconstructed correlation function, for each carbon $\mathrm{C}_s^{(n)}$ we set Δt_{fit} equal to the minimum value $\Delta t'$ such that $\Delta t_{\mathrm{fit}} = \min(\Delta t')$ where $G_{p,s}^{(n)}(0) \geq G_{p,s}^{(n)}(\Delta t')$. Figs. S5 and S6 show the reconstructed correlation functions and resulting carbon Δt_{fit} values (see discussion).

Accordingly, the theoretical spectral densities $J_{0,s}^{(n)}(\omega)$, $J_{1,s}^{(n)}(\omega)$, and $J_{2,s}^{(n)}(\omega)$ from Eq. 16 are fit to power-law functions of the $ax^b + c$ form. The best fits are then used to calculate the relaxation rate of carbon $\mathrm{C}_s^{(n)}$ following Eq. 10:

$$R_{1Z,s}^{(n)} \;=\; \frac{3}{20}\pi^2\chi_{\mathrm{Q}}^2\left\{J_{0,s}^{(n)}(\omega_0) + 4J_{0,s}^{(n)}(2\omega_0) + 2\left[J_{1,s}^{(n)}(\omega_0) + 4J_{1,s}^{(n)}(2\omega_0)\right] + 2\left[J_{2,s}^{(n)}(\omega_0) + 4J_{2,s}^{(n)}(2\omega_0)\right]\right\}. \qquad (17)$$

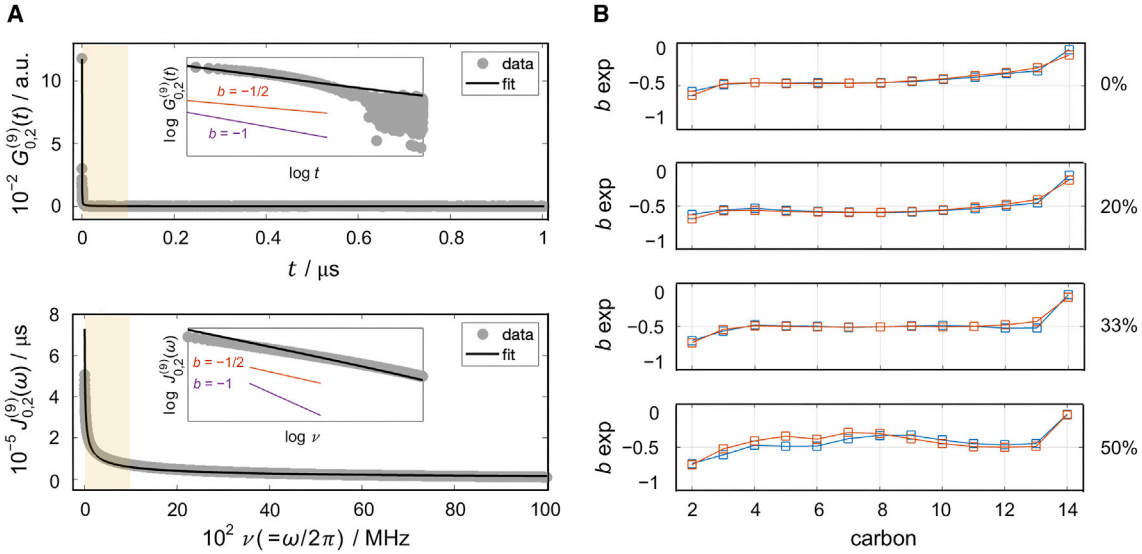

FIGURE 2 Illustration of dynamics of CH bond fluctuations. (*A*) Example of (*top*) autocorrelation function $G_{0,2}^{(9)}(t)$ and (*bottom*) spectral density function $J_{0,2}^{(9)}(\omega)$ for carbon C9 of the *sn*-2 chain of DMPC. The results correspond to fluctuations of the CH bonds as described by the Wigner $D_{00}^{(2)}(\Omega)$ function. Simulation data are shown in gray and best power-law fit to the simulation results in black. Insets show expansion of the data from the highlighted region from 0 to 1000 MHz but in a log-log plot. Shown for comparison are sample functions of the form ax^{-1} (*purple*) and $ax^{-1/2}$ (*red*). (*B*) Power exponents of best fits to the spectral densities $J_{0,s}^{(n)}(\omega)$ for carbons C2–C14 on the *sn*-1 (*red*) and *sn*-2 (*blue*) chains of DMPC with 0, 20, 33, and 50 mol % cholesterol. The power exponents of all carbons in all simulated bilayers are close to −1/2, consistent with collective segmental dynamics. All simulations were performed at 44°C. See text for details. To see this figure in color, go online.

In the above formula $\chi_Q = 170$ kHz, ω_0 is the resonance (Larmor) frequency, and all other symbols are previously defined. The theoretical spectral densities $J^{(n)}_{p,s}(\omega)$ refer to the CH fluctuations with respect to the bilayer normal (director axis) in terms of their mean-square amplitudes (variance) and reduced values. Relaxation rates are averaged over all director orientations to correspond to the actual experimental measurements. Importantly, although the relaxation rates are orientationally averaged, they are not the same as the isotropic solution NMR results found in textbooks. Use of the latter is often assumed but is inapplicable to lipid membranes, because of the underlying assumption that the fluctuations are isotropic, i.e., there is no order parameter. Rather, the CH bond fluctuations must be expressed with respect to the bilayer director and occur with restricted amplitude, as described by their orientational order parameters. Thus, the formula applicable to MD simulations and to the validation of MD force fields based on NMR relaxation is given in Eq. 17. This result is based on group theory principles (35) and is different from that obtained by application of the spherical-harmonic addition theorem (see discussion). Validation of the theoretical and experimental results is further discussed below. Note that the mean-square amplitudes are equal to the area under the spectral density in the region $[0,\infty]$ and they cannot be numerically determined from the integral of $J^{(n)}_{0,s}(\omega)$ due to the finite sampling. Instead the mean-square amplitudes are thought of as the orientational order parameters in terms of a Clebsch-Gordon series expansion (35) and can be calculated from the raw simulation data (i.e., the time series of the Wigner rotation matrix elements from Eqs. 2–4).

Application of NMR-based approach to extract apparent bilayer bending rigidity from molecular dynamics trajectories

An apparent bending modulus κ_C can be extracted from the slope of the theoretically predicted square-law dependence between the relaxation rate R_{1Z} and order parameter S_{CD} of the acyl chain carbons, as derived previously (35). Following the same NMR-based protocol, we obtain κ_C of the simulated bilayers with the formula

$$D = \frac{3k_BT\sqrt{\eta}}{5\pi S_S^2\sqrt{2K^3}}. \quad (18)$$

In Eq. 18 $\eta = 0.1$ Pa·s is the bilayer viscosity, $S_S = 0.6$ is the order parameter estimated for slow motions, $K \approx \kappa_C/t_B$ is an elastic constant related to κ_C and the full bilayer thickness t_B (see below), and D is a constant in units of $s^{1/2}$ which is obtained from the relation:

$$D = \frac{8A\sqrt{\nu_0}}{15\pi^2{\chi_Q}^2}. \quad (19)$$

Here the constant A is the slope of the dependence of R_{1Z} on $|S_{CD}|^2$, χ_Q is the static quadrupolar coupling constant, and $\nu_0 = 76.8$ MHz is the deuterium Larmor frequency. The thickness t_B which is used to obtain K in Eq. 18 represents the full bilayer thickness and is calculated from the number density profile of the bilayer. Specifically, a single number density profile of all bilayer lipid atoms is calculated with the Density Profile plugin of VMD (59) for each system. The profile has two peaks corresponding to the maximum density in the hydrocarbon regions of the two leaflets and decreases to 0 at the ends of the headgroup regions where bulk water begins (see results). The thickness t_B used in Eq. 18 is set equal to the distance between the two tails of the bilayer number density profile where the density drops below 5% of the maximum (peak) density. Table S1 lists the corresponding thicknesses for all simulated bilayers.

The full range of carbons used for the square-law fits in the simulations included C4–C13, C6–C13, C8–C13, and C10–C13 for the bilayers with 0, 20, 33, and 50 mol % cholesterol, respectively. Errors for the κ_C values obtained from the fits were calculated as the standard deviation of the slopes resulting from the best fits to the data after excluding the last 0, 1, or 2 carbon atoms with largest order parameters from each chain. Note that the terminal methyl carbon C14 was also excluded from the fits due to its different geometry.

Splay-fluctuations-based analysis of bilayer bending rigidity

The κ_C modulus can also be obtained in simulations of lipid bilayers from analysis of the fluctuations in lipid splay angles (see (60) and references therein). In brief, the procedure involves calculating the probability distribution of splay angles (i.e., the angles between the local director vectors) of neighboring pairs of lipids within a leaflet and using this distribution to obtain a potential of mean force (PMF) profile. A quadratic function is then fit to the PMF in the region of small deviations from the mean, and the coefficient of the quadratic term is the corresponding splay modulus for that lipid pair. The splay moduli of all lipid pairs are subsequently weighted and summed, revealing the leaflet κ_C value. The bilayer κ_C is then the sum of the κ_C values of the two opposed monolayers. Here, we used the OpenStructure software and algorithm presented in (61,62) to calculate κ_C with an alternative computational method from the splay moduli of DMPC, cholesterol, and DMPC-cholesterol lipid pairs in the simulation trajectories.

Analysis of local director fluctuations

Local director (LD) vectors of different lengths were defined at each carbon along the lipid acyl chains (Fig. 1 *A*). Each LD vector connects the carbon of interest $C^{(n)}_{l,2}$ on the *sn*-2 chain either to another carbon atom $C^{(n-i)}_{l,2}$ further up the chain on the same lipid l toward the lipid headgroup with $1 \le i \le 12$, or to the lipid phosphorus atom P (see results). The fluctuations of the orientations of an LD vector were analyzed in a manner similar to the calculation of the spectral densities described in Eqs. 8 and 15. The only differences are that all angles are defined with respect to the LD vector instead of the CH bond, the denominator in the pre-factor in Eq. 8 is N_L instead of $2N_L$, and because the autocorrelation functions of the LD vector fluctuations do not follow a power law or an exponential function, no fitting and resampling of the correlation was performed. Instead, the spectral density was calculated with Eq. 15 using the sampling interval corresponding to the simulation Δt of 40 ps.

Measurement of bending moduli with neutron spin-echo spectroscopy

To extend the results of the MD simulations and NMR analysis, complementary neutron spin-echo (NSE) measurements were performed on unilamellar vesicles extruded through a polycarbonate filter with 100-nm pore diameter (see supporting material for more details). The NSE data yielded the normalized intermediate scattering function, $I(q,t)/I(q,0)$, for discrete q values within the accessed q range, where t is the Fourier time. For lipid membranes, the probed dynamics follow a stretched exponential function with a stretching exponent of 2/3, such that (63)

$$I(q,t)\,/\,I(q,0) = \exp\left[-(\Gamma(q)t)^{2/3}\right]. \quad (20)$$

Fits of the intermediate scattering functions using the above equation yield the decay rate, $\Gamma(q)$, at individual q values. Plots of $\Gamma(q)$ versus q show the typical q^3 dependence for thermally undulating elastic thin sheets predicted by Zilman and Granek (63). Using theoretical refinements by Watson and Brown (64), based on the Seifert-Langer model (65), allows calculation of a renormalized bending rigidity $\tilde{\kappa} = \kappa + 2h^2k_m$, where h is the height

of the neutral surface from the midplane and k_m is the monolayer area compressibility modulus. Assuming the neutral plane to be at the interface between the hydrophilic headgroups and the hydrophobic tails, these refinements result in a modified expression of the Zilman-Granek decay rates, $\Gamma(q)$, given by (66):

$$\Gamma(q) = 0.0069 \frac{k_B T}{\eta_{sol}} \sqrt{\frac{k_B T}{\kappa}} q^3 . \quad (21)$$

Here, $k_B T$ is the thermal energy and η_{sol} is the solvent (i.e., D_2O buffer) viscosity.

RESULTS

Lipid dynamics at length scales smaller than the membrane thickness resemble nematic liquid crystals

Membrane lipids are known to diffuse rapidly within the plane of a fluid bilayer while their chains explore various rotational degrees of freedom (29,37,67,68). These thermally excited motions are governed by both bonded and nonbonded interactions and can be rather inhomogeneous along the lengths of the lipid chains due to the hydrophobic effect holding the two leaflets together (69). Nuclear spin relaxation measurements show both fast and slow components of the CH bond fluctuations at each carbon (34). Still, because the resulting signal has contributions from all lipids in the bilayer, the origins of this hierarchy of motions, and consequently the nature of the lipid dynamics, need further investigation (27,32,38,39,70). To help address this question, we sought to examine the thermal fluctuations of the CH bonds along the lipid acyl chains with all-atom MD simulations (60,67,71). As a test system we chose DMPC bilayers with increasing amounts of cholesterol that have been well characterized experimentally (34,41,52). In the past, CH bond fluctuations from simulation trajectories have been expressed in terms of spherical harmonics using spherical polar angles (72,73). However, that representation presents certain challenges (see discussion), and we sought to derive a theoretical framework centered around the so-called Wigner rotation matrix elements instead (35,74,75). The latter represent functions (Eqs. 2–4) of the Euler angles describing the CH bond orientation within the lipid membrane, where the angle β is between the CH bond and the bilayer normal and the angle γ is for the rotation of the CH bond about the director (see Fig. 1 and Eq. 5). The autocorrelation function of the time series of each of these functions describes a different relaxation mode of the CH bond fluctuations and was found to follow a power-law dependence (see Fig. 2 *A* and materials and methods). Its Fourier transform yields the spectral density as a function of frequency that can be directly related to the relaxation rates measured experimentally by NMR spectroscopy (Eq. 17).

Importantly, the functional form of the spectral density contains information about the nature of the bilayer dynamics. Each spectral density function calculated from the simulations was found to follow a power-law dependence of the form $y = ax^b + c$ (Figs. 2 *A* and S7–S9). This functional form has been shown to correspond to collective dynamics of the lipids, and its power-law exponent represents the dimensionality of the collective lipid interactions formulated in terms of quasi-elastic order-director fluctuations (ODF) (35). At this level, a continuum of wave-like disturbances with an exponent of -1 indicates 2D smectic-like dynamic undulations (19,75–78) while an exponent of $-1/2$ points to three-dimensional (3D) nematic-like fluctuations (26,35,79). Figs. 2 *B* and S10 show the exponent *b* for all carbons on the *sn*-1 and *sn*-2 chains of the lipids in the simulated DMPC bilayers. As seen in the plots, the power exponents are very close to $-1/2$ throughout both chains in all trajectories. This result suggests that the dynamics of the lipid hydrocarbon acyl tails are collective and yet locally more segmental in nature, resembling the behavior of nematic liquid crystals at distances less than the bilayer thickness (80).

To explore this interpretation further, we compared the fluctuations of the lipid CH bonds with those of LD vectors of varying lengths (Fig. 3 *A*). An LD vector connects a carbon either to another carbon at increasing distance further

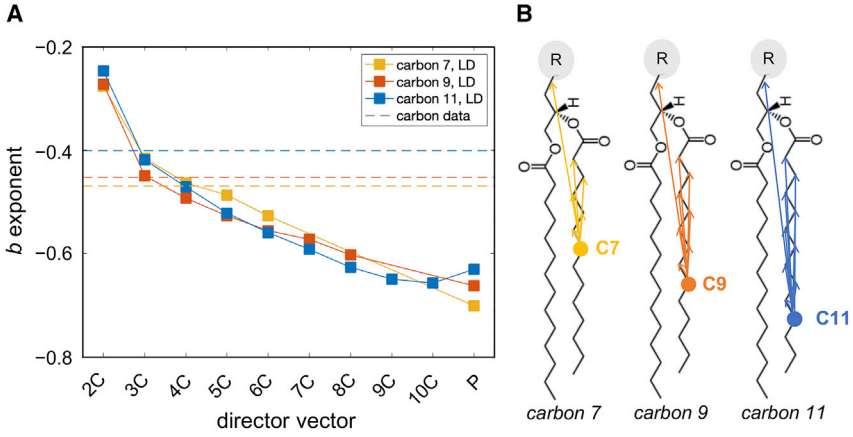

FIGURE 3 Dynamics of local director (LD) vectors connecting two carbons (or a carbon and the phosphate) of a lipid. (*A*) Plotted are the *b*-exponents of the best power-law fits to the spectral densities of LD vectors originating from C7 (*yellow*), C9 (*red*), and C11 (*blue*) carbons on the *sn*-2 chain of DMPC in the cholesterol-free bilayer. The LD vectors are from two (2C) to ten (10C) carbon segments in length or extend all the way to the phosphorus atom (P). Shown for comparison are the exponents of the best power-law fits to the spectral densities of the CH bonds at C7, C9, and C11 carbons (*dashed lines*). (*B*) Schematic of all analyzed LD vectors. The CH bond fluctuations correspond most closely to LD vectors of lengths 3–4 carbons, illustrating the segmental nature of the CH bond dynamics. See text for details. To see this figure in color, go online.

up the chain or to the phosphate atom (*red dashed arrow* in Fig. 1 *A* and *arrows* in the schematic in Fig. 3 *B*). The spectral density of the fluctuations of each LD vector again followed a power law (Figs. S11–S13), where the fits to the power-law function yielded the corresponding *b*-coefficients. Fig. 3 exemplifies the relationship between these *b*-exponents and the lengths of the LD vectors by showing *b* versus length of the director vectors originating from carbons C7, C9, and C11 on the *sn*-2 chain of DMPC (Fig. 1 *A*). As seen from this figure, an increase in the length of an LD vector results in more smectic-like dynamics as the power exponent decreases, eventually approaching a value of approximately −0.7. Yet the motions of the CH bonds resemble most closely those of an LD vector of length 3–4 carbons (compare where the dashed lines cross the corresponding data points in Fig. 3 *A*), in agreement with a model of nematic-like dynamics of relaxation rates and order parameters, as originally proposed (35,80).

Square-law dependence holds for specific carbon atoms

As mentioned earlier, the spectral densities of the CH bond fluctuations of a carbon atom on the lipid chains can be used to calculate the spin-lattice relaxation time R_{1Z} of the bond fluctuations (Eq. 17 and Fig. 1). Various NMR experiments have shown that often in bilayers R_{1Z} is dependent on the square of the order parameter, a rule thus termed the square-law (35,41,81). To understand the molecular origin of this surprising relationship—and test whether it holds in simulated bilayers—we analyzed this trend in our trajectories of DMPC bilayers with increasing amounts of cholesterol (0, 20, 33, and 50 mol %). As expected, the addition of cholesterol made the bilayer more ordered and tightly packed, decreasing the average area per lipid and increasing the bilayer thickness (Fig. S14). From this set of simulations, we calculated the spectral density profiles of the CH bonds along the two chains of DMPC in each trajectory and used them to obtain the corresponding relaxation rates at the NMR deuterium frequency of 76.8 MHz, corresponding to a magnetic field strength of 11.7 T (Eq. 17). Fig. 4 shows the relaxation rates R_{1Z} (see materials and methods) and order parameters for all carbons in the simulated bilayers with 0 mol % and 50 mol % cholesterol, and how the two variables are functionally related to each other. From the corresponding log-log plots (Fig. S15) it becomes apparent that they exhibit a square-law relationship for a subset of the carbon atoms in the lower parts of the chains. In particular, carbons C4 through C13 in the DMPC bilayer without cholesterol and carbons within C6, C8, or C10 through C13 in the DMPC/cholesterol bilayers with 20, 33, and 50 mol % cholesterol, respectively (Figs. 4 and S15) clearly follow the square-law dependence, consistent with the experimental findings (41). The observed behavior is not chain dependent, as we see the same dependence for the *sn*-1 and *sn*-2 chains of the lipids (Fig. S15). Note that the C14 terminal methyl carbons on both chains have a different geometry and are therefore excluded from the analysis.

Interestingly, the square-law in the simulated bilayers breaks down for carbons further up the chain (Figs. 4 and S15). These carbons are schematically illustrated in Fig. 1 *A* and reside at the top part of the acyl groups. To examine in more detail the differences between these carbons and the ones that follow the square-law, we calculated the average position of the carbon atoms relative to the bilayer midplane (Fig. 5 *A*) and compared their number density distributions (Fig. 5 *B*). These data show that regardless of the presence of cholesterol, the carbons that follow the square-law are

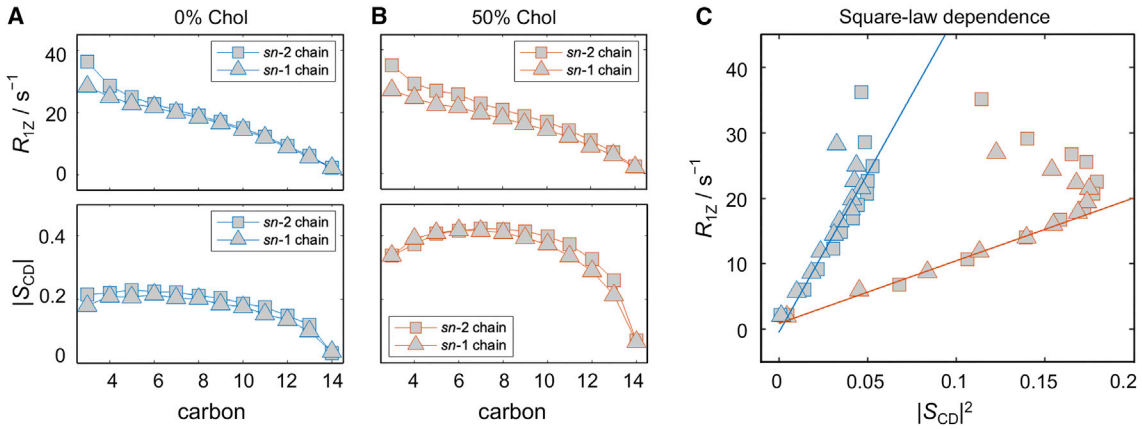

FIGURE 4 Functional dependence of relaxation rates on CH bond order parameters in simulated bilayers. Data are shown for: (*A*) DMPC bilayer in the absence of cholesterol (*blue*) and (*B*) DMPC containing 50 mol % cholesterol (Chol) (*red*). Profiles of spin-lattice relaxation rates (R_{1Z}, top) and order parameters (S_{CD}, bottom) are plotted as a function of carbon position along the *sn*-1 and *sn*-2 chains of DMPC. (*C*) Same data but now replotted as the R_{1Z} relaxation rate as a function of the squared S_{CD} order parameter. Best linear fits to carbons (on both chains) C4 through C13 for 0 mol % cholesterol and C10 through C13 for 50 mol % cholesterol are shown in blue and red, respectively. Carbon atoms outside of these ranges deviate from the linear relationship. Note that the relaxation rates and order parameters exhibit a square-law dependence both with and without cholesterol. All simulations were performed at 44°C. See text for further details. To see this figure in color, go online.

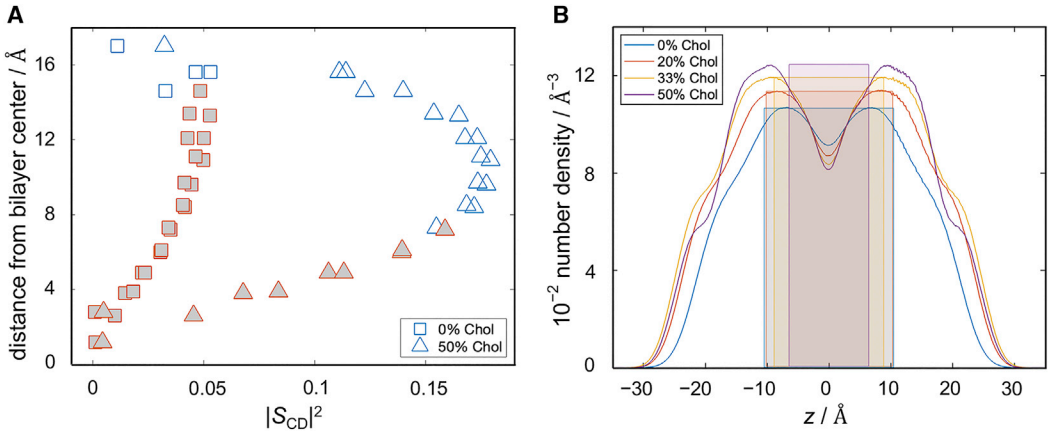

FIGURE 5 Properties of acyl carbons that follow square-law dependence of relaxation rates and order parameters in simulated bilayers. (*A*) Distance from the bilayer center as a function of the squared order parameter $|S_{CD}|^2$ for each carbon in the bilayers with 0 mol % and 50 mol % cholesterol. Filled symbols indicate the carbons used for the square-law fits. (*B*) Number density profiles including all atoms of the simulated bilayers with 0, 20, 33, and 50 mol % cholesterol. Color-coded highlighted areas show the regions of the carbon atoms used in the square-law fits for the corresponding bilayers. The carbons that follow the square-law dependence are within the region where lipid dynamics are influenced by interleaflet interactions. All simulations were performed at 44°C. To see this figure in color, go online.

consistently those in the middle of the bilayer, whose average depth within the membrane falls linearly with their squared order parameters. Stated differently, the relationship between R_{1Z} and $|S_{CD}|^2$ holds precisely for the CH bonds residing within the region of the bilayer sufficiently far from the headgroups where the two leaflets intercalate (Figs. 1 and 5). Thus, the existence of the square-law dependence uncovers the difference between interfacial (i.e., closer to the water-hydrocarbon interface) and noninterfacial (i.e., closer to the bilayer midplane) dynamics. While both are modulated by collective motions, the former are more smectic-like and the latter are more nematic-like in nature. These observations provide a possible explanation for the mechanistic origin of the square-law relationship and why it holds mainly for a subset of carbon atoms in the lipid acyl chains (see discussion).

Bilayer bending modulus emerges from the square-law dependence

It has been previously shown that the square-law dependence, i.e., the linear relationship between R_{1Z} and $|S_{CD}|^2$, is connected to the elastic properties of the bilayer in the liquid-crystalline state (35). In particular, the authors used the slope emerging from the fit of the data to estimate an apparent κ_C bilayer bending modulus. The calculation involved three parameters, namely the bilayer viscosity, the order parameter for slow motions, and a quadrupolar coupling constant, in addition to the bilayer thickness which is proportional to κ_C (see Eqs. 18 and 19). Accordingly, having shown that the square-law holds in our atomistic MD simulations, we followed the same protocol as in (82) to estimate κ_C of the simulated bilayers. Fig. 6 *A* shows the calculated values for R_{1Z} and $|S_{CD}|^2$ for DMPC with 0 mol % and 50 mol % cholesterol from the simulations (*green*), as well as NMR data for the identical systems together with their corresponding best linear fits (*black*). There is a very good agreement between theory and experiment, confirming the ability of the simulations to recapitulate the properties of the experimental model system.

Using previously estimated values of 0.1 Pa·s for the bilayer viscosity, ∼0.6 for the slow order parameter, and 167–170 kHz for the quadrupolar coupling constant (56), as well as the full bilayer thickness (see materials and methods and Table S1), we calculated the corresponding κ_C values as outlined in materials and methods. The resulting bending moduli are shown in Fig. 6 *B* and for DMPC show very good agreement with published values (Table S2). As expected, the apparent bilayer κ_C from the simulations increases with increasing cholesterol concentration, starting at 24.8 ($\pm$1.1) k_BT for the pure DMPC membrane and reaching 79.5 ($\pm$4.5) k_BT at 50 mol % cholesterol. For comparison, we used an alternative computational method to obtain κ_C from the simulation trajectories, namely by analyzing the fluctuations in lipid splay angles as described in detail in (61,62) and summarized in materials and methods. As shown in Fig. 6 *B*, while the absolute values are different, the two computational methods show almost identical trends with cholesterol concentration (Fig. 6 *C*). Plotted in the same figure are also the respective bending rigidities from NMR calculated from the slopes of the experimental data (41) with the same parameters (viscosity, slow order parameter, quadrupolar coupling constant, and thickness) used in the simulations analysis. Not surprisingly, considering the strong agreement of the raw data (Fig. 6 *A*), the NMR results are very close to the simulation ones (Fig. 6 *B*). To obtain an independent experimental validation of the bending moduli, we also used NSE spectroscopy to analyze the thickness fluctuations of extruded

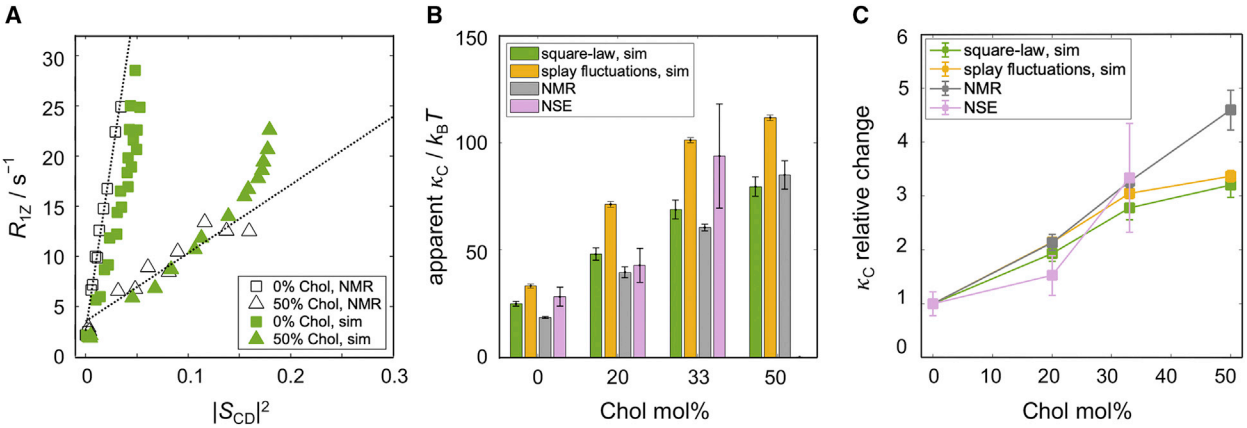

FIGURE 6 Square-law dependence yields an estimate of bilayer bending rigidity. (*A*) Simulation (*green*) and NMR (*black*) data and best square-law fits to the experimental data for DMPC (*squares*) and DMPC containing 50 mol % cholesterol (*triangles*) in the liquid-crystalline state. Experimental data were taken from (41), and simulation data are shown for carbons C4 through C14 for DMPC and C8 through C14 for DMPC/cholesterol. (*B*) Comparison between the apparent bilayer bending modulus κ_C calculated from the square-law relationship (*green*) or splay fluctuations (*yellow*) in the simulations. Shown also are experimental results for κ_C obtained from the square-law relationship of NMR data (*gray*) and from bilayer thickness fluctuations measured with NSE (*purple*). All κ_C values are in units of k_BT. (*C*) Changes in κ_C in the cholesterol-containing bilayers relative to the bilayers without cholesterol. Plotted is the ratio between the two for each of the four methods displayed in (*B*). Errors for the κ_C values obtained from the experimentally determined slope of the square-law relationship were calculated as the standard deviation resulting from the best fits to the data after excluding the last 0, 1, and 2 carbon atoms with largest order parameters. The corresponding errors from the square-law dependence in the simulations were calculated in a similar way (see materials and methods). All simulations were performed at 44°C. The functional dependence between relaxation rates and order parameters is directly related to the bilayer bending rigidity as validated for the full range of cholesterol concentrations. To see this figure in color, go online.

DMPC liposomes with 0, 20, and 33 mol % cholesterol. As shown previously and summarized in materials and methods, these thickness fluctuations are related to the bilayer bending rigidity via the Zilman-Granek theory (63). The results show a very good overall agreement with the computational methods, with a clear stiffening effect of cholesterol (Fig. 6, *B* and *C*). The relative increase in the bending constants estimated for the cholesterol-containing bilayers from the square-law relationship is slightly lower than that given by other methods. This may be due to the assumed constant value for the bilayer viscosity $\eta = 0.1$ Pa·s in Eqs. 18 and 19. However, considering the possibility that cholesterol can increase η even in unsaturated membranes (83) could rectify these differences. Fig. S16 shows the bending moduli for all simulated bilayers for a range of values for η calculated from published estimates for the bilayer viscosity (83,84). Knowing that the bending rigidity obtained from the slope of the square-law relationship is proportional to η, the cholesterol-induced increase in bilayer viscosity would amplify the trends relative to those shown in Fig. 6 *C*. Consequently, the simulated relative rigidity would be closer to the experimental values, confirming the ability of the NMR-based approach to adequately report on the bilayer elasticity.

Frequency dependence of relaxation rates further informs the collective bilayer dynamics

The square-law relationship between the CH bond order parameters and relaxation rates is measured at a particular Larmor frequency (ν_0) (see materials and methods). To ascertain whether the trend is dependent on ν_0, we used the simulation trajectories to analyze the CH bond fluctuations for a range of Larmor frequencies. Fig. 7 shows the results calculated at different ν_0 values for the DMPC bilayer in the liquid-disordered state. Regardless of the specific value of ν_0 the relaxation rates and squared order parameters are linearly dependent, illustrating that the square-law relationship holds for all the accessible frequencies, as seen experimentally (85). At lower frequencies the data are more spread out, while at higher frequencies the deviation from the best fit is smaller. There is also a systematic decrease in the slope with increasing frequency both as expected theoretically and seen experimentally (85). These results demonstrate that the trend encoded by these structural and dynamic aspects of the CH bond fluctuations is not accidental but rather arises from inherent bilayer elastic properties as they emerge from the collective atomic-level interactions of the lipids.

DISCUSSION

It is a universally acknowledged fact that the lipid composition of a membrane affects its structure and function (9,10,83,86–88). However, considerably less is known about the level of cooperativity of the fluctuations of individual lipid molecules that give rise to the emerging bilayer properties. Despite the availability of an extensive amount of biophysical and NMR spectral data, interpretations have remained controversial. We were motivated by the unique

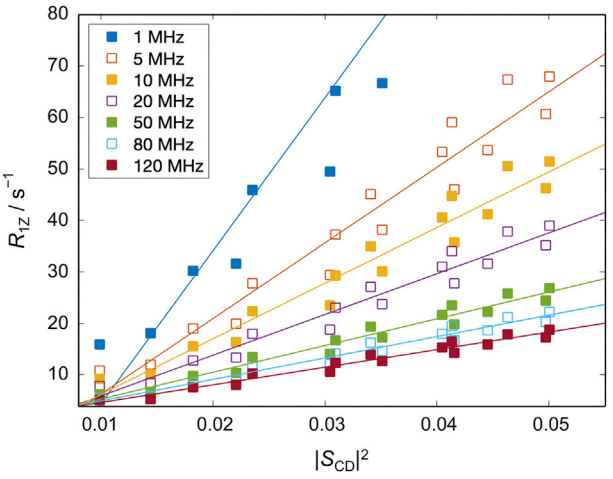

FIGURE 7 Frequency dependence of relaxation rates and order parameters for simulated bilayers. Shown are plots of the simulated ^{2}H NMR relaxation rates of the acyl carbons of DMPC versus the squared order parameters at different Larmor frequencies (ν_0). Data are included for carbons on the *sn*-2 chain of DMPC in the cholesterol-free bilayer in the fluid state. Simulated results are depicted as squares, and lines indicate the corresponding best fits. Note that the slope of the square-law increases with decreasing frequency, consistent with experimental NMR data. The simulation was performed at 44°C. To see this figure in color, go online.

atomistic level information regarding both structure and dynamics offered by the NMR approach, as well as the ongoing need to continuously validate MD force fields with experimental data (7,29). To this end, we used MD simulations to further explore the connection between lipid and bilayer dynamics, and its relation to NMR observables and bilayer elastic properties (5,38). Taking the unique features of the simulations into account, involving the fixed orientation of the bilayer normal, we derived a formulation that allows the simulation results to be directly compared with NMR measurements (34) of multilamellar vesicles (MLVs) as well as small unilamellar vesicles (SUVs) where the bilayer normal can adopt any angle with respect to the laboratory frame (magnetic field). Analysis of the simulation trajectories established the nematic-like behavior of the localized dynamics of the membrane lipids as suggested by NMR, namely their segmental 3D nature modulated by collective lipid dynamics. We saw a clear square-law relationship between the order parameters of the lipid acyl carbon atoms and their respective relaxation rates, in excellent agreement with NMR results (35,85). The atomic resolution of the simulations allowed us to further identify the region in the bilayer where the square-law dependence holds, revealing the importance of interleaflet interactions for the collective dynamics of the lipids. The apparent bilayer bending moduli emerging from the application of an NMR-based formalism to the simulation data are moreover corroborated by an alternative computational method, as well as NMR and NSE experiments (83,88). Our MD simulations thus successfully replicate NMR observables and validate their interpretation while offering new insights about their physical origins.

Theoretical framework for comparing molecular dynamics simulations with NMR measurements

There have been numerous occasions where results from MD simulations of lipid bilayers have been compared with NMR observables, such as acyl chain order parameters of the lipids or relaxation rates due to the underlying fluctuations (7,29,37,39,89). In the case of NMR spectroscopy, the elementary processes occur with correlation times near $1/\nu_0 \approx 10$ ns, even though the relaxation times are in the 10–100 ms regime (weak collision limit) (34,56). Likewise, atomistic MD simulations access the same simulation timescale even though the actual time needed to perform the simulation often differs by many orders of magnitude (so-called wall clock time) (9,60,89). Thus, both NMR spectroscopy and MD simulations entail measurement times that are much longer than the actual processes of interest, in this case the lipid fluctuations, but the results describe the same underlying dynamics. The order parameters depend on a well-defined angle between the CH bond and the bilayer normal, and thus have a straightforward correspondence between the simulations and experiments. Still, the spin-lattice relaxation rate is challenging to compare between the two techniques for the following reasons: 1) there are multiple frame transformations that need to be performed to relate the orientation of a lipid CH bond to the measured relaxation rate (see Fig. 4 in (58)), and 2) NMR measurements are often performed on multilamellar lipid vesicles which have approximately spherical symmetry on average, so that the bilayer normal can adopt any angle with respect to the magnetic field axis. These aspects reside in the liquid-crystalline nature of the membrane lipids and open up the question of how to encapsulate both the lipid structure and dynamics in a fully consistent manner.

The assumption of unrestricted isotropic motion circumvents the above features, and the resulting expression for the relaxation rate simplifies to a function dependent only on a single correlation time τ_C as shown in Eq. 9 and re-derived in the supporting material. In fact, the formula in Eq. 9 (and its equivalent for the carbon-13 relaxation rates) have been the ones used in comparisons of lipid dynamics between simulations and NMR in the past (see, e.g., (32,72,73,90)). In this solution NMR approach a spherical-harmonics representation is often employed, where the CH bond fluctuations are described in terms of changes in their direction over time. The correlation function is thus written as

$$C(t) = \langle P_2[\boldsymbol{\mu}(0)\cdot\boldsymbol{\mu}(t)]\rangle = \langle P_2[\cos\tilde{\beta}(t)]\rangle\,, \qquad (22)$$

where P_2 is the second-order Legendre polynomial (analogous to S_{CD} in Eq. 1) and $\tilde{\beta}$ is the angle between the unit (radius) vectors of the initial and final points. The change

in CH bond orientation is defined by the scalar (dot) product of the unit vector $\boldsymbol{\mu}(0)$ at time zero and the unit vector $\boldsymbol{\mu}(t)$ at time t (Fig. 8 *A*). Fourier transformation of Eq. 22 gives $j(\omega)$, and R_{1Z} is subsequently calculated from the solution NMR result (Eqs. 9, S22, and S23). Note that in the spherical-harmonics representation, the pre-factor in Eq. 9 may look slightly different (see supporting material and Eqs. S22 and S23). One should furthermore recall that Eq. 22 corresponds to the spherical-harmonic addition theorem, i.e., where $\boldsymbol{\mu}(0)\cdot\boldsymbol{\mu}(t) = \cos\tilde{\beta}(t)$ represents one side of a spherical triangle (Fig. 8 *A*) (57). The other sides are the CH bond orientation $\theta(0)$ (at $t = 0$) and the bond orientation $\theta(t)$ (at time t), with $|\phi(t) - \phi(0)|$ as the dihedral angle opposite to the $\tilde{\beta}(t)$ angle. Importantly, the angle $\tilde{\beta}$ in Eq. 22 is different from the Euler angle β in Eqs. 2–4 because $\tilde{\beta}$ is a relative angle independent of the laboratory frame (Fig. 8 *A*). There is no projection axis (index) for the angular momentum, and hence Eq. 22 is applicable to solution NMR spectroscopy. For the case of solution NMR, the isotropic averaging is readily introduced leading to the well-known results in textbooks. For multi-axis or composite motions, the orientational order parameters can then be reintroduced, leading to the so-called model-free approach for proteins in solution (91) as the limit of our generalized approach published concurrently (35). This formulation has been successfully used to compare NMR relaxation results with MD simulations for proteins as well as their lipid anchors (92–95).

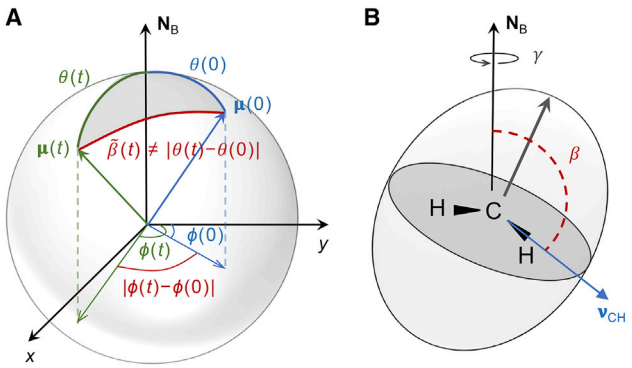

FIGURE 8 Schematic illustration of angles used in different approaches for analyzing CH bond fluctuations from MD simulations. (*A*) Spherical-harmonic representation of the orientation of the CH bond at $t = 0$ and time t described by unit vector $\boldsymbol{\mu}(0)$ and unit vector $\boldsymbol{\mu}(t)$. The corresponding spherical polar coordinates are the polar angles $[\theta(0), \phi(0)]$ and $[\theta(t), \phi(t)]$, respectively. The CH bond angle with respect to the bilayer normal $\mathbf{N}_B$ is $\theta(0)$ or $\theta(t)$. However, the angle $\tilde{\beta}(t)$ whose fluctuations are analyzed with the use of the spherical-harmonic addition theorem (cf. Eq. 22) is different from $|\theta(t) - \theta(0)|$ and does not depend on the director axis. (*B*) Alternatively, the orientation of the CH bond $\mathbf{v}_{CH}$ is described by the Euler angles (α,β,γ). Angles β and γ define the orientation of $\mathbf{v}_{CH}$ with respect to the bilayer normal $\mathbf{N}_B$ (*director axis*), and their fluctuations are analyzed in the new theoretical framework (Eq. 17). The schematic in (*B*) is adapted from (58). Note that use of the spherical-harmonic addition theorem is applicable to isotropic liquids with unrestricted motions, while the representation in terms of Euler angles includes the director axis (*bilayer normal*) and orientational order parameters of the lipids. Analysis of multi-scale composite motions of liquid-crystalline membranes thus becomes possible with the latter approach. To see this figure in color, go online.

On the other hand, lipid membranes are uniaxial liquid crystals in which the fluctuations are expressed in terms of orientational order parameters with respect to the bilayer normal, as shown in Fig. 8 *B* (see also Fig. 1 *A*) (35). Hence, it is incorrect to apply the solution NMR limit to lipids in SUVs, MLVs, or planar supported bilayers. In an NMR experiment with liposomes, the bilayer normal can adopt all orientations with respect to the magnetic field and the CH bond fluctuations consequently might appear unrestricted. However, the CH bond fluctuations are not isotropic but rather anisotropic because of their inherent ordering with respect to the bilayer normal (i.e., their order parameters). That is why the analysis of solid-state NMR data assumes orientational averaging (the bilayer director can adopt all angles) but still retains information about the underlying ordering of the bonds (see supporting material). In simulations of bilayer patches, the bilayer normal is fixed but the CH bond dynamics are analogous to those in the liposomes measured experimentally with NMR spectroscopy. To connect the two approaches, we therefore derived an expression for the orientationally averaged relaxation rates, but in terms of the director frame, i.e., with respect to the local frame described by the bilayer normal (Eqs. 10 and 17). Stated differently, we take the simulation relaxation rates and then orientationally average them to compare them directly with the experimental ones. Note that Eq. 10 for the orientationally averaged relaxation rate has an equivalent formulation in terms of spherical-harmonic spectral densities (see Eq. S17). Importantly, the formulas presented here account for both the fixed bilayer normal in the simulations and the restricted anisotropic motion of the CH bond fluctuations described by segmental order parameters. They should thus be used instead of the solution NMR limit to compare simulation data with experimental NMR results.

To explicitly demonstrate the differences between the two theoretical approaches, i.e., using the spherical-harmonic addition theorem with Eq. 22 versus the Wigner rotation matrix elements and Eqs. 16 and 17, we followed (72) to calculate the ^{2}H NMR relaxation rates corresponding to the commonly used solution NMR limit. In particular, the spectral densities $\tilde{J}(\omega) \equiv \langle \tilde{J}_m(\omega) \rangle$ were obtained from the discrete one-sided Fourier transform of the correlation function using Eq. 22, which gives

$$\tilde{J}(\omega) = \int_0^\infty \langle C(t)\rangle \cos\,\omega t \mathrm{d}t = \sum_{t=0}^{(N_F/2)-1} \langle C(t)\rangle \cos\,\omega t \Delta t\,, \tag{23}$$

where $\langle C(t)\rangle$ is the orientational average of Eq. 22, i.e., the correlation function averaged over all bilayer orientations with respect to the laboratory frame. The relaxation rates

were then calculated with Eq. 2.5 of (72) (also re-derived as Eq. S21 in supporting material):

$$R_{1Z} = \frac{3}{40}\tilde{\chi}_Q^2 \left[\tilde{j}(\omega_0) + 4\tilde{j}(2\omega_0)\right], \tag{24}$$

where the pre-factor in Eq. 24 is $(3/40)\tilde{\chi}_Q^2 = (3/40)(2\pi\chi_Q)^2 = (3/40)(4\pi^2)(1.70 \times 10^5\ s^{-1})^2 = 8.5570 \times 10^{10}\ s^{-2}$. Accordingly, Fig. 9 shows the results from Eq. 24, noted as solution NMR, together with the results from Eq. 17, designated as solid-state NMR and the experimental data (cf. Fig. 6 *A*). The solution NMR relaxation rates (*solid red symbols*) clearly deviate from the solid-state NMR data (*solid green symbols*), and the deviation is larger for the more ordered bilayer with 50% cholesterol. This result illustrates the underlying assumption behind Eq. 24 that the fluctuations are isotropic, so that there is no order in the system, which is incorrect. Thus, when the order parameter is lower the two approaches are more alike, but when the order parameters are larger the differences become more pronounced.

What is more, Fig. 9 shows also how the solution NMR approach suffers from the same sampling problem due to the discrete Fourier transformation as the solid-state NMR approach (see below). At $t = 0$ the correlation function from Eq. 22 is $C(0) = 1$ and when the integral in Eq. 23 goes from 0 to ∞, this results in a large shift in the spectral density and, correspondingly, the relaxation rates (*open red symbols*). If instead the element at $t = 0$ is ignored, and the integral in Eq. 23 is evaluated from $t = \Delta t$ to ∞, the relaxation rates are closer in absolute value to the experiment. Note that the shift due to the $C(0)\Delta t$ term in Eq. 23 at $t = 0$ increases the magnitude of the relaxation rates but does not affect the slope of the square-law relationship, because $C(0) = 1$ for all carbons on the lipid chains. In contrast, in Eq. 15 $G_{p,s}^{(n)}(0)$ is the mean-square amplitude or variance of the Wigner rotation matrix elements, which is different for the various carbon atoms due to their inequivalent order parameters (Fig. S14). Consequently, ignoring the element at lag time $t_k = k\Delta t = 0$ in Eq. 15 would change not only the magnitude of the R_{1Z} values but also the slope of the square-law relationship. This aspect must be recognized in any validations of MD simulations or their force fields versus actual experimental NMR data.

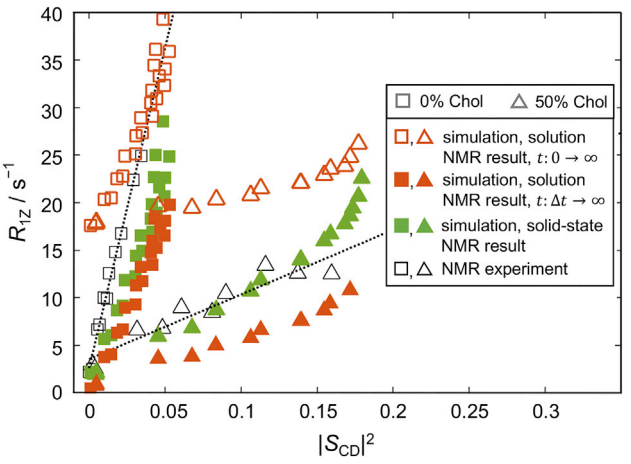

FIGURE 9 Comparison of relaxation rates from MD simulations calculated with different approaches. Shown are results from the solution NMR limit (Eqs. 22–24) (*red*), the new framework (Eq. 17) (*green*), and experiments (*black*). Open and solid red symbols correspond to the relaxation rates calculated from the discrete Fourier transform of the correlation function $C(t)$ by integrating either from $0 \rightarrow \infty$ or from $\Delta t \rightarrow \infty$, respectively (Eq. 23). All simulations of DMPC with 0 mol % and 50 mol % cholesterol (Chol) were performed at 44°C. Quantitative agreement between the simulation and experimental relaxation rates requires consideration of both the sampling interval and whether the solution NMR or solid-state NMR limit is used. See text for details. To see this figure in color, go online.

The nature of lipid dynamics in biomembranes

The spectral densities of the acyl chain CH bond fluctuations hold the key to the types of motions that the lipids exhibit while interacting with other lipids in a bilayer. It was recently shown that these spectral densities (calculated using the NMR solution limit described above) can be fit to a large sum of exponential functions (68). While the respective fits are very good, likely due to the large number of fitting parameters, the results point to an extensive hierarchy of motions with unclear origins, i.e., very fast dynamics modulated by slightly slower dynamics, modulated by yet slower dynamics, and so on. Alternatively, it is shown here that the spectral densities corresponding to the NMR measurements can instead be adequately fit to a simple power-law function that has a clear physical interpretation pertaining to the nature of the underlying motions. The value of the single relevant parameter, the power exponent, indicates the degree of cooperativity of the lipid motions. For all carbons on all chains of the bilayers in the present study, we find the exponent to be around $-1/2$ (Figs. 2 *B* and S7–S9) consistent with collective segmental dynamics. This observation is further confirmed by comparison of the respective power exponents to those of LD vectors of varying lengths, whose orientations with respect to the bilayer normal fluctuate due to the thermal energy (Figs. 3 and S10). Regardless of which carbon the LD vectors originate from, their exponents decrease in an almost identical way with increasing vector length, illustrating the physical interpretation of the origins of this exponent: nematic-like motions at a value around $-1/2$, and smectic-like dynamics at a value approaching -1 as the limit. Our results therefore are a direct manifestation of Occam's razor and show how the seemingly complex interplay between the lipid bond fluctuations is governed by a simple principle of segmental cooperativity.

Quantum-mechanical view of the square-law dependence

Our simulations confirm the existence of the square-law dependence in simulated bilayers, in excellent agreement

with NMR results for in vitro model lipid membranes. While we can distinguish two distinct regions of the lipid chains where this relationship holds and where it breaks (Figs. 4, 5, and S15), the question remains as to the origins of this initially surprising functional correspondence between the order parameters and relaxation rates (35). Notably, the fluctuations of the CH bonds of a lipid reflect the changes in the energy of the atomic nuclei due to their magnetic or electric coupling to their surroundings. Such energy fluctuations result in transitions between different nuclear spin energy levels. The main energy levels of a nucleus in an NMR experiment are determined by the applied magnetic field (Zeeman effect), where transitions between these main energy levels (whose rate is quantified by R_{1Z}) are enabled by additional energy perturbations due to the interactions of the nucleus with its surroundings. Weak coupling to the surroundings results in slower and less efficient relaxation, while strong coupling gives rise to much faster relaxation rates. Thus, the rate of the relaxation depends on the strength of the energy perturbations near the resonance ν_0 frequency. The transition probability between two main energy states is found to be proportional to the product of the squared matrix element of the perturbation and the density of states, according to Fermi's golden rule. In the case of the fluctuating CH bonds, the matrix element is analogous to the mean-squared amplitude of the fluctuations, i.e., corresponding to the square of the segmental order parameter. Together with the square-law dependence, the NMR data show an additional dependence on inverse frequency in the form of a $\nu_0^{-1/2}$ factor that multiplies or scales the squared order parameter (which is why this term appears in Eq. 19). Because the latter is analogous to the density of states in the original formulation, the square-law relationship becomes a direct manifestation of time-dependent perturbation theory and Fermi's golden rule in spectroscopy.

Bilayer elastic properties emerging from the region of interleaflet contact

The presence of the square-law dependence shows clearly that the motional rates of lipid bond fluctuations are functionally related to their mean-squared amplitudes. Here we demonstrate that the relationship yields an estimate of the bilayer bending modulus (Fig. 6 and Table S2). The derivation relies on a single elastic constant approximation, i.e., there is no special treatment of specific deformation modes (e.g., splay, tilt, twist) as they are all approximated with a single parameter. While this formulation cannot distinguish the contribution of particular molecular motions to the membrane deformation, it is simple and general—the fact that it successfully captures both the values and trends in the bending constants makes it an advantageous descriptor of the inherent bilayer elasticity.

Notably, we find from our MD simulations that the collective nematic-like dynamics at the region of direct contact between the two leaflets are closely related to the bilayer bending elasticity, while outside of this region they are not (Fig. 6). This finding is unlikely to arise from simulation artifacts because: 1) available NMR data for the square-law dependence do not clearly resolve carbon atoms in the upper segments of the lipids (plateau region of order profile), and therefore it is unclear whether the bonds of these atoms follow the same dependence as in vitro systems; and 2) there is no difference in the agreement between order parameters for the upper and lower lipid chain segments obtained from NMR and the MD simulations (e.g., Fig. 10). Instead, this intriguing observation complements the relation between local thickness fluctuations in this same mid-bilayer region and the local monolayer area compressibility modulus recently reported (71). The height fluctuations of the carbon atoms inside the region of leaflet-leaflet contact were found to be decoupled from the interfacial dynamics, and the thickness fluctuations of that particular bilayer slab separately yielded the apparent area compressibility moduli of the two leaflets (71). Moreover, outside of this mid-bilayer region, extensive analysis of a large set of simulated lipid bilayers has likewise revealed a strong correlation in the height fluctuations of all carbon atoms, suggesting a direct influence of interfacial tension (occurring at the water-hydrocarbon interface) on their dynamics (Fig. 1 in (71)).

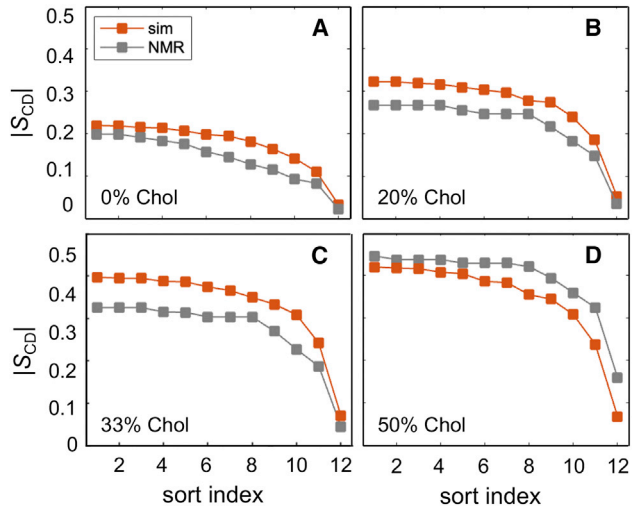

FIGURE 10 Comparison of DMPC order profiles obtained from simulations and NMR spectroscopy. Acyl chain order parameters are shown for DMPC bilayers containing (*A*) 0 mol %, (*B*) 20 mol %, (*C*) 33 mol %, and (*D*) 50 mol % cholesterol. The results are plotted as a function of sort index (i.e., in descending order) either calculated from simulations (*red*) or reported from NMR (*gray*). Simulation data are average from the two chains. Experimental data were taken from (34) with the 0 mol % cholesterol values interpolated from the data at 30°C, 50°C, and 60°C. All simulations were performed at 44°C. Validation of lipid force fields with NMR data requires consideration of both order parameters and relaxation rates. See text for details. To see this figure in color, go online.

The existence of two functionally decoupled bilayer regions can then be explained by variations in the conformational dynamics of the lipid chains along the bilayer normal. In particular, since the chains are effectively tethered to the aqueous interface, their extent (travel) along the bilayer normal (director) depends on the numbers of *gauche* versus *trans* isomers. The more *gauche* isomers, the shorter the chain extension along the director and vice versa. However, the 3D volume must still be occupied, and hence the shorter chain extensions must be compensated by greater disorder of the surrounding chains (96) to fill the volume at liquid hydrocarbon density (80). Accordingly, we propose that the bilayer can be subdivided into two regions (Fig. 1 *A*). The outermost bilayer region corresponds to the so-called plateau of the NMR order parameter profiles (56), coming from the top part of the chains where backfolding and interleaflet penetration are minimal. In contrast, the innermost or mid-bilayer region is where the chain terminations become appreciable and the segmental disorder reaches a maximum (71,96). To a first approximation, we can then consider the outer and mid-bilayer regions separately for the analysis of bilayer mechanics.

Emerging within the mid-bilayer region, the thickness and lipid chain CH bond fluctuations have a hitherto unrecognized connection to the elastic moduli of the membrane. An intricate relationship exists for both bending and compressibility between the noninterfacial segmental dynamics modulated by interleaflet coupling and the energy to locally bend or stretch the bilayer. These mechanical constants have been traditionally obtained from global bilayer properties (e.g., thermal vesicle shape fluctuations or response to induced out-of-equilibrium deformations, flicker spectroscopy) in terms of underlying theoretical concepts of membrane elasticity (5,38,43,44,97). This analysis treats the membrane as a 2D flexible surface (a thin sheet) that exhibits smectic-like dynamics at longer length scales. In addition, our results point to an alternative contribution from the more localized nematic-like lipid dynamics at the bilayer midplane, which appear to have a major role in the observed elastic behavior at shorter length scales. Both approaches at the global and more local scales have been shown to yield similar results for some bilayers (e.g., saturated lipids with and without cholesterol) but contradictory results for other types of bilayers (e.g., di-unsaturated lipids with cholesterol (83)). The sources of these discrepancies may lie in the timescales and length scales of the underlying dynamics (83,88) and are the subject of ongoing debate.

Validation of molecular dynamics simulations with experimental NMR data

As discussed above, the proper comparison between relaxation rates obtained from NMR and calculated from MD simulations requires special considerations which are included in the theoretical framework presented here. The new formulation allows us to comment on a few key points pertaining to theoretical MD simulations and experimental NMR relaxation studies. Here we recall that the simulation data are always discrete in nature; that is, the atomic coordinates are collected at some fixed time sampling interval ($\Delta t > 0$). As a result, calculation of the spectral densities is inevitably done via a discrete (one-sided) Fourier transform of the correlation function (Eq. 15). This discrete transformation as illustrated in Eq. 15 produces a constant equal to the product of the autocorrelation at zero lag time (which is the variance of the data, $\mathrm{var}[D_{0p}^{(2)}(\Omega)]$ from Eq. 7) and the Δt sampling interval. This constant is added to the spectral density at every frequency, and consequently it shifts the calculated relaxation rates in a Δt-dependent manner as an inevitable result of the discrete Fourier transform. Theoretically, the spectral density goes to infinite frequency, and its integral is equal to $\mathrm{var}[D_{0p}^{(2)}(\Omega)]$ as can also be obtained from the second- and fourth-order Legendre polynomials ($\langle P_2 \rangle$ and $\langle P_4 \rangle$) via a Clebsch-Gordan series expansion (see Table V in (75)). Analytically, in the Fourier time domain, the correlation function goes to zero Δt and $\mathrm{var}[D_{0p}^{(2)}(\Omega)]$ equals the initial value. However, that limit is impossible to reach either in simulations or experiments—therefore, we can only access a small window or bandwidth of the spectral density in the Fourier space.

Even then, we managed to alleviate the dependence on the discrete sampling interval Δt by taking advantage of the fact that the correlation functions of the CH bond fluctuations, expressed in terms of the second-rank Wigner rotation matrix elements, follow a power-law relation. As explained in materials and methods, this approach allowed us to fit the correlation functions and use the best fits to resample them at smaller time intervals. Correspondingly, we found the smallest Δt_{fit} that preserved the smoothness of the correlation function for each carbon, as shown in Fig. S6. These Δt_{fit} values correspond to the fastest rotations of the CH bonds that contribute to the spectral density and are in the range of 0.5–30 ps. The results are in excellent agreement with the 5- to 20-ps correlation times predicted to arise from the bilayer microviscosity and account for the apparent enhancement in relaxation of lipid bilayers versus hydrocarbon fluids as measured with NMR spectroscopy (23,80). If a larger sampling time step were used (such as 40 ps due to the output frequency in our simulations), it would effectively mask these rapid bond rotations, while an output frequency corresponding to the femtosecond regime would be impractical for long MD simulations. Mathematical tricks for resampling of the correlation functions are thus necessary to help bridge the gap between the discrete and continuum representations, although an exact correspondence can never be achieved.

Another important observation from our analysis is that the square-law dependence can be used in a model-free

way, as illustrated by Fig. 6 *A*, to validate lipid force fields against NMR relaxation data. While the order parameters contain information about the average structure of the lipid chains—and therefore provide a static picture of their conformations—the spin-lattice relaxation rates describe the CH bond dynamics that produce these conformations, thus complementing the structural data. To substantiate this point, Fig. 10, *A–D* shows a comparison between the theoretically simulated and experimental order parameter profiles for DMPC with various mole fractions of cholesterol. Although the DMPC lipids in the presence of 0, 20, and 33 mol % cholesterol in the simulations are more ordered than in the experiment, both theory and experiment are in remarkable agreement in that we see smaller slopes of their square-law dependences corresponding to higher effective bending rigidities of the simulated bilayers (Fig. 6 *B*). This feature is expected from the known dependence of κ_C on lipid packing (and, consequently, order): the more disordered the lipids the lower the κ_C value (60,83). Interestingly, the simulated bilayer with 50 mol % cholesterol has slightly lower order parameters than the NMR measurements, and its square-law slope matches closely the experimental one for carbons C10 through C14 (cf. Fig. 6 *A*). Therefore, while the overall trends in the deviations from experimental data are similar across the order parameters and relaxation rates, there may be differences from the ability of the force fields to capture the elasticity of the bilayer or its average structure, thus highlighting a path forward toward their improvements. For this to occur, the validation of lipid dynamics in the form of CH bond relaxation rates, as measured with NMR, becomes critical.

Lastly, it is worth noting that simulations are often validated against experimental data where differences in the types of samples and analysis for the various techniques may produce seemingly contradictory structural and/or dynamical features. One example is the recently reported problem in the lack of correspondence between the order parameters of sphingomyelin bilayers obtained from NMR and the bilayer structural properties (area per lipid and thickness) obtained from small-angle scattering techniques (6). Because the analysis of any experimental data adds another set of variables to its interpretation, a model-free comparison of the raw data is always optimal for a bias-free comparison. However, whenever there is a mismatch in the structure resolved by two approaches, the simulated system will inevitably fail to reproduce certain experimental observables.

CONCLUSIONS

Experimentally observed relationships between the relaxation rates of CH bond fluctuations and their order parameters or the frequency at which they are measured have raised questions about the cooperativity of lipid motions in a bilayer and their link to membrane elasticity. We have shown here that the local movements of the lipid acyl chains in the region of interleaflet contact are captured by MD simulations that are indicative of collective segmental motions analogous to nematic liquid crystals. For this, we developed a new theoretical framework that allows direct comparison of the relaxation rates calculated from the simulations with those measured with NMR experiments by accounting for the inherent differences between the two approaches. Following an NMR-based formalism for liquid-crystalline bilayers, we found that the square-law dependence between the rate and amplitude of the lipid CH bond fluctuations yields a frequency-independent estimate of an apparent bilayer bending modulus, which for DMPC bilayers follows the expected trends with addition of cholesterol. Our results are fully in line with NMR observables and their interpretation and offer an alternative protocol for extracting mechanical properties of the simulated membranes. In the future, it will be interesting to explore whether our analysis is applicable to bilayers with mono- and polyunsaturated lipids, as well as more complex lipid mixtures in terms of establishing the universality of bilayer functional properties.

SUPPORTING MATERIAL

Supporting material can be found online at https://doi.org/10.1016/j.bpj.2022.12.007.

AUTHOR CONTRIBUTIONS

M.D. and M.F.B. developed the concept and designed the research. G.K. produced the simulation trajectories and M.D. performed all computational analysis. R.A. performed the NSE experiments, including data collection and analysis. M.D., G.K., R.A., and M.F.B. wrote and edited the manuscript.

ACKNOWLEDGMENTS

Klaus Gawrisch is acknowledged with gratitude for sharing his eternal insight and friendly collegiality over the years. We thank Steven Abel, Frederick Heberle, Kayla Sapp, and Alexander Sodt for helpful advice and insightful discussions on the Fourier analysis of time autocorrelation data from the simulations. We also gratefully acknowledge Andrew Erly and Trivikram Molugu for valuable discussions on the interpretation of simulation results. M.D. was supported by NIH postdoctoral fellowship F32GM134704. R.A. acknowledges NSF support through grant MCB 2137154. G.K. is supported by the HRH Prince Alwaleed Bin Talal Bin Abdulaziz Alsaud Institute of Computational Biomedicine at Weill Cornell Medical College through the 1923 Fund. M.F.B. acknowledges NIH support through grant R01EY026041 and NSF through grants MCB 1817862 and CHE 1904125. Access to the NGA-NSE beamline was provided by the Center for High Resolution Neutron Scattering, a partnership between the National Institute of Standards and Technology and the National Science Foundation under agreement no. DMR-1508249. MD simulations were performed using the Oak Ridge Leadership Computing Facility (Summit allocation BIP109) at the Oak Ridge National Laboratory (supported by the Office of Science of the US Department of Energy under contract no. DE-AC05-00OR22725).

DECLARATION OF INTERESTS

The authors declare no competing interests.

REFERENCES

1. Zimmerberg, J., and K. Gawrisch. 2006. The physical chemistry of biological membranes. *Nat. Chem. Biol.* 2:564–567. https://doi.org/10.1038/nchembio1106-564. https://www.ncbi.nlm.nih.gov/pubmed/17051226.
2. Harayama, T., and H. Riezman. 2018. Understanding the diversity of membrane lipid composition. *Nat. Rev. Mol. Cell Biol.* 19:281–296. https://doi.org/10.1038/nrm.2017.138. https://www.ncbi.nlm.nih.gov/pubmed/29410529.
3. van Meer, G., D. R. Voelker, and G. W. Feigenson. 2008. Membrane lipids: where they are and how they behave. *Nat. Rev. Mol. Cell Biol.* 9:112–124. https://doi.org/10.1038/nrm2330. http://www.ncbi.nlm.nih.gov/entrez/query.fcgi?cmd=Retrieve&db=PubMed&dopt=Citation&list_uids=18216768.
4. Heberle, F. A., D. Marquardt, …, G. Pabst. 2016. Subnanometer structure of an asymmetric model membrane: interleaflet coupling influences domain properties. *Langmuir.* 32:5195–5200. https://doi.org/10.1021/acs.langmuir.5b04562. http://www.ncbi.nlm.nih.gov/pubmed/27128636.
5. Allolio, C., A. Haluts, and D. Harries. 2018. A local instantaneous surface method for extracting membrane elastic moduli from simulation: comparison with other strategies. *Chem. Phys.* 514:31–43. https://doi.org/10.1016/j.chemphys.2018.03.004.
6. Doktorova, M., N. Kučerka, …, F. A. Heberle. 2020. Molecular structure of sphingomyelin in fluid phase bilayers determined by the joint analysis of small-angle neutron and X-ray scattering data. *J. Phys. Chem. B.* 124:5186–5200. https://doi.org/10.1021/acs.jpcb.0c03389. https://www.ncbi.nlm.nih.gov/pubmed/32468822.
7. Yu, Y., A. Krämer, …, R. W. Pastor. 2021. CHARMM36 lipid force field with explicit treatment of long-range dispersion: parametrization and validation for phosphatidylethanolamine, phosphatidylglycerol, and ether lipids. *J. Chem. Theor. Comput.* 17:1581–1595. https://doi.org/10.1021/acs.jctc.0c01327. https://www.ncbi.nlm.nih.gov/pubmed/33620194.
8. Honerkamp-Smith, A. R., S. L. Veatch, and S. L. Keller. 2009. An introduction to critical points for biophysicists; observations of compositional heterogeneity in lipid membranes. *Biochim. Biophys. Acta.* 1788:53–63. https://doi.org/10.1016/j.bbamem.2008.09.010. https://www.ncbi.nlm.nih.gov/pubmed/18930706.
9. Sodt, A. J., M. L. Sandar, …, E. Lyman. 2014. The molecular structure of the liquid-ordered phase of lipid bilayers. *J. Am. Chem. Soc.* 136:725–732. https://doi.org/10.1021/ja4105667. https://www.ncbi.nlm.nih.gov/pubmed/24345334.
10. Lorent, J. H., K. R. Levental, …, I. Levental. 2020. Plasma membranes are asymmetric in lipid unsaturation, packing and protein shape. *Nat. Chem. Biol.* 16:644–652. https://doi.org/10.1038/s41589-020-0529-6. https://www.ncbi.nlm.nih.gov/pubmed/32367017.
11. Levental, I., K. R. Levental, and F. A. Heberle. 2020. Lipid rafts: controversies resolved, mysteries remain. *Trends Cell Biol.* 30:341–353. https://doi.org/10.1016/j.tcb.2020.01.009. https://www.ncbi.nlm.nih.gov/pubmed/32302547.
12. Lorent, J. H., B. Diaz-Rohrer, …, I. Levental. 2017. Structural determinants and functional consequences of protein affinity for membrane rafts. *Nat. Commun.* 8:1219. https://doi.org/10.1038/s41467-017-01328-3. https://www.ncbi.nlm.nih.gov/pubmed/29089556.
13. Doktorova, M., F. A. Heberle, …, R. A. Dick. 2017. Cholesterol promotes protein binding by affecting membrane electrostatics and solvation properties. *Biophys. J.* 113:2004–2015. https://doi.org/10.1016/j.bpj.2017.08.055. https://www.ncbi.nlm.nih.gov/pubmed/29117524.
14. Doktorova, M., F. A. Heberle, …, O. S. Andersen. 2019. Gramicidin increases lipid flip-flop in symmetric and asymmetric lipid vesicles. *Biophys. J.* 116:860–873. https://doi.org/10.1016/j.bpj.2019.01.016. https://www.ncbi.nlm.nih.gov/pubmed/30755300.
15. Ghysels, A., A. Krämer, …, R. W. Pastor. 2019. Permeability of membranes in the liquid ordered and liquid disordered phases. *Nat. Commun.* 10:5616. https://doi.org/10.1038/s41467-019-13432-7. https://www.ncbi.nlm.nih.gov/pubmed/31819053.
16. Kelley, E. G., P. D. Butler, …, M. Nagao. 2020. Scaling relationships for the elastic moduli and viscosity of mixed lipid membranes. *Proc. Natl. Acad. Sci. USA.* 117:23365–23373. https://doi.org/10.1073/pnas.2008789117. https://www.ncbi.nlm.nih.gov/pubmed/32883879.
17. Ballweg, S., E. Sezgin, …, R. Ernst. 2020. Regulation of lipid saturation without sensing membrane fluidity. *Nat. Commun.* 11:756. https://doi.org/10.1038/s41467-020-14528-1. https://www.ncbi.nlm.nih.gov/pubmed/32029718.
18. Dufourc, E. J., C. Mayer, …, G. Kothe. 1992. Dynamics of phosphate head groups in biomembranes. Comprehensive analysis using phosphorus-31 nuclear magnetic resonance lineshape and relaxation time measurements. *Biophys. J.* 61:42–57. https://doi.org/10.1016/S0006-3495(92)81814-3. https://www.ncbi.nlm.nih.gov/pubmed/1540698.
19. Weisz, K., G. Gröbner, …, G. Kothe. 1992. Deuteron nuclear magnetic resonance study of the dynamic organization of phospholipid/cholesterol bilayer membranes: molecular properties and viscoelastic behavior. *Biochemistry.* 31:1100–1112. https://doi.org/10.1021/bi00119a019.
20. Nowacka, A., P. C. Mohr, …, D. Topgaard. 2010. Polarization transfer solid-state NMR for studying surfactant phase behavior. *Langmuir.* 26:16848–16856. https://doi.org/10.1021/la102935t. https://www.ncbi.nlm.nih.gov/pubmed/20925371.
21. Leftin, A., C. Job, …, M. F. Brown. 2013. Solid-state ^{13}C NMR reveals annealing of raft-like membranes containing cholesterol by the intrinsically disordered protein α-synuclein. *J. Mol. Biol.* 425:2973–2987. https://doi.org/10.1016/j.jmb.2013.04.002. https://pubmed.ncbi.nlm.nih.gov/23583776.
22. Leftin, A., T. R. Molugu, …, M. F. Brown. 2014. Area per lipid and cholesterol interactions in membranes from separated local-field ^{13}C NMR spectroscopy. *Biophys. J.* 107:2274–2286. https://doi.org/10.1016/j.bpj.2014.07.044. https://pubmed.ncbi.nlm.nih.gov/25418296.
23. Brown, M. F. 2019. 7. Collective dynamics in lipid membranes. *In* Characterization of Biological Membranes: Structure and Dynamics. M. Nieh, F. Heberle, and J. Katsaras, eds De Gruyter, Berlin, pp. 231–268. https://doi.org/10.1515/9783110544657-007.
24. Douliez, J.-P., A. Léonard, and E. J. Dufourc. 1995. Restatement of order parameters in biomembranes: calculation of CC bond order parameters from CD quadrupolar splittings. *Biophys. J.* 68:1727–1739. https://doi.org/10.1016/S0006-3495(95)80350-4.
25. Douliez, J.-P., A. Ferrarini, and E.-J. Dufourc. 1998. On the relationship between CC and CD order parameters and its use for studying the conformation of lipid acyl chains in biomembranes. *J. Chem. Phys.* 109:2513–2518. https://doi.org/10.1063/1.476823.
26. Brown, M. F., and S. I. Chan. 2007. Bilayer membranes: deuterium carbon-13 NMR. *eMagRes*. https://doi.org/10.1002/9780470034590.emrstm0023.
27. Brown, M. F., R. L. Thurmond, …, K. Beyer. 2002. Elastic deformation of membrane bilayers probed by deuterium NMR relaxation. *J. Am. Chem. Soc.* 124:8471–8484. https://doi.org/10.1021/ja012660p. https://www.ncbi.nlm.nih.gov/pubmed/12105929.
28. Vermeer, L. S., B. L. de Groot, …, J. Czaplicki. 2007. Acyl chain order parameter profiles in phospholipid bilayers: computation from molecular dynamics simulations and comparison with ^{2}H NMR experiments. *Eur. Biophys. J.* 36:919–931. https://doi.org/10.1007/s00249-007-0192-9. https://www.ncbi.nlm.nih.gov/pubmed/17598103.
29. Klauda, J. B., R. M. Venable, …, R. W. Pastor. 2010. Update of the CHARMM all-atom additive force field for lipids: validation on six lipid types. *J. Phys. Chem. B.* 114:7830–7843. https://doi.org/10.1021/jp101759q. https://www.ncbi.nlm.nih.gov/pubmed/20496934.
30. Ferreira, T. M., F. Coreta-Gomes, …, D. Topgaard. 2013. Cholesterol and POPC segmental order parameters in lipid membranes: solid state ^{1}H–^{13}C NMR and MD simulation studies. *Phys. Chem. Chem. Phys.* 15:1976–1989. https://doi.org/10.1039/c2cp42738a. https://pubmed.ncbi.nlm.nih.gov/23258433.

31. Mallikarjunaiah, K. J., J. J. Kinnun, …, M. F. Brown. 2019. Flexible lipid nanomaterials studied by NMR spectroscopy. *Phys. Chem. Chem. Phys.* 21:18422–18457. https://doi.org/10.1039/c8cp06179c. https://www.ncbi.nlm.nih.gov/pubmed/31410425.

32. Pastor, R. W., R. M. Venable, and S. E. Feller. 2002. Lipid bilayers, NMR relaxation, and computer simulations. *Acc. Chem. Res.* 35:438–446. https://doi.org/10.1021/ar0100529. https://www.ncbi.nlm.nih.gov/pubmed/12069629.

33. Soubias, O., and K. Gawrisch. 2007. Docosahexaenoyl chains isomerize on the sub-nanosecond time scale. *J. Am. Chem. Soc.* 129:6678–6679. https://doi.org/10.1021/ja068856c. https://www.ncbi.nlm.nih.gov/pubmed/17477528.

34. Leftin, A., and M. F. Brown. 2011. An NMR database for simulations of membrane dynamics. *Biochim. Biophys. Acta.* 1808:818–839. https://doi.org/10.1016/j.bbamem.2010.11.027. https://www.ncbi.nlm.nih.gov/pubmed/21134351.

35. Brown, M. F. 1982. Theory of spin-lattice relaxation in lipid bilayers and biological membranes. ^{2}H and ^{14}N quadrupolar relaxation. *J. Chem. Phys.* 77:1576–1599. https://doi.org/10.1063/1.443940.

36. Usery, R. D., T. A. Enoki, …, G. W. Feigenson. 2018. Membrane bending moduli of coexisting liquid phases containing transmembrane peptide. *Biophys. J.* 114:2152–2164. https://doi.org/10.1016/j.bpj.2018.03.026. https://www.ncbi.nlm.nih.gov/pubmed/29742408.

37. Huber, T., K. Rajamoorthi, …, M. F. Brown. 2002. Structure of docosahexaenoic acid-containing phospholipid bilayers as studied by ^{2}H NMR and molecular dynamics simulations. *J. Am. Chem. Soc.* 124:298–309. https://doi.org/10.1021/ja011383j. https://pubmed.ncbi.nlm.nih.gov/11782182.

38. Venable, R. M., F. L. H. Brown, and R. W. Pastor. 2015. Mechanical properties of lipid bilayers from molecular dynamics simulation. *Chem. Phys. Lipids.* 192:60–74. https://doi.org/10.1016/j.chemphyslip.2015.07.014. https://www.ncbi.nlm.nih.gov/pubmed/26238099.

39. Smith, A. A., A. Vogel, …, D. Huster. 2022. A method to construct the dynamic landscape of a bio-membrane with experiment and simulation. *Nat. Commun.* 13:108. https://doi.org/10.1038/s41467-021-27417-y. https://www.ncbi.nlm.nih.gov/pubmed/35013165.

40. Trouard, T. P., A. A. Nevzorov, …, M. F. Brown. 1999. Influence of cholesterol on dynamics of dimyristoylphosphatidylcholine bilayers as studied by deuterium NMR relaxation. *J. Chem. Phys.* 110:8802–8818. https://doi.org/10.1063/1.478787.

41. Martinez, G. V., E. M. Dykstra, …, M. F. Brown. 2002. NMR elastometry of fluid membranes in the mesoscopic regime. *Phys. Rev. E.* 66:050902. https://doi.org/10.1103/PhysRevE.66.050902. https://www.ncbi.nlm.nih.gov/pubmed/12513460.

42. Martinez, G. V., E. M. Dykstra, …, M. F. Brown. 2004. Lanosterol and cholesterol-induced variations in bilayer elasticity probed by ^{2}H NMR relaxation. *Langmuir.* 20:1043–1046. https://doi.org/10.1021/la036063n. https://www.ncbi.nlm.nih.gov/pubmed/15803674.

43. Watson, M. C., E. G. Brandt, …, F. L. H. Brown. 2012. Determining biomembrane bending rigidities from simulations of modest size. *Phys. Rev. Lett.* 109:028102. https://doi.org/10.1103/PhysRevLett.109.028102. https://www.ncbi.nlm.nih.gov/pubmed/23030207.

44. Johner, N., D. Harries, and G. Khelashvili. 2014. Curvature and lipid packing modulate the elastic properties of lipid assemblies: comparing H_{II} and lamellar phases. *J. Phys. Chem. Lett.* 5:4201–4206. https://doi.org/10.1021/jz5022284. https://www.ncbi.nlm.nih.gov/pubmed/26278954.

45. Jo, S., T. Kim, …, W. Im. 2008. CHARMM-GUI: a web-based graphical user interface for CHARMM. *J. Comput. Chem.* 29:1859–1865. https://doi.org/10.1002/jcc.20945. https://www.ncbi.nlm.nih.gov/pubmed/18351591.

46. Brooks, B. R., C. L. Brooks, …, M. Karplus. 2009. CHARMM: the biomolecular simulation program. *J. Comput. Chem.* 30:1545–1614. https://doi.org/10.1002/jcc.21287. https://pubmed.ncbi.nlm.nih.gov/19444816.

47. Wu, E. L., X. Cheng, …, W. Im. 2014. CHARMM-GUI *membrane builder* toward realistic biological membrane simulations. *J. Comput. Chem.* 35:1997–2004. https://doi.org/10.1002/jcc.23702. https://www.ncbi.nlm.nih.gov/pubmed/25130509.

48. Lee, J., X. Cheng, …, W. Im. 2016. CHARMM-GUI input generator for NAMD, GROMACS, AMBER, OpenMM, and CHARMM/OpenMM simulations using the CHARMM36 additive force field. *J. Chem. Theor. Comput.* 12:405–413. https://doi.org/10.1021/acs.jctc.5b00935. https://www.ncbi.nlm.nih.gov/pubmed/26631602.

49. Lee, J., D. S. Patel, …, W. Im. 2019. CHARMM-GUI *membrane builder* for complex biological membrane simulations with glycolipids and lipoglycans. *J. Chem. Theor. Comput.* 15:775–786. https://doi.org/10.1021/acs.jctc.8b01066. https://www.ncbi.nlm.nih.gov/pubmed/30525595.

50. Phillips, J. C., D. J. Hardy, …, E. Tajkhorshid. 2020. Scalable molecular dynamics on CPU and GPU architectures with NAMD. *J. Chem. Phys.* 153:044130. https://doi.org/10.1063/5.0014475. https://www.ncbi.nlm.nih.gov/pubmed/32752662.

51. Lim, J. B., B. Rogaski, and J. B. Klauda. 2012. Update of the cholesterol force field parameters in CHARMM. *J. Phys. Chem. B.* 116:203–210. https://doi.org/10.1021/jp207925m. https://www.ncbi.nlm.nih.gov/pubmed/22136112.

52. Nevzorov, A. A., T. P. Trouard, and M. F. Brown. 1998. Lipid bilayer dynamics from simultaneous analysis of orientation and frequency dependence of deuterium spin-lattice and quadrupolar order relaxation. *Phys. Rev. E.* 58:2259–2281. https://doi.org/10.1103/PhysRevE.58.2259.

53. Eastman, P., J. Swails, …, V. S. Pande. 2017. OpenMM 7: rapid development of high performance algorithms for molecular dynamics. *PLoS Comput. Biol.* 13:e1005659. https://doi.org/10.1371/journal.pcbi.1005659. https://www.ncbi.nlm.nih.gov/pubmed/28746339.

54. Krämer, A., A. Ghysels, …, R. W. Pastor. 2020. Membrane permeability of small molecules from unbiased molecular dynamics simulations. *J. Chem. Phys.* 153:124107. https://doi.org/10.1063/5.0013429. https://www.ncbi.nlm.nih.gov/pubmed/33003739.

55. Humphrey, W., A. Dalke, and K. Schulten. 1996. VMD: visual molecular dynamics. *J. Mol. Graph.* 14:27–38. http://www.ncbi.nlm.nih.gov/pubmed/8744570.

56. Molugu, T. R., S. Lee, and M. F. Brown. 2017. Concepts and methods of solid-state NMR spectroscopy applied to biomembranes. *Chem. Rev.* 117:12087–12132. https://doi.org/10.1021/acs.chemrev.6b00619. https://www.ncbi.nlm.nih.gov/pubmed/28906107.

57. Rose, M. E. 1957. Elementary Theory of Angular Momentum. John Wiley & Sons, New York.

58. Kinnun, J. J., K. J. Mallikarjunaiah, …, M. F. Brown. 2015. Elastic deformation and area per lipid of membranes: atomistic view from solid-state deuterium NMR spectroscopy. *Biochim. Biophys. Acta.* 1848:246–259. https://doi.org/10.1016/j.bbamem.2014.06.004. https://pubmed.ncbi.nlm.nih.gov/24946141.

59. Giorgino, T. 2014. Computing 1-D atomic densities in macromolecular simulations: the density profile tool for VMD. *Comput. Phys. Commun.* 185:317–322. https://doi.org/10.1016/j.cpc.2013.08.022.

60. Doktorova, M., D. Harries, and G. Khelashvili. 2017. Determination of bending rigidity and tilt modulus of lipid membranes from real-space fluctuation analysis of molecular dynamics simulations. *Phys. Chem. Chem. Phys.* 19:16806–16818. https://doi.org/10.1039/c7cp01921a. https://www.ncbi.nlm.nih.gov/pubmed/28627570.

61. Johner, N., D. Harries, and G. Khelashvili. 2016. Implementation of a methodology for determining elastic properties of lipid assemblies from molecular dynamics simulations. *BMC Bioinf.* 17:161. https://doi.org/10.1186/s12859-016-1003-z. https://www.ncbi.nlm.nih.gov/pubmed/27071656.

62. Johner, N., D. Harries, and G. Khelashvili. 2016. Erratum to: implementation of a methodology for determining elastic properties of lipid assemblies from molecular dynamics simulations. *BMC Bioinf.* 17:236. https://doi.org/10.1186/s12859-016-1091-9. https://www.ncbi.nlm.nih.gov/pubmed/27301431.

63. Zilman, A. G., and R. Granek. 1996. Undulations and dynamic structure factor of membranes. *Phys. Rev. Lett.* 77:4788–4791. https://doi.org/10.1103/PhysRevLett.77.4788. https://www.ncbi.nlm.nih.gov/pubmed/10062631.

64. Watson, M. C., and F. L. H. Brown. 2010. Interpreting membrane scattering experiments at the mesoscale: the contribution of dissipation within the bilayer. *Biophys. J.* 98:L9–L11. https://doi.org/10.1016/j.bpj.2009.11.026. https://www.ncbi.nlm.nih.gov/pubmed/20303849.

65. Seifert, U., and S. A. Langer. 1993. Viscous modes of fluid bilayer membranes. *Europhys. Lett.* 23:71–76. https://doi.org/10.1209/0295-5075/23/1/012.

66. Nagao, M., E. G. Kelley, …, P. D. Butler. 2017. Probing elastic and viscous properties of phospholipid bilayers using neutron spin echo spectroscopy. *J. Phys. Chem. Lett.* 8:4679–4684. https://doi.org/10.1021/acs.jpclett.7b01830. https://www.ncbi.nlm.nih.gov/pubmed/28892394.

67. Högberg, C. J., and A. P. Lyubartsev. 2006. A molecular dynamics investigation of the influence of hydration and temperature on structural and dynamical properties of a dimyristoylphosphatidylcholine bilayer. *J. Phys. Chem. B.* 110:14326–14336. https://doi.org/10.1021/jp0614796. https://www.ncbi.nlm.nih.gov/pubmed/16854139.

68. Antila, H. S., T. M Ferreira, …, M. S. Miettinen. 2021. Using open data to rapidly benchmark biomolecular simulations: phospholipid conformational dynamics. *J. Chem. Inf. Model.* 61:938–949. https://doi.org/10.1021/acs.jcim.0c01299. https://www.ncbi.nlm.nih.gov/pubmed/33496579.

69. Tanford, C. 1978. The hydrophobic effect and the organization of living matter. *Science.* 200:1012–1018. https://doi.org/10.1126/science.653353. https://www.ncbi.nlm.nih.gov/pubmed/653353.

70. Klauda, J. B., N. V. Eldho, …, R. W. Pastor. 2008. Collective and noncollective models of NMR relaxation in lipid vesicles and multilayers. *J. Phys. Chem. B.* 112:5924–5929. https://doi.org/10.1021/jp075641w. https://www.ncbi.nlm.nih.gov/pubmed/18179193.

71. Doktorova, M., M. V. LeVine, …, H. Weinstein. 2019. A new computational method for membrane compressibility: bilayer mechanical thickness revisited. *Biophys. J.* 116:487–502. https://doi.org/10.1016/j.bpj.2018.12.016. https://pubmed.ncbi.nlm.nih.gov/30665693/.

72. Lindahl, E., and O. Edholm. 2000. Mesoscopic undulations and thickness fluctuations in lipid bilayers from molecular dynamics simulations. *Biophys. J.* 79:426–433. https://doi.org/10.1016/S0006-3495(00)76304-1. https://pubmed.ncbi.nlm.nih.gov/10866968.

73. Lindahl, E., and O. Edholm. 2001. Molecular dynamics simulation of NMR relaxation rates and slow dynamics in lipid bilayers. *J. Chem. Phys.* 115:4938–4950. https://doi.org/10.1063/1.1389469.

74. Trouard, T. P., T. M. Alam, and M. F. Brown. 1994. Angular dependence of deuterium spin-lattice relaxation rates of macroscopically oriented dilauroylphosphatidylcholine in the liquid-crystalline state. *J. Chem. Phys.* 101:5229–5261. https://doi.org/10.1063/1.467378.

75. Nevzorov, A. A., and M. F. Brown. 1997. Dynamics of lipid bilayers from comparative analysis of ^{2}H and ^{13}C nuclear magnetic resonance relaxation data as a function of frequency and temperature. *J. Chem. Phys.* 107:10288–10310. https://doi.org/10.1063/1.474169.

76. Marqusee, J. A. 1984. Dynamics of late stage phase separations in two dimensions. *J. Chem. Phys.* 81:976–981. https://doi.org/10.1063/1.447698.

77. Rommel, E., F. Noack, …, G. Kothe. 1988. Proton spin relaxation dispersion studies of phospholipid membranes. *J. Phys. Chem.* 92:2981–2987. https://doi.org/10.1021/j100321a053.

78. Althoff, G., O. Stauch, …, G. Kothe. 2002. Transverse nuclear spin relaxation studies of viscoelastic properties of membrane vesicles. II. Experimental results. *J. Phys. Chem. B.* 106:5517–5526. https://doi.org/10.1021/jp012829l.

79. Nevzorov, A. A., T. P. Trouard, and M. F. Brown. 1997. Correlation functions for lipid membrane dynamics obtained from NMR spectroscopy. *Phys. Rev. E.* 55:3276–3282. https://doi.org/10.1103/PhysRevE.55.3276.

80. Brown, M. F., A. A. Ribeiro, and G. D. Williams. 1983. New view of lipid bilayer dynamics from ^{2}H and ^{13}C NMR relaxation time measurements. *Proc. Natl. Acad. Sci. USA.* 80:4325–4329. https://doi.org/10.1073/pnas.80.14.4325. https://www.ncbi.nlm.nih.gov/pubmed/6576340.

81. Williams, G. D., J. M. Beach, …, M. F. Brown. 1985. Dependence of deuterium spin-lattice relaxation rates of multilamellar phospholipid dispersions on orientational order. *J. Am. Chem. Soc.* 107:6868–6873. https://doi.org/10.1021/ja00310a021.

82. Brown, M. F., R. L. Thurmond, …, K. Beyer. 2001. Composite membrane deformation on the mesoscopic length scale. *Phys. Rev. E.* 64:010901. https://doi.org/10.1103/PhysRevE.64.010901.

83. Chakraborty, S., M. Doktorova, …, R. Ashkar. 2020. How cholesterol stiffens unsaturated lipid membranes. *Proc. Natl. Acad. Sci. USA.* 117:21896–21905. https://doi.org/10.1073/pnas.2004807117. https://www.ncbi.nlm.nih.gov/pubmed/32843347.

84. Zgorski, A., R. W. Pastor, and E. Lyman. 2019. Surface shear viscosity and interleaflet friction from nonequilibrium simulations of lipid bilayers. *J. Chem. Theor. Comput.* 15:6471–6481. https://doi.org/10.1021/acs.jctc.9b00683. https://www.ncbi.nlm.nih.gov/pubmed/31476126.

85. Brown, M. F. 1984. Theory of spin-lattice relaxation in lipid bilayers and biological membranes. Dipolar relaxation. *J. Chem. Phys.* 80:2808–2831. https://doi.org/10.1063/1.447030.

86. Teague, W. E., Jr., O. Soubias, …, K. Gawrisch. 2013. Elastic properties of polyunsaturated phosphatidylethanolamines influence rhodopsin function. *Faraday Discuss.* 161:383–395. https://doi.org/10.1039/c2fd20095c. https://www.ncbi.nlm.nih.gov/pubmed/23805751.

87. Brown, M. F. 2017. Soft matter in lipid-protein interactions. *Annu. Rev. Biophys.* 46:379–410. https://doi.org/10.1146/annurev-biophys-070816-033843. https://www.ncbi.nlm.nih.gov/pubmed/28532212.

88. Ashkar, R., M. Doktorova, …, M. F. Brown. 2021. Reply to Nagle et al.: the universal stiffening effects of cholesterol on lipid membranes. *Proc. Natl. Acad. Sci. USA.* 118. e2102845118. https://doi.org/10.1073/pnas.2102845118. https://www.ncbi.nlm.nih.gov/pubmed/33952694.

89. Eldho, N. V., S. E. Feller, …, K. Gawrisch. 2003. Polyunsaturated docosahexaenoic vs docosapentaenoic acid–differences in lipid matrix properties from the loss of one double bond. *J. Am. Chem. Soc.* 125:6409–6421. https://doi.org/10.1021/ja029029o. http://www.ncbi.nlm.nih.gov/pubmed/12785780.

90. Pastor, R. W., R. M. Venable, …, A. Szabo. 1988. A simulation based model of NMR T_1 relaxation in lipid bilayer vesicles. *J. Chem. Phys.* 89:1128–1140. https://doi.org/10.1063/1.455219.

91. Lipari, G., and A. Szabo. 1982. Model-free approach to the interpretation of nuclear magnetic resonance relaxation in macromolecules. 1. Theory and range of validity. *J. Am. Chem. Soc.* 104:4546–4559. https://doi.org/10.1021/ja00381a009.

92. Prompers, J. J., and R. Brüschweiler. 2001. Reorientational eigenmode dynamics: a combined MD/NMR relaxation analysis method for flexible parts in globular proteins. *J. Am. Chem. Soc.* 123:7305–7313. https://doi.org/10.1021/ja0107226. https://www.ncbi.nlm.nih.gov/pubmed/11472158.

93. Vogel, A., K. T. Tan, …, D. Huster. 2007. Flexibility of ras lipid modifications studied by ^{2}H solid-state NMR and molecular dynamics simulations. *Biophys. J.* 93:2697–2712. https://doi.org/10.1529/biophysj.107.104562. https://www.ncbi.nlm.nih.gov/pubmed/17557790.

94. Vogel, A., G. Reuther, …, D. Huster. 2010. Backbone conformational flexibility of the lipid modified membrane anchor of the human N-Ras protein investigated by solid-state NMR and molecular dynamics simulation. *Biochim. Biophys. Acta.* 1798:275–285. https://doi.org/10.1016/j.bbamem.2009.09.023. https://www.ncbi.nlm.nih.gov/pubmed/19819220.

95. Gu, Y., D. W. Li, and R. Brüschweiler. 2014. NMR order parameter determination from long molecular dynamics trajectories for objective comparison with experiment. *J. Chem. Theor. Comput.* 10:2599–2607. https://doi.org/10.1021/ct500181v. https://www.ncbi.nlm.nih.gov/pubmed/26580780.

96. Petrache, H. I., S. W. Dodd, and M. F. Brown. 2000. Area per lipid and acyl length distributions in fluid phosphatidylcholines determined by ^{2}H NMR spectroscopy. *Biophys. J.* 79:3172–3192. https://doi.org/10.1016/S0006-3495(00)76551-9. https://www.ncbi.nlm.nih.gov/pubmed/11106622.

97. Helfrich, W. 1973. Elastic properties of lipid bilayers: theory and possible experiments. *Z. Naturforsch.* 28c:693–703. https://doi.org/10.1515/znc-1973-11-1209. https://pubmed.ncbi.nlm.nih.gov/4273690.

Biophysical Journal, Volume *122*

Supplemental information

Molecular simulations and NMR reveal how lipid fluctuations affect membrane mechanics

Milka Doktorova, George Khelashvili, Rana Ashkar, and Michael F. Brown

Supporting Material

Molecular Simulations and NMR Reveal How Lipid Fluctuations Affect Membrane Mechanics

Milka Doktorova, George Khelashvili, Rana Ashkar, Michael F. Brown

The document includes 2 tables, 16 figures and extended methods.

The figures are as follows:

Fig. S1 schematic of Euler and polar angles describing the forward and inverse transformations to and from the CH bond position

Fig. S2–S4 correlation functions $G_{p,2}^{(n)}(t)$ for all carbons in the simulated bilayers with their corresponding best power-law fits

Fig. S5 actual and resampled correlation functions $G_{0,2}^{(n)}(t)$

Fig. S6 optimal Δt_{fit} values (in ps) obtained from resampling of $G_{0,s}^{(n)}(t)$

Fig. S7–S9 spectral density functions $J_{p,2}^{(n)}(\omega)$ for all carbons in the simulated bilayers with their corresponding best power-law fits

Fig. S10 *b* exponents of the best power-law fits to the correlation functions $G_{p,s}^{(n)}(t)$ and spectral density functions $J_{p,s}^{(n)}(\omega)$ for all carbons in the simulated bilayers

Fig. S11–S13 the spectral density functions $J_{0,2}^{(n)}(\omega)$ of local director vectors and their corresponding best power-law fits

Fig. S14 bilayer structural properties (order parameters, lipid packing and thickness) as a function of cholesterol concentration

Fig. S15 linear and log-log plots of R_{1Z} vs $|S_{CD}|^2$ for all carbons in the simulated bilayers

Fig. S16 effect of bilayer viscosity η on the bending rigidity κ_C calculated from the square-law relationship

Table S1. Full bilayer thicknesses calculated from the bilayer number density profile as described in Methods.

Bilayer composition	Thickness / Å
DMPC	51.2
DMPC/Chol 80/20	55.2
DMPC/Chol 67/33	56.4
DMPC/Chol 50/50	55.6

Table S2. Reference values for estimates of the bending modulus for DMPC bilayers obtained from experiments and simulations. C36 denotes CHARMM36 force field.

Bending modulus / $k_B T$	Method	Reference
29.2 ± 1.2	simulations, C36, lipid director fluctuations	(1)
25.1 ± 1.0	X-ray diffuse scattering	(2)
31.1 ± 1.9	Flicker analysis of vesicle fluctuations	(3)
24.8 ± 1.1	simulations, C36, square-law	this paper
33.2 ± 1.0	simulations, C36, splay fluctuations	this paper
18.5 ± 1.0	NMR	this paper
28.1 ± 4.4	NSE	this paper

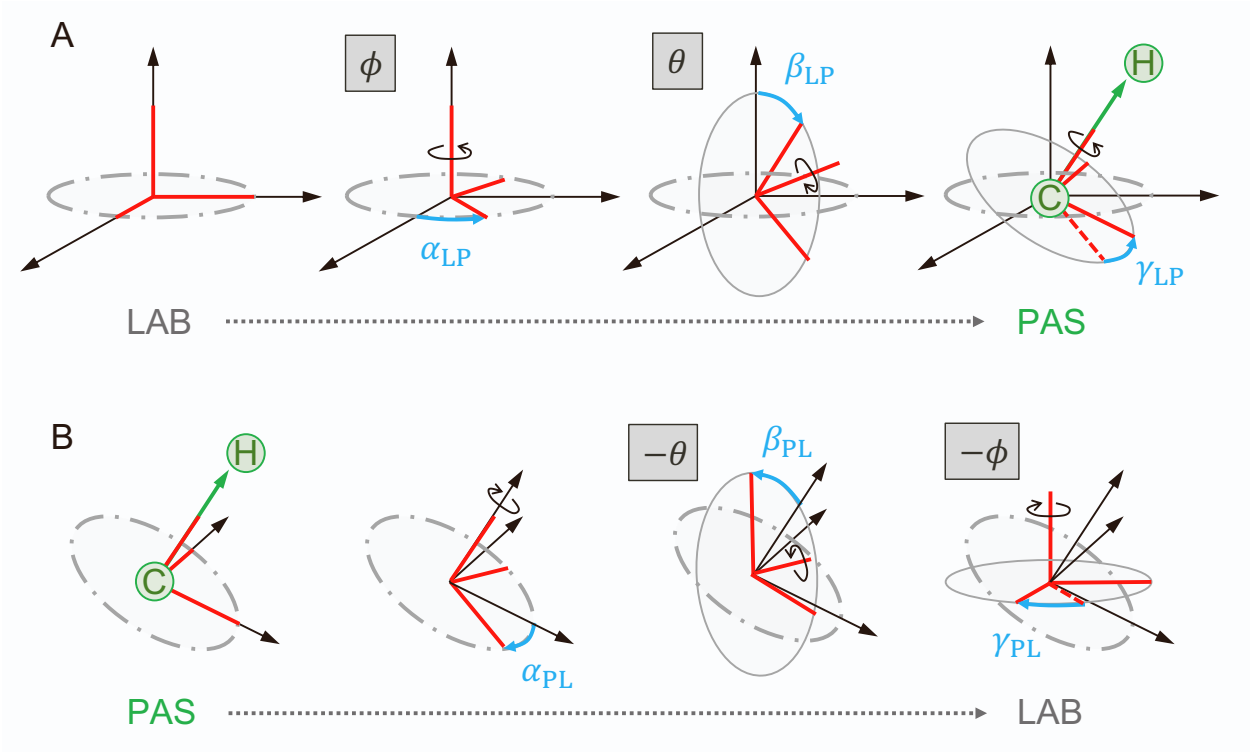

Figure S1. Schematic representation of the angles describing (A) the forward transformation from the laboratory frame (LAB) to the principal axis system (PAS) which is defined as the CH bond position (green), and (B) the inverse transformation from PAS to LAB. The Euler angles for the forward transformation are $\Omega_{LP} = (\alpha_{LP}, \beta_{LP}, \gamma_{LP})$ while the Euler angles for the inverse transformation are $\Omega_{PL} = (\alpha_{PL}, \beta_{PL}, \gamma_{PL}) = (-\gamma_{LP}, -\beta_{LP}, -\alpha_{LP})$. The corresponding polar angles (θ, ϕ) are indicated in grey-shaded boxes next to their Euler angle equivalents.

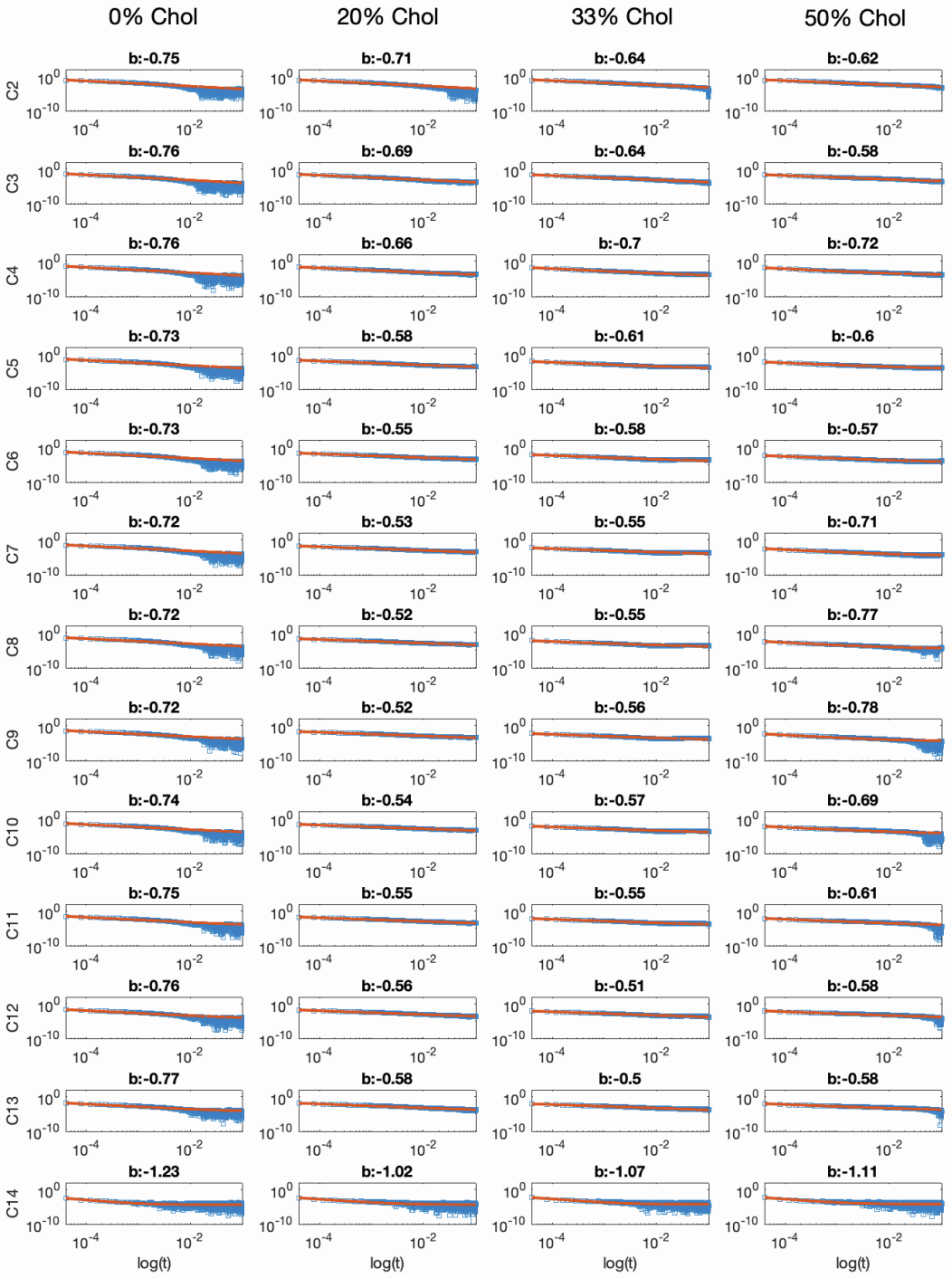

Figure S2. Log-log plot of the correlation function $G_{0,2}^{(n)}(t)$, $t \geq 1$ for each carbon atom C*n* (indicated on the left) on the *sn*-2 chain of DMPC in the bilayers with 0%, 20%, 33%, and 50% cholesterol (Chol) (blue data points), and corresponding best fit to a power-law function of the form $ax^b + c$ (red solid line). Shown above each plot is the b-exponent of the best fit. Only the first 100 ns of the correlation function are shown to better illustrate the fit. All plots have the same x- and y-axes.

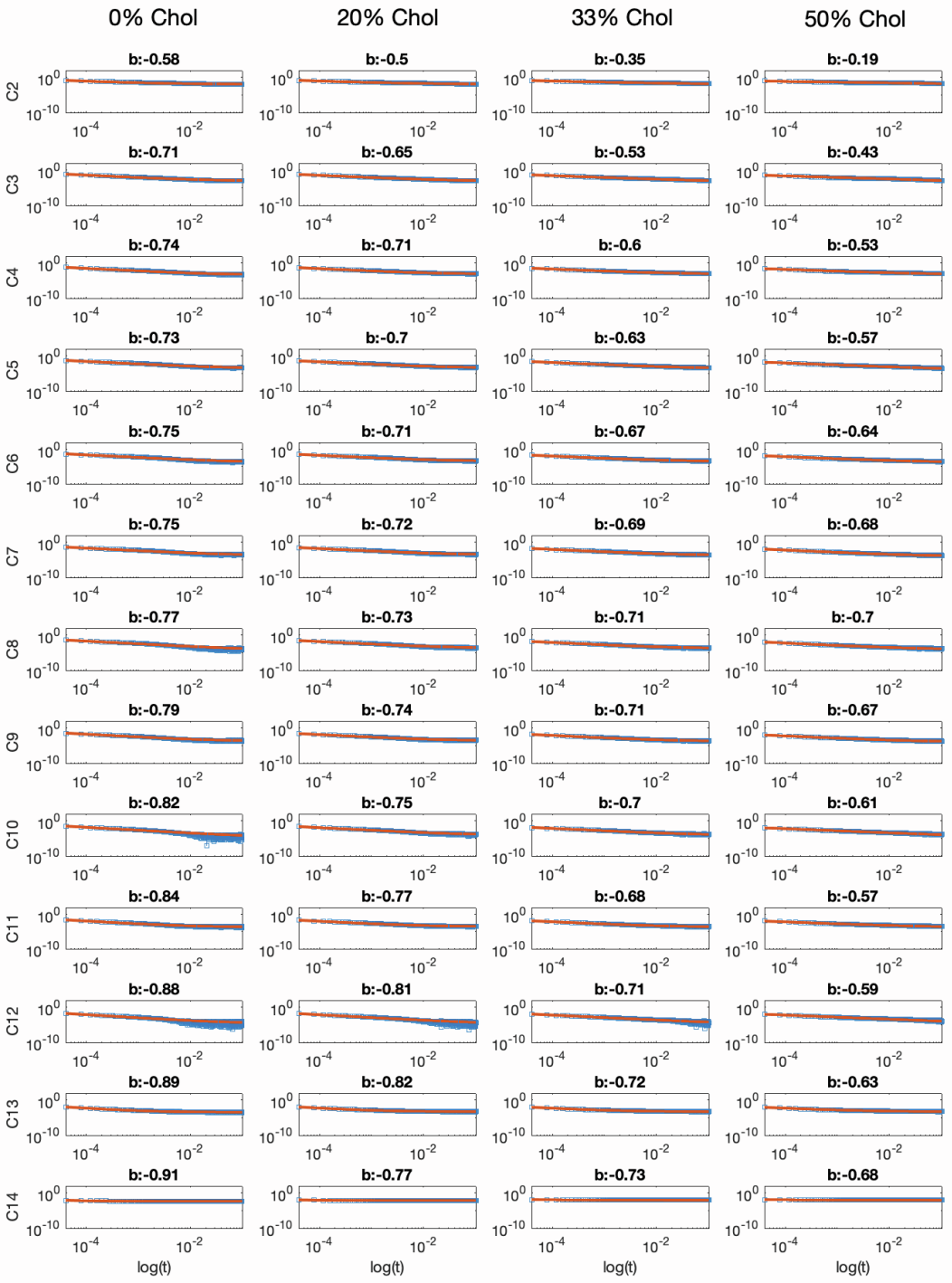

Figure S3. Log-log plot of the correlation function $G_{1,2}^{(n)}(t), t \geq 1$ for each carbon atom C*n* (indicated on the left) on the *sn*-2 chain of DMPC in the bilayers with 0%, 20%, 33%, and 50% Chol (blue data points), and corresponding best fit to a power-law function of the form $ax^b + c$ (red solid line). Shown above each plot is the b-exponent of the best fit. Only the first 100 ns of the correlation function are shown to better illustrate the fit. All plots have the same x- and y-axes.

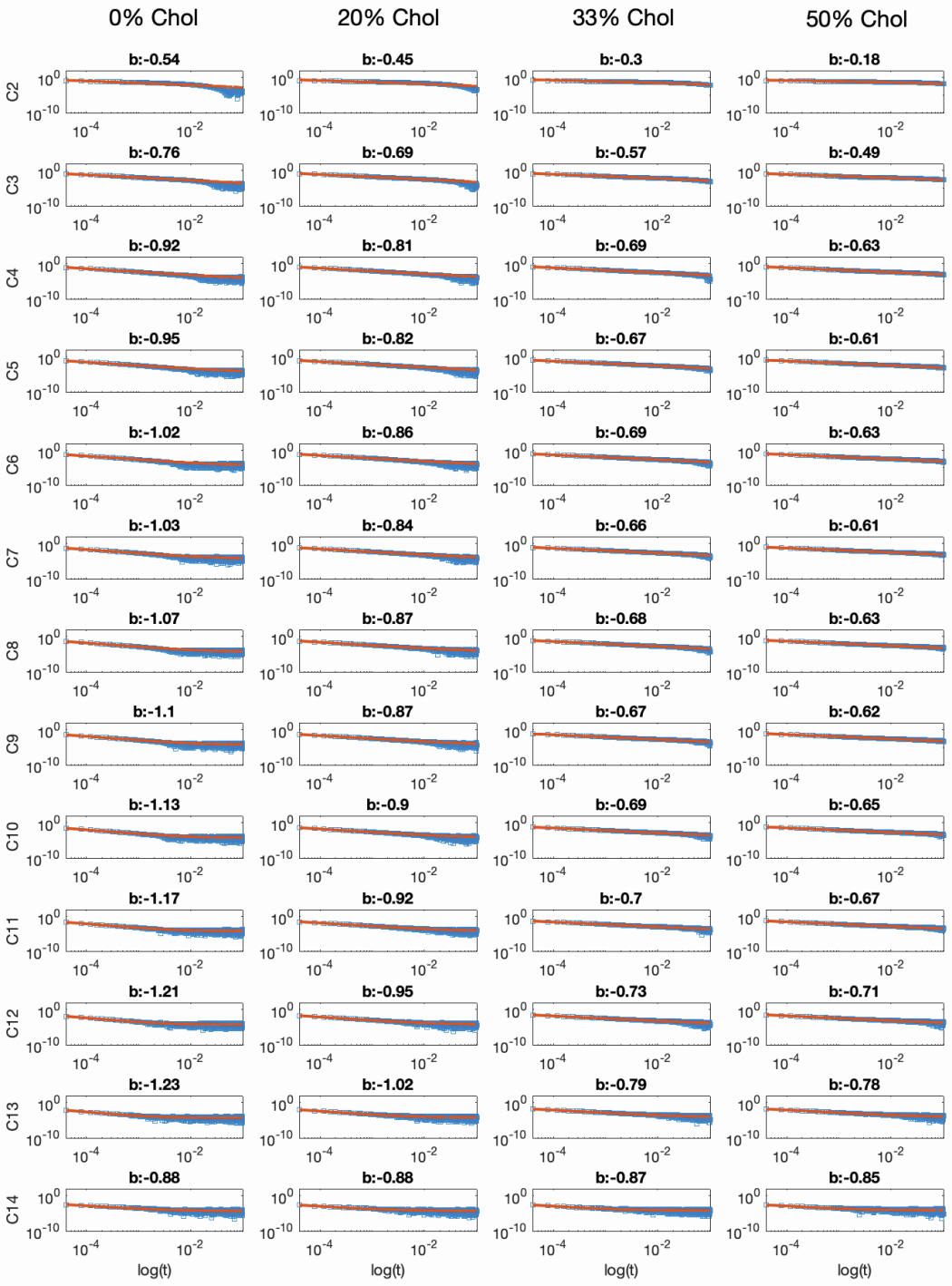

Figure S4. Log-log plot of the correlation function $G_{2,2}^{(n)}(t)$, $t \geq 1$ for each carbon atom C*n* (indicated on the left) on the *sn*-2 chain of DMPC in the bilayers with 0%, 20%, 33%, and 50% Chol (blue data points), and corresponding best fit to a power-law function of the form $ax^b + c$ (red solid line). Shown above each plot is the b-exponent of the best fit. Only the first 100 ns of the correlation function are shown to better illustrate the fit. All plots have the same x- and y-axes.

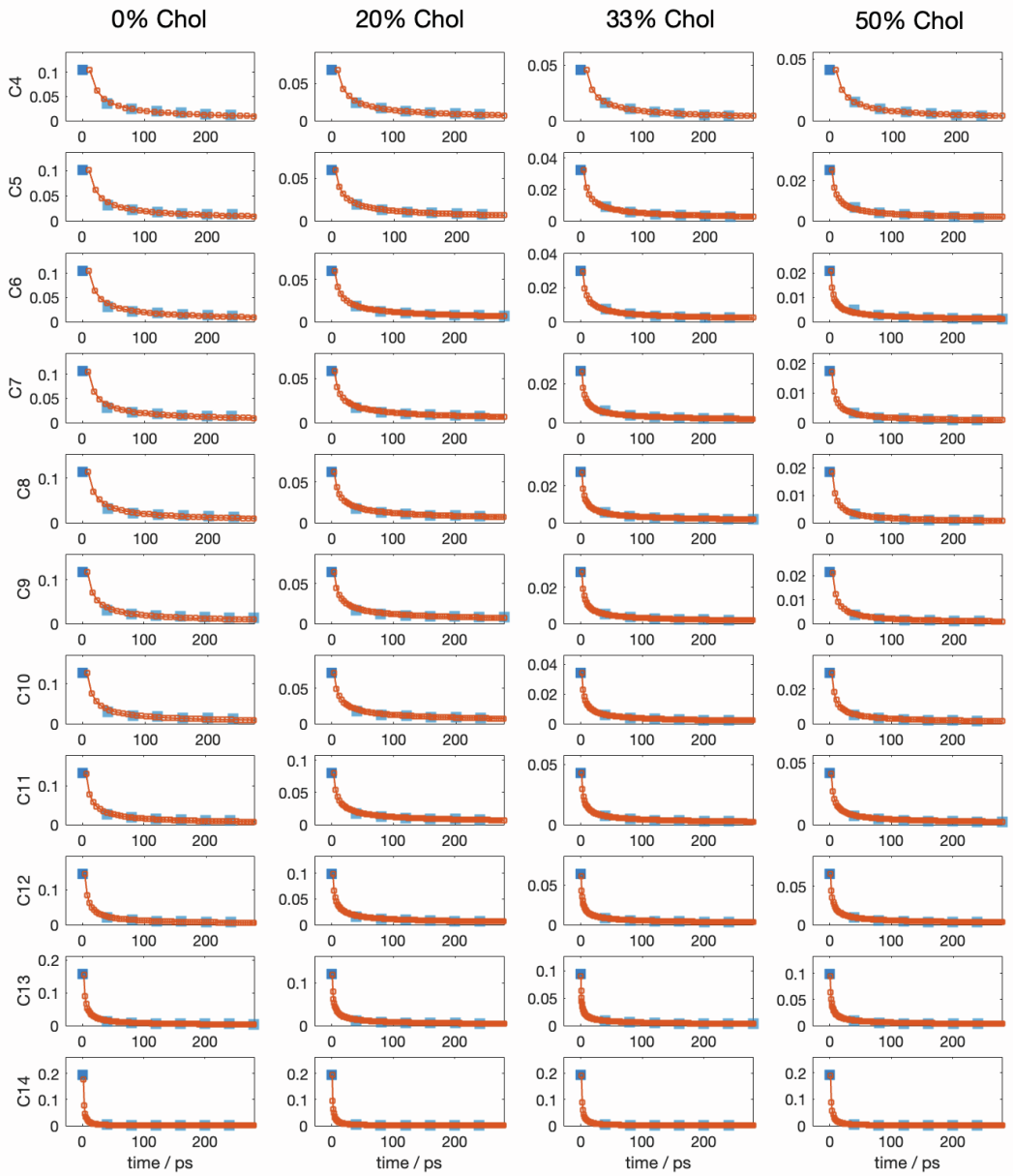

Figure S5. First 200 ps of the correlation function $G_{0,2}^{(n)}(t)$, $t \geq 0$ for carbons C4–C14 (indicated on the left) on the *sn*-2 chain of DMPC in the bilayers with 0%, 20%, 33%, and 50% Chol sampled at the original $\Delta t = 40$ ps (blue shaded squares), and the resampled correlation function from the best fits from Fig. S2 sampled at the optimal $\Delta t_{\mathrm{fit}} < \Delta t$ (red). The initial values $G_{0,2}^{(n)}(0)$ are highlighted in solid blue color.

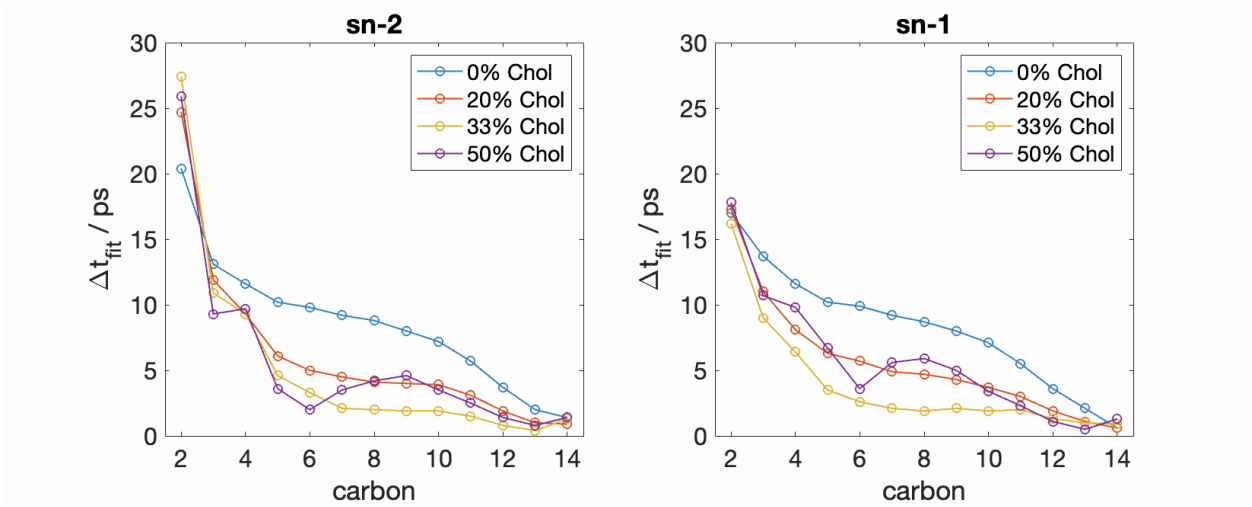

Figure S6. Optimal Δt_{fit} values (in ps) obtained from resampling of $G_{0,s}^{(n)}(t)$ using the best fit (see Figure S5) for each carbon on the *sn*-1 and *sn*-2 chains of DMPC in the simulated bilayers. The simulation output frequency (and thus, original timestep Δt) in the trajectories correspond to Δt = 40 ps. The decrease of Δt_{fit} further down the chain towards the terminal methyl (C14) is consistent with faster rapid motions closer to the bilayer midplane.

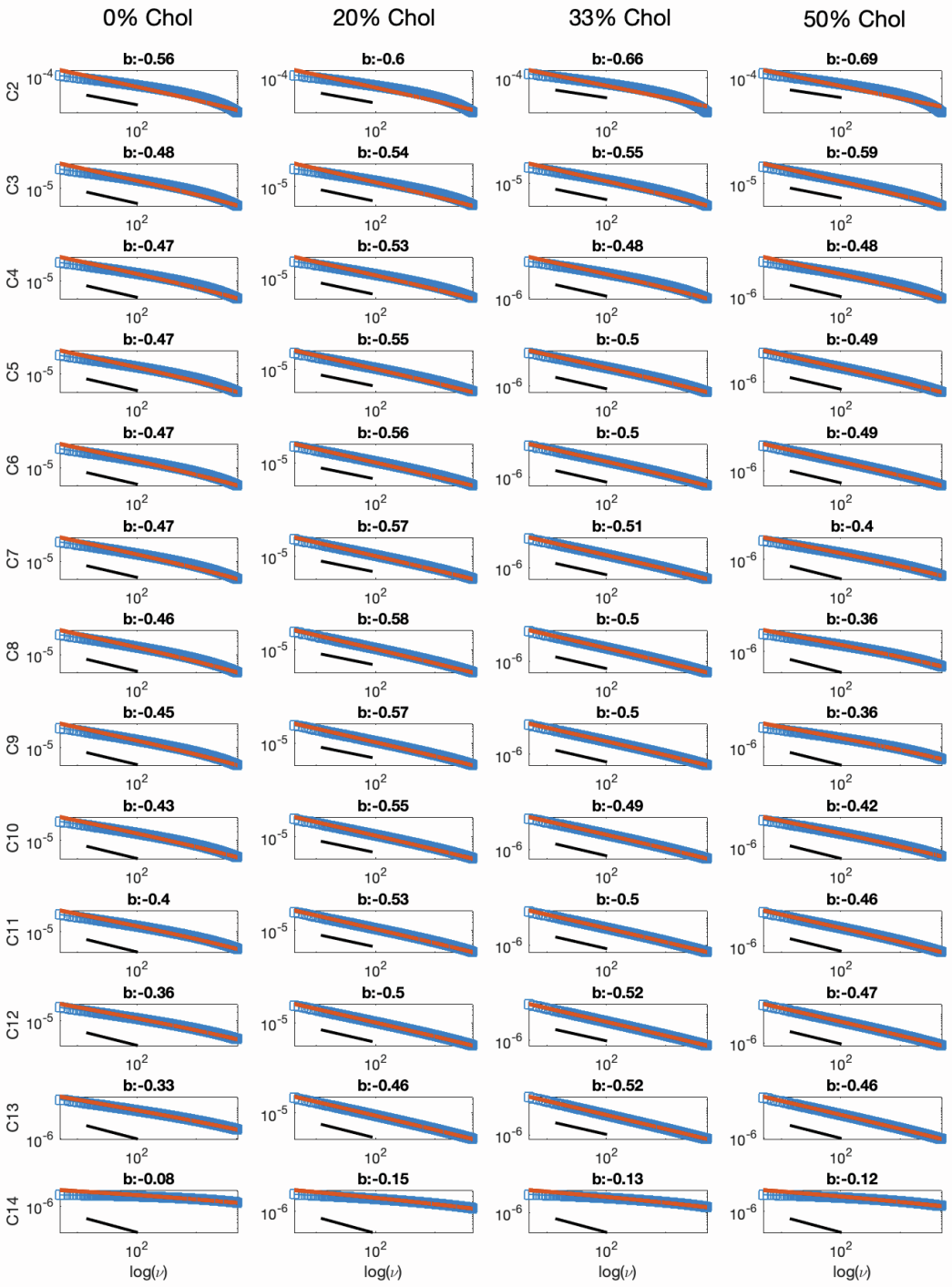

Figure S7. Log-log plots of the spectral density $J_{0,2}^{(n)}(\omega)$ (blue) for each carbon C*n* (indicated on the left) on the *sn*-2 chain of DMPC in the simulated bilayers, and its corresponding best fit to a power-law function of the form $ax^b + c$ (red solid line). Indicated above each plot is the b-exponent of the best fit. For visual comparison, a black line following a power-law with an exponent of −0.5 is shown below the data and the fits.

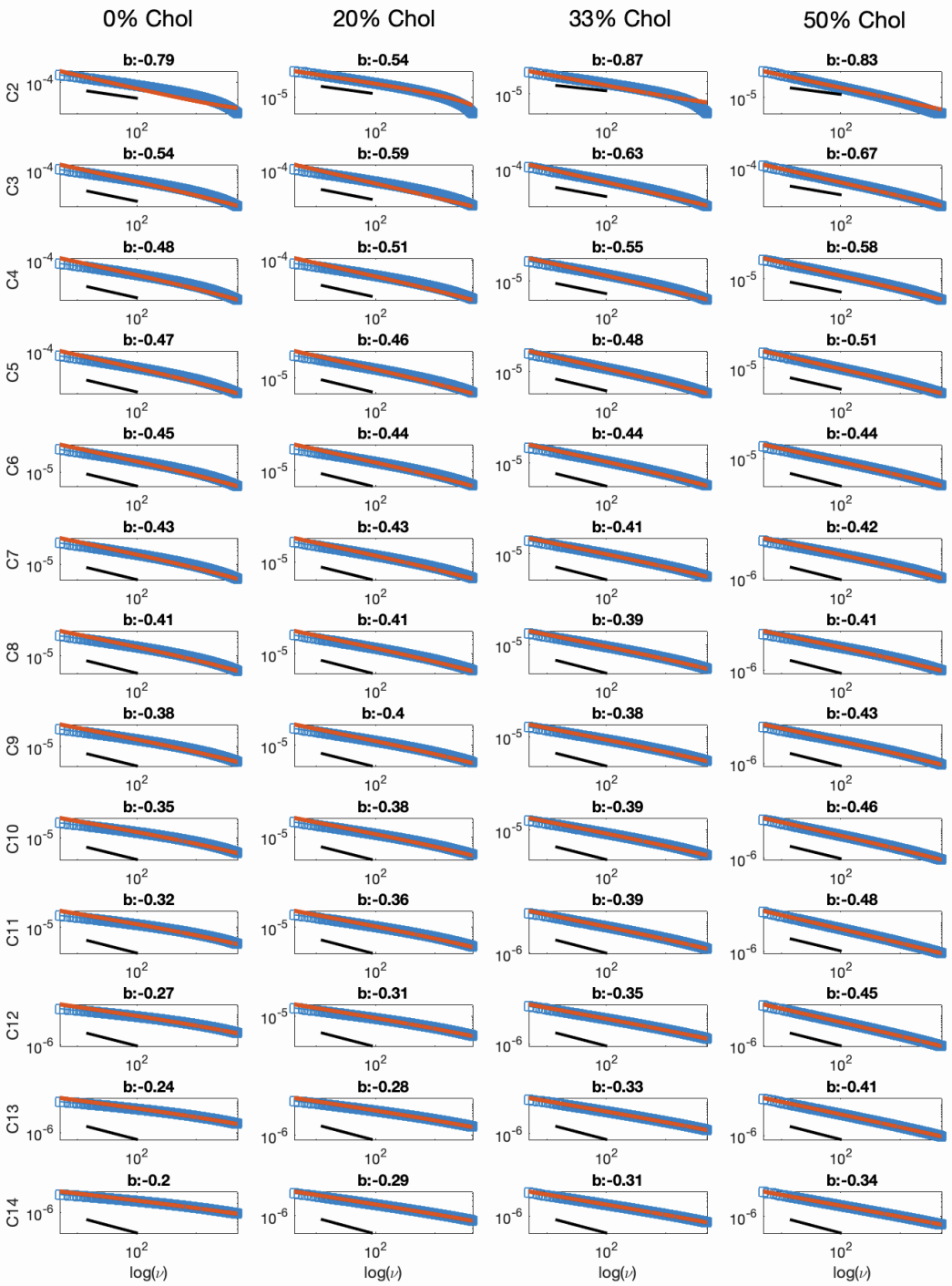

Figure S8. Log-log plots of the spectral density $J_{1,2}^{(n)}(\omega)$ (blue) for each carbon C*n* (indicated on the left) on the *sn*-2 chain of DMPC in the simulated bilayers, and its corresponding best fit to a power-law function of the form $ax^b + c$ (red solid line). Indicated above each plot is the b-exponent of the best fit. For visual comparison, a black line following a power-law with an exponent of −0.5 is shown below the data and fits.

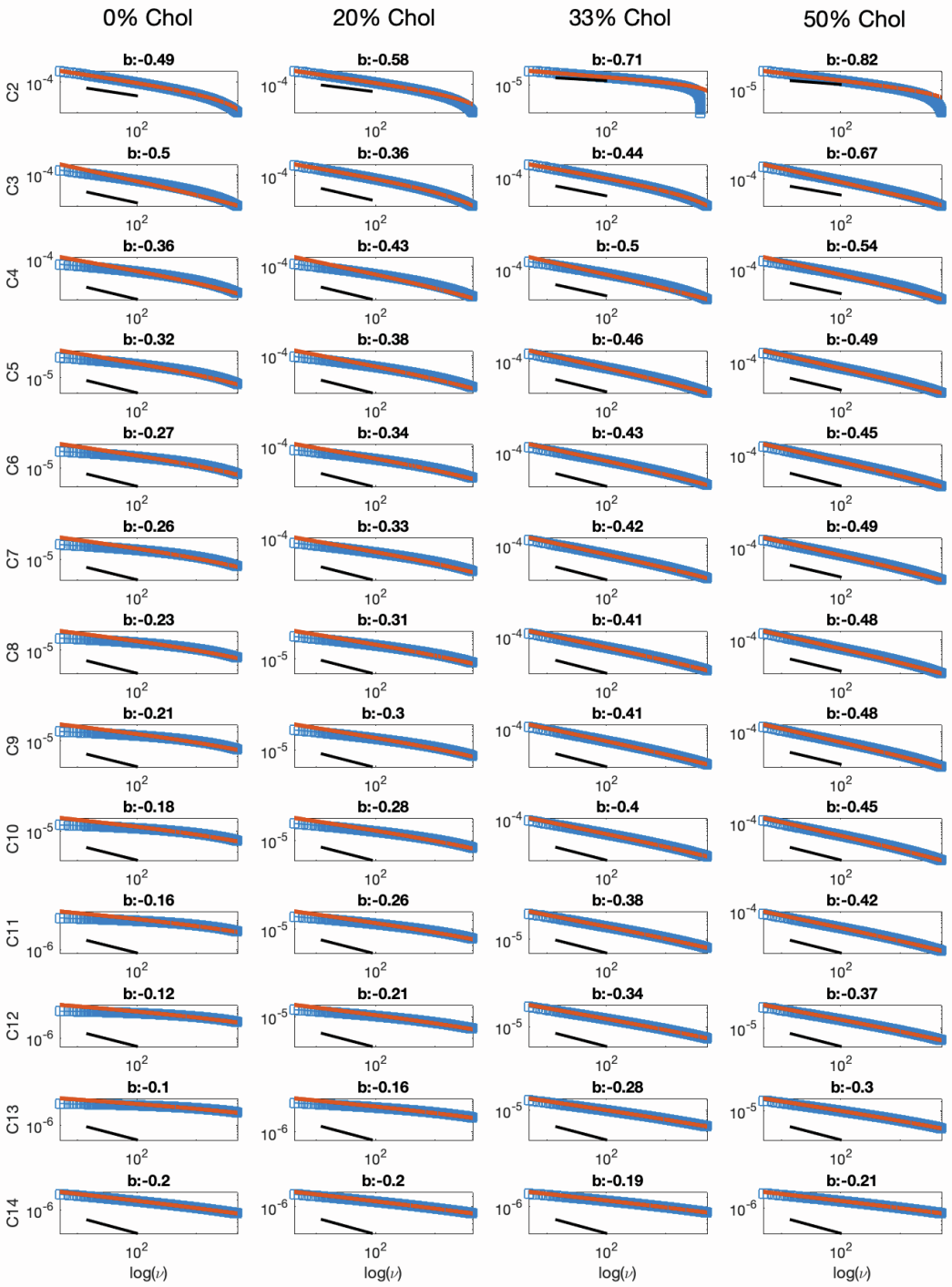

Figure S9. Log-log plots of the spectral density $J_{2,2}^{(n)}(\omega)$ (blue) for each carbon C*n* (indicated on the left) on the *sn*-2 chain of DMPC in the simulated bilayers, and its corresponding best fit to a power-law function of the form $ax^b + c$ (red solid line). Indicated above each plot is the b-exponent of the best fit. For visual comparison, a black line following a power-law with an exponent of −0.5 is shown below the data and fits.

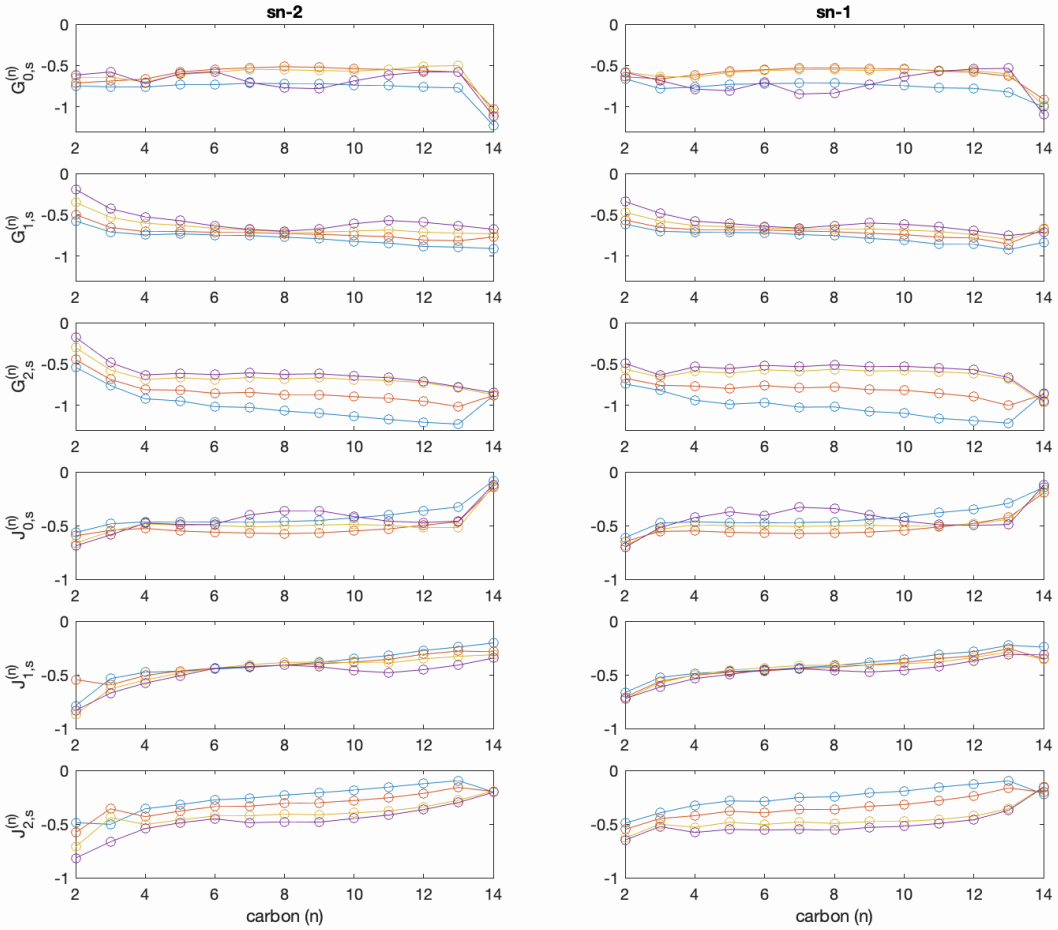

Figure S10. Plots of *b*-exponents of the best fits to the correlation function $G_{p,s}^{(n)}(t)$ (top 3 rows) and spectral density $J_{p,s}^{(n)}(\omega)$ (bottom 3 rows) for each carbon on the *sn*-2 (left) and *sn*-1 (right) chains of DMPC in the bilayers with 0 (blue), 20 (red), 33 (yellow), and 50% (purple) cholesterol. Note that the y-axis for the correlation functions ranges from −1.3 to 0, while for the spectral densities it is between −1 and 0.

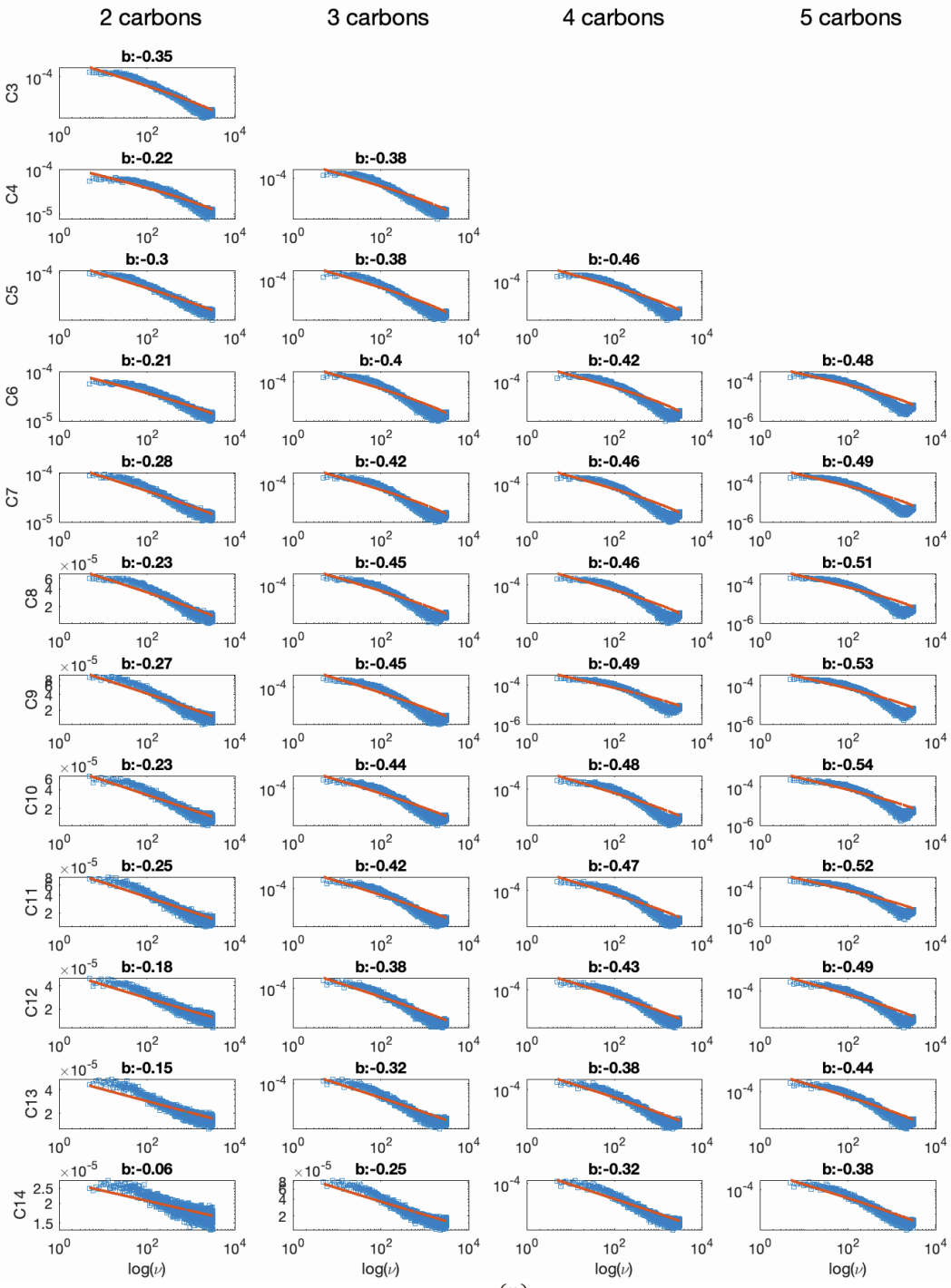

Figure S11. Log-log plots of the spectral density $J_{0,2}^{(n)}(\omega)$ of local director (LD) vectors of lengths 2–5 carbons. Each row corresponds to LD vectors originating from the same carbon C*n* (indicated on the left). Raw data are shown in blue and best fit to a power-law function of the form $ax^b + c$ is shown in red. The corresponding power-law coefficients of the best fits are indicated above the plots.

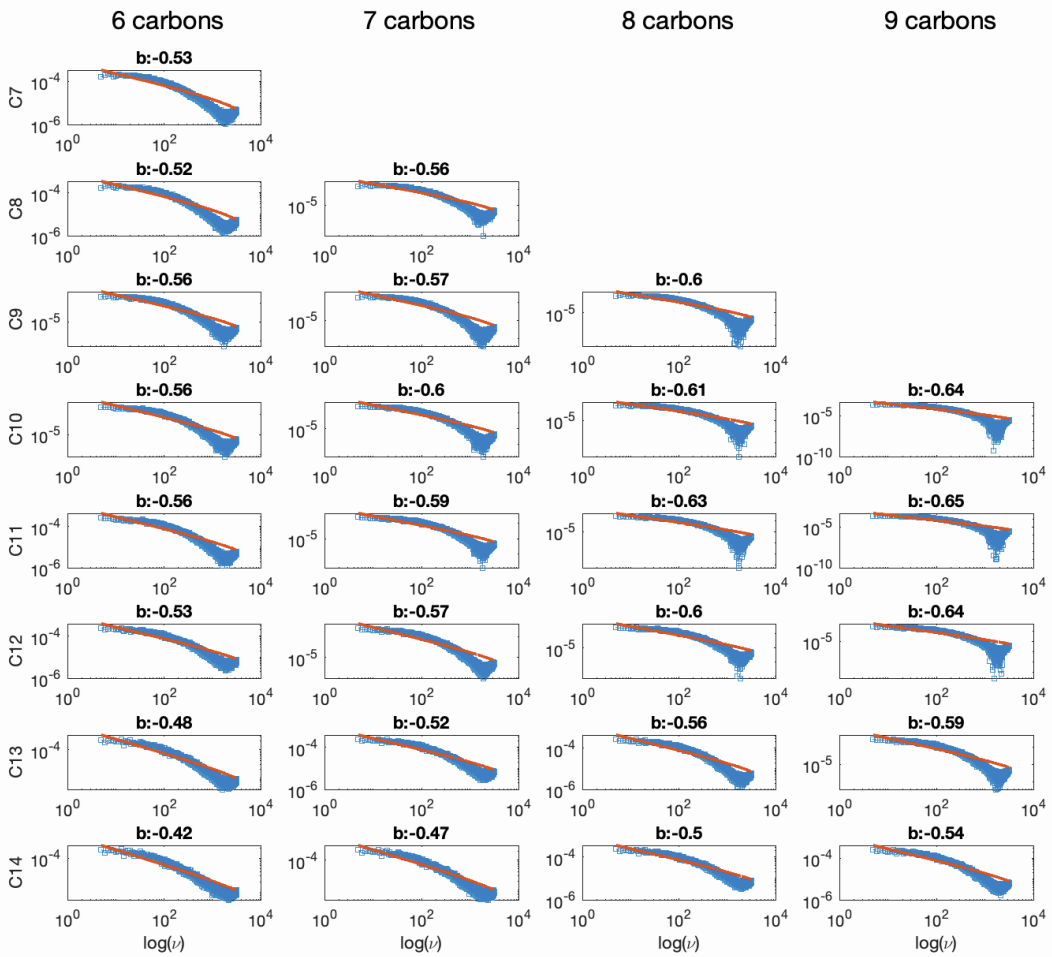

Figure S12. Log-log plots of the spectral density $J_{0,2}^{(n)}(\omega)$ of local director (LD) vectors of lengths 6–9 carbons. Each row corresponds to LD vectors originating from the same carbon C*n* (indicated on the left). Raw data are shown in blue and best fit to a power-law function of the form $ax^b + c$ is shown in red. The corresponding power-law coefficients of the best fits are indicated above the plots.

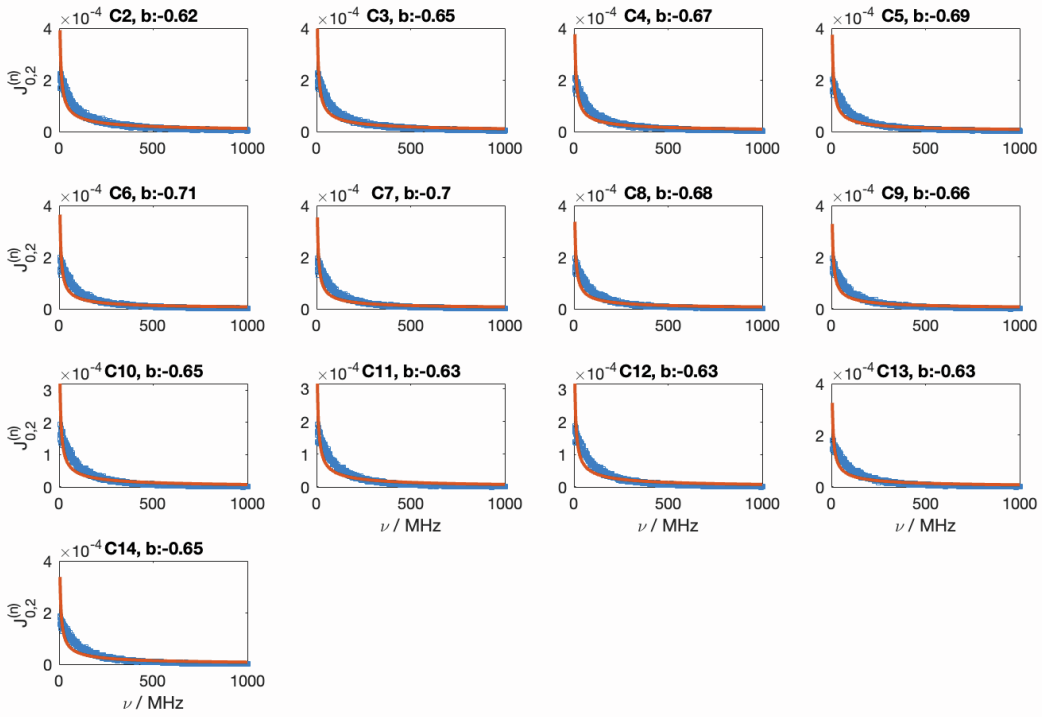

Figure S13. Linear plots of the spectral density $J^{(n)}_{0,2}(\omega)$ of local director (LD) vectors connecting each carbon C*n* (indicated above each plot) to the phosphate atom of the lipid. Raw data are shown in blue and best fit to a power-law function of the form $ax^b + c$ is shown in red. The corresponding power-law coefficients of the best fits are indicated above the plots.

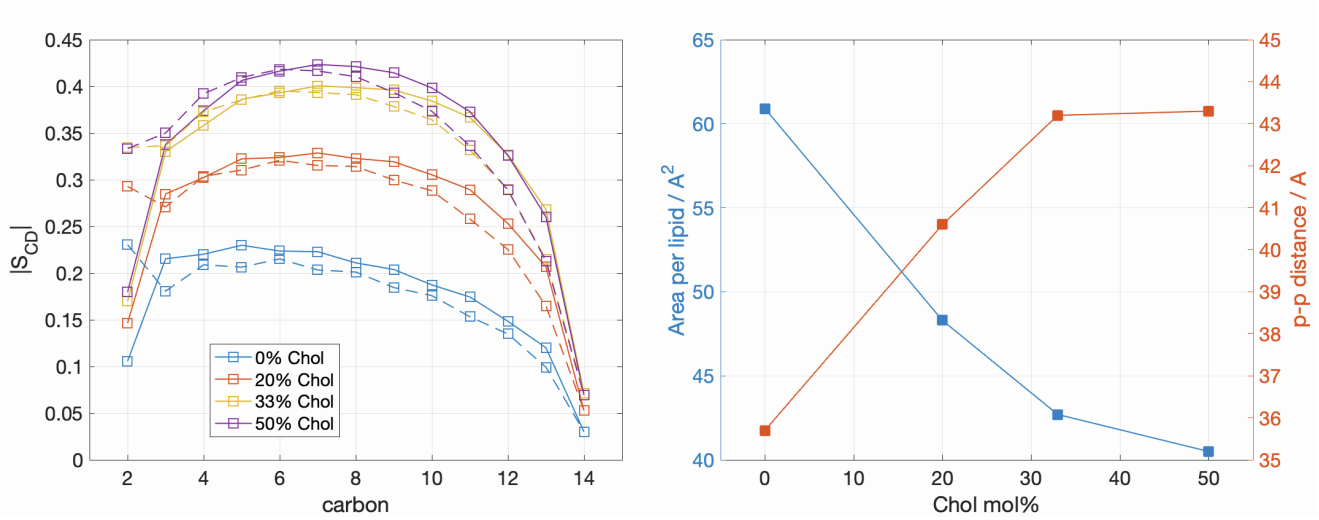

Figure S14. (Left) Order parameter profiles for the two chains of DMPC, *sn*-1 (dashed) and *sn*-2 (solid), in the simulated bilayers. (Right) Average area per lipid (blue, left axis) and phosphate-to-phosphate distance (red, right axis) as a function of cholesterol concentration.

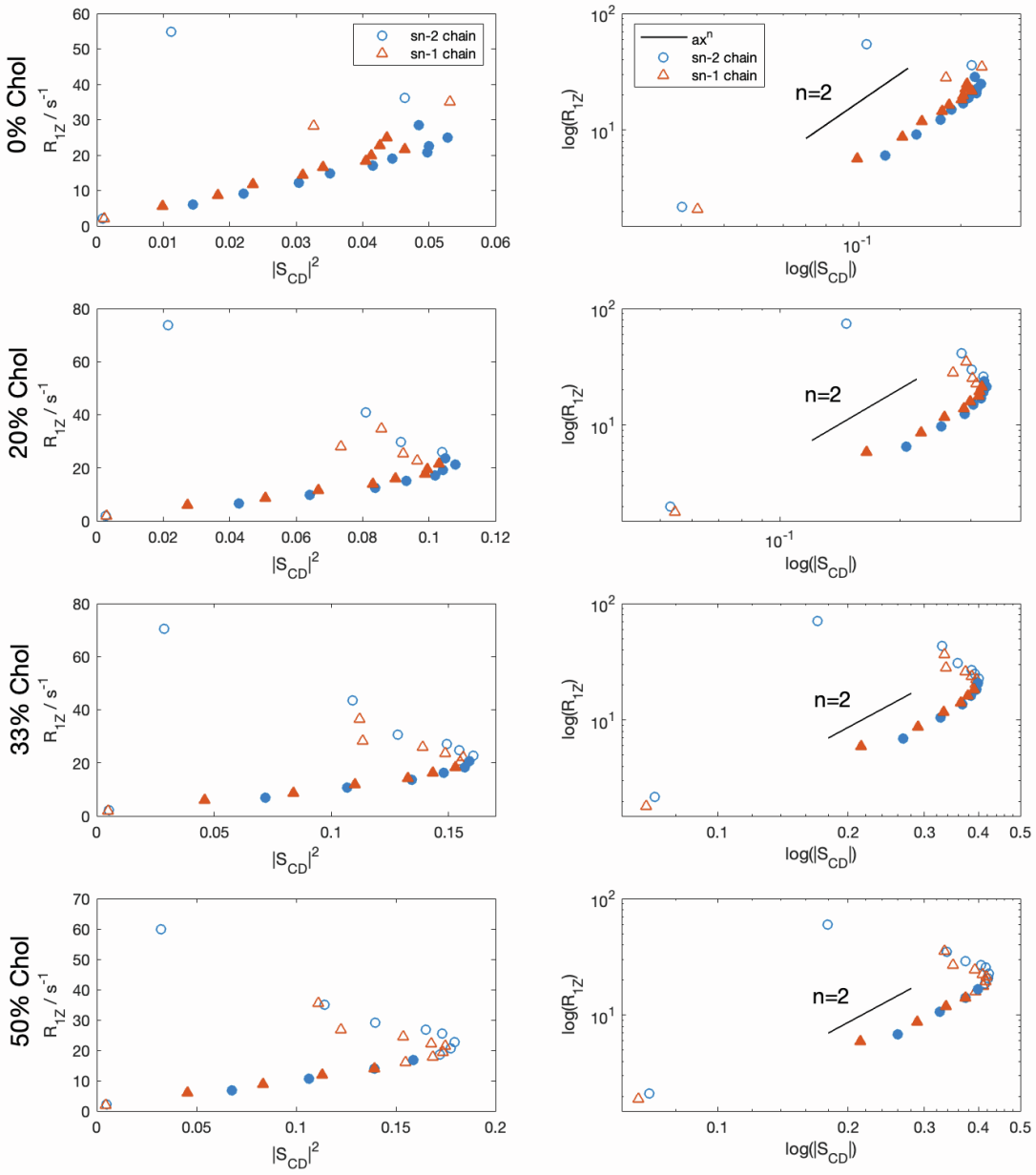

Figure S15. Relationship between spin-lattice relaxation rate R_{1Z} and order parameter $|S_{\mathrm{CD}}|$ for all carbons of DMPC in the simulated bilayers. Carbons on the *sn*-2 chain are shown as blue circles and on the *sn*-1 chain as red triangles. Filled symbols indicate the carbons from each chain that follow the square-law relationship as used in subsequent analysis of the apparent bilayer bending rigidity. On the left R_{1Z} is shown as a function of $|S_{\mathrm{CD}}|^2$ while on the right the log-log plot illustrates the model-free relationship between R_{1Z} and $|S_{\mathrm{CD}}|$ values. Also shown for comparison on these plots is a sample square-law function of the form ax^n with $n = 2$ in black. Note that the x- and y-axes of the plots are purposefully different to better illustrate the spread in the data.

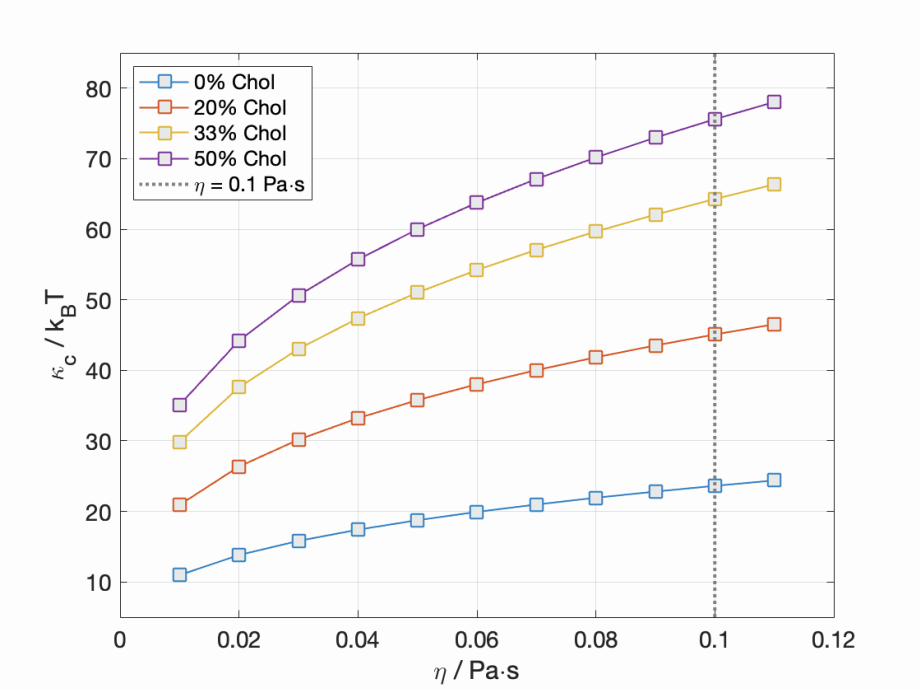

Figure S16. Effect of bilayer viscosity η on the apparent bending rigidity κ_C calculated from the slope of the square-law relationship (Eqs. 18, 19 of main text). The range for η was obtained from available estimates of η from experiments (4) and simulations (5).

Extended Methods

Neutron Spin Echo experiments

Suspensions of 100-nm unilamellar vesicles were prepared at a lipid concentration of 50 mg/mL, using standard vesicle extrusion methods (6). The samples were prepared by mixing protiated DMPC and cholesterol in chloroform at the required mole fractions. This step was followed by evaporation of chloroform under an inert gas stream and subsequent drying under vacuum overnight at 45 °C. The dry lipid films were then hydrated with 10 mM deuterated sodium phosphate buffer (prepared with D_2O instead of H_2O) at 45 °C with intermittent vortex mixing. The hydration of the lipid films at elevated temperature facilitates dispersion and promotes mixing of DMPC and cholesterol within the formed bilayers. The suspension was then subjected to at least 5 freeze/thaw cycles using a −80 °C freezer and a warm 45 °C water bath. The suspension was then extruded using an automated mini-extruder (Avanti Polar Lipids; Birmingham, AL) by passing the suspension 31 times through a polycarbonate filter (pore size = 100 nm). The extruder setup was heated to 45 °C during all extrusions. After extrusion, the samples were kept in a Peltier box at 45 °C until measured.

The NSE experiments were conducted on the NG-A NSE spectrometer at the NIST Center for Neutron Research (NCNR) over a q-range of 0.04 $Å^{-1}$ to 0.1 $Å^{-1}$, where $q = 4\pi \sin\theta/\lambda$ is the wavevector transfer defined by the neutron wavelength, λ, and the scattering, 2θ, measured relative to the incident beam. Measurements of the instrumental resolution and deuterated buffer were performed under the same configuration for data reduction and normalization. Data reduction was performed using the Data Analysis and Visualization Environment (DAVE) software developed at NIST (7).

Theoretical background: nuclear spin relaxation of lipid membranes

In general, the NMR spectra and relaxation times are governed by the Hamiltonian for coupling of the nuclear spins to the environment of the molecule or material. The main Hamiltonian is due to the Zeeman interaction of the nuclear magnetic moment with the applied external (static) magnetic field and will not be further discussed here. The smaller perturbing Hamiltonian contains the information of interest to chemists or physicists. It is due to the chemical shift, the direct (through space) magnetic dipolar interaction, the indirect (through bond or electron-mediated, spin-spin) dipolar coupling, and the electric quadrupolar coupling in the case of nuclei with a quadrupolar moment describing the non-spherical nuclear charge distribution. The perturbation is typically considered within the quantum-mechanical interaction picture.

Role of average Hamiltonian and correspondence to bilayer average structure. When motion is present, as in the case of liquid crystals, liquids, and even molecular solids, one must consider the average value of the perturbation and the fluctuating parts. The secular (time-independent part) part governs the lineshape, while the non-secular (time-dependent part) part governs the relaxation. Notably, the fluctuations of the Hamiltonian occur with respect to the mean value so that the fluctuating part is given by: $\widehat{H}_\lambda{}' = \widehat{H}_\lambda - \langle\widehat{H}_\lambda\rangle$, where $\lambda = \mathrm{Q}$ for the quadrupolar interaction in ^{2}H NMR spectroscopy. The time-independent average Hamiltonian is

secular; it commutes with the main Zeeman Hamiltonian and hence governs the NMR lineshape in accord with time-independent perturbation theory. Conversely, the averaged value of the Hamiltonian is non-zero and it must be subtracted to yield the fluctuating part that governs the relaxation. The fluctuating part is non-secular and affects the energy level transitions as considered by time-dependent perturbation theory.

Correspondence to experimental relaxation rates in NMR spectroscopy. Next, we apply time-dependent perturbation theory within the Redfield approximation (8). After transforming the principal values of the coupling (EFG) tensor from the molecule-fixed principal axis system (PAS) within the molecule to the laboratory frame, the irreducible correlation functions directly correspond to the Wigner rotation matrix elements. They read:

$$G_m^{\mathrm{lab}}(t) = \langle [D_{0m}^{(2)}(\Omega_{\mathrm{PL}}; t) - \langle D_{0m}^{(2)}(\Omega_{\mathrm{PL}})\rangle]^* \, [D_{0m}^{(2)}(\Omega_{\mathrm{PL}}; 0) - \langle D_{0m}^{(2)}(\Omega_{\mathrm{PL}})\rangle]\rangle \,, \qquad \text{(S1)}$$

where $D_{0m}^{(2)}(\Omega_{\mathrm{PL}})$ are the second-rank Wigner rotation matrix elements for the transformation from the molecule-fixed PAS to the laboratory frame in terms of Euler angles $\Omega_{\mathrm{PL}} \equiv (0, \beta_{\mathrm{PL}}, \gamma_{\mathrm{PL}})$ for transformation form the principal axis system (P) to the laboratory (L) frame (Fig. S1). The corresponding irreducible spectral densities of motion $J_m^{\mathrm{lab}}(\omega)$ are the Fourier transform partners of the $G_m^{\mathrm{lab}}(t)$ correlation functions:

$$J_m^{\mathrm{lab}}(\omega) = \mathrm{Re} \int_{-\infty}^{\infty} G_m^{\mathrm{lab}}(t) e^{-i\omega t} \, dt \,. \qquad \text{(S2)}$$

In the above formula $J_m^{\mathrm{lab}}(\omega)$ is a two-sided Fourier transform of the correlation function with limits of $(-\infty, +\infty)$. For more details the reader is referred to Refs. (9,10).

The relaxation rates in NMR spectroscopy correspond to various linear combinations of the irreducible spectral densities of motions $J_m(\omega)$ of the coupling Hamiltonian. In the case of solid-state ^{2}H NMR of lipid membranes, the spin-lattice relaxation rate ($R_{1\mathrm{Z}}$) and the quadrupolar order relaxation rate ($R_{1\mathrm{Q}}$) are of interest (8). The spin-lattice relaxation rate is given by:

$$R_{1\mathrm{Z}} = \frac{3}{4}\pi^2 \chi_{\mathrm{Q}}^2 \left[J_1^{\mathrm{lab}}(\omega_0) + 4 J_2^{\mathrm{lab}}(2\omega_0) \right] , \qquad \text{(S3)}$$

where $\chi_{\mathrm{Q}} \equiv e^2 qQ/h$ = 170 kHz is the static quadrupolar coupling constant (11). The value of the numerical pre-factor is thus $(3/4)\pi^2(1.70\ x\ 10^5)^2$ = $2.1392 \times 10^{11}\ s^{-2}$. The irreducible spectral densities of motion $J_m^{\mathrm{lab}}(\omega)$ are the Fourier transform partners of the $G_m^{\mathrm{lab}}(t)$ correlation functions (Eq. S1) and are directly connected to the observable relaxation rates in NMR spectroscopy.

Formulation of spherical-harmonic correlation functions and spectral densities. Furthermore, the Wigner rotation matrix elements are related to the well-known spherical harmonics by the following expression (derived from Eqs. 4.21, 4.30, and 4.31 from (12)):

$$D_{0m}^{(l)}(\chi, -\theta, -\phi) = \sqrt{\frac{4\pi}{2l+1}} \, Y_{lm}(\theta, \phi) \,, \qquad \text{(S4)}$$

in which l is the rank ($l = 2$ in the present case) and m is the projection of the angular momentum onto the axis of quantization. Note that $(\theta, \phi) = (\beta_{\mathrm{LP}}, \alpha_{\mathrm{LP}}) = (-\beta_{\mathrm{PL}}, -\gamma_{\mathrm{PL}})$ where the subscripts of the Euler angles denote forward rotation from the lab to the PAS frame (LP), or inverse rotation from the PAS to the lab frame, thus the negative angles (PL) (see Fig. S1). Accordingly, the correlation functions $G_m(t)$ of the second-rank Wigner rotation matrix elements are related to the spherical-harmonic correlation functions $\tilde{G}_m(t)$ for $l = 2$ by the relation: $G_m(t) = (4\pi/5)\,\tilde{G}_m(t)$, where the tilde on the right is to be noted. Here, the spherical-harmonic correlation functions read:

$$G_m(t) = \left(\frac{4\pi}{2l+1}\right)\tilde{G}_m(t)$$

$$= \left(\frac{4\pi}{2l+1}\right)\langle[Y_{lm}(\theta,\phi;t) - \langle Y_{lm}(\theta,\phi)\rangle]^*\,[Y_{lm}(\theta,\phi;0) - \langle Y_{lm}(\theta,\phi)\rangle]\rangle\,. \tag{S5}$$

The spherical-harmonic correlation functions $\tilde{G}_m(t)$ are often used in the literature (13-15) as an alternative to the Wigner rotation matrix correlation functions (9).

The two-sided spectral densities of the Wigner rotation matrix elements (Eq. S2) are then related to the one-sided spherical-harmonic spectral densities $\tilde{J}_m(\omega)$ with limits $(0, \infty)$ by: $J_m(\omega) = (8\pi/5)\,\tilde{J}_m(\omega)$, where the tilde on the right should again be noted. The spin-lattice relaxation rate formulated in terms of the spherical-harmonic spectral densities then becomes:

$$R_{1\mathrm{Z}} = \frac{3}{10}\pi\,\tilde{\chi}_{\mathrm{Q}}^2\left[\tilde{J}_1^{\mathrm{lab}}(\omega_0) + 4\tilde{J}_2^{\mathrm{lab}}(2\omega_0)\right], \tag{S6}$$

where $\tilde{\chi}_{\mathrm{Q}} = e^2qQ/\hbar = 2\pi\chi_{\mathrm{Q}}$ and we have also re-introduced the "lab" superscript. Note that the results using the spherical-harmonic correlation functions and spectral densities are obtained by substituting: $(3/4)\pi^2\chi_{\mathrm{Q}}^2 \rightarrow (3/10)\pi\tilde{\chi}_{\mathrm{Q}}^2$ and $J_m(\omega) \rightarrow \tilde{J}_m(\omega)$ where the tilde on the right is to be noted. Everything else is the same and it is just bookkeeping. The above formulas correspond to results found in the literature (14).

Use of closure to describe composite motions and multiple coordinate transformations. Next, as we have described above, it is necessary to separate the coupling Hamiltonian and correspondingly the correlation functions and spectral densities into the time-dependent and time-independent parts. The time-dependent part (nonsecular) governs the nuclear spin relaxation, while the time-independent part (secular) affects the spectral lineshape. The time dependence is expressed with respect to the director axis (the lamellar normal), while the time-independent part corresponds to the director orientation versus the laboratory axis system.

Accordingly, we can now separate the time-dependent and time-independent transformations using closure. We use closure to decompose the overall matrix elements with respect to the laboratory axes system into the time-dependent transformation with respect to the director frame, and the static or time-independent orientation of the director with respect

to the laboratory frame. Use of closure readily allows us to expand any Wigner rotation matrix element into a sequence of intermediate frame transformations, or equivalently to collapse a sequence of frame transformations into the appropriate rotation matrix element for the overall, i.e. composite, motion.

In the present case we focus on the separation of the overall transformation from the PAS of the molecule to the laboratory frame in two steps: first the transformation to the director frame (time-dependent), and second the transformation from the director frame to the laboratory system (time-independent). Because the Wigner rotation matrix elements are members of a group, the overall rotation can be expressed in terms of the other members of the group to read:

$$D_{0m}^{(2)}(\Omega_{\mathrm{PL}};t) = \sum_{p} D_{0p}^{(2)}(\Omega_{\mathrm{PD}};t)\, D_{pm}^{(2)}(\Omega_{\mathrm{DL}})\,. \tag{S7}$$

In the above formula $\Omega_{\mathrm{PD}}(t)$ are the time-dependent Euler angles for transformation from the principal axis system (P) of the molecule to the director (D) frame, and Ω_{DL} are the Euler angles for the static transformation from the director (D) to the laboratory (L) axis system.

Director-frame spectral densities versus laboratory-frame spectral densities. To make a comparison of the NMR relaxation times and order parameters to the results of MD simulations, we need to recognize that the time-dependent lipid fluctuations occur with respect to the frame of the director. This introduces a dependence on both the second-rank order parameter $\langle P_2 \rangle$ and the fourth-rank order parameter $\langle P_4 \rangle$ (9). Hence to compare the experimental NMR relaxation rates to the MD calculated values, we need to specify the director orientation with respect to the laboratory frame.

By applying closure (see above Eq. S7) to the overall correlation functions, and following the development through to the laboratory frame, we find that:

$$G_m^{\mathrm{lab}}(t) = \textstyle\sum_P \left| D_{0p}^{(2)}(\Omega_{\mathrm{DL}}) \right|^2 G_p^{\mathrm{dir}}(t)\,, \tag{S8}$$

where

$$G_p^{\mathrm{dir}}(t) = \langle [D_{0p}^{(2)}(\Omega_{\mathrm{PD}};t) - \langle D_{0p}^{(2)}(\Omega_{\mathrm{PD}})\rangle]^* \, [D_{0p}^{(2)}(\Omega_{\mathrm{PD}};0) - \langle D_{0p}^{(2)}\,(\Omega_{\mathrm{PD}})\rangle] \rangle\,. \tag{S9}$$

The director-frame correlation functions can also be written by subtracting the modulus-squared of the average value:

$$G_p^{\mathrm{dir}}(t) = \langle D_{0p}^{(2)*}(\Omega_{\mathrm{PD}};t) D_{0p}^{(2)}(\Omega_{\mathrm{PD}};0)\rangle - |\langle D_{0p}^{(2)}\,(\Omega_{\mathrm{PD}})\rangle|^2\,. \tag{S10}$$

Similarly, for the laboratory-frame spectral densities, upon Fourier transformation we find that:

$$J_m^{\mathrm{lab}}(\omega) = \sum_P \left| D_{0p}^{(2)}(\Omega_{\mathrm{DL}}) \right|^2 J_p^{\mathrm{dir}}(\omega)\,,$$

(S11)

where:

$$J_p^{\mathrm{dir}}(t) = \mathrm{Re} \int_{-\infty}^{\infty} \langle [D_{0p}^{(2)}(\Omega_{\mathrm{PD}};t) - \langle D_{0p}^{(2)}(\Omega_{\mathrm{PD}})\rangle]^* \, [D_{0p}^{(2)}(\Omega_{\mathrm{PD}};0) - \langle D_{0p}^{(2)}(\Omega_{\mathrm{PD}})\rangle] \rangle e^{-i\omega t} dt\,.$$

(S12)

In the above formulas the values of the Wigner rotation matrix elements $D_{0p}^{(2)}(\Omega_{\mathrm{PD}})$ can be found from the geometry of the system. The expressions for the Wigner rotation matrix elements are listed, e.g., in the Appendix of Ref. (11).

Orientational averaging of relaxation rates. In *randomly oriented* lipid membrane dispersions (so-called multilamellar vesicles or MLVs), the orientations where the director axis is perpendicular to the main magnetic field are most probable (because they correspond to the equator of the orientational probability distribution, where the area element is maximal). For *non-oriented* (powder-type) samples, in solid-state NMR spectroscopy, the $\theta = 90^\circ$ spectral edges (where $\theta \equiv \beta_{\mathrm{DL}}$) correspond to weak singularities (integrable) in the spectral orientational distribution function. They are the most prominent spectral features for which the relaxation rates are measured. However, because of lateral diffusion of the lipids in non-oriented powder-type distributions, i.e., multilamellar dispersions or MLVs, during the relaxation times (tens of milliseconds) the relaxation rates are averaged over all director orientations. Hence, the orientation dependence of the relaxation is suppressed, or averaged (16), and one can thus assume the orientationally averaged limit.

When the director changes its orientation rapidly compared to the relaxation times, the Wigner rotation matrix elements for the director–laboratory frame transformation are averaged over the various possible values. Orientational averaging of the director with respect to the laboratory frame is defined with respect to the spin-lattice relaxation times, which are typically in the range of ~50–100 ms or longer (17). In this case, the mean-square Wigner rotation matrix elements for the frame transformation are averaged to their isotropic values, leading to: $\langle |D_{0p}^{(2)}(\Omega_{\mathrm{PD}})|^2 \rangle = 1/5$. It follows that the dependence on the projection index (*m*) in the ***lab*** frame is lost due to the overall spherical symmetry. However, that does not imply the absence of a projection index (*p*) in the ***director*** frame. Quite to the contrary, the fluctuations are of limited amplitude with respect to the director as characterized by the orientational order parameters $\langle P_j(\beta_{\mathrm{PD}})\rangle$ where *j* = 2, 4 in the case of NMR spectroscopy.

Hence, in the orientationally averaged case (16), the spectral densities are:

$$J_m^{\mathrm{lab}}(\omega) = \langle J_m^{\mathrm{lab}}(\omega)\rangle \equiv J(\omega) = \frac{1}{5}\left[J_0^{\mathrm{dir}}(\omega) + 2J_1^{\mathrm{dir}}(\omega) + 2J_2^{\mathrm{dir}}(\omega)\right],$$

(S13)

where the dependence on the projection index (m) in the laboratory frame vanishes due to the spherical symmetry. The spin-lattice relaxation rates are thus:

$$R_{1Z} = \tfrac{3}{4}\pi^2\chi_Q^2\,[J(\omega_0) + 4J(2\omega_0)]\,. \qquad \text{(S14)}$$

Correspondence to molecular dynamics (MD) simulations. The director-frame spectral density functions $J_p^{\mathrm{dir}}(\omega)$ describe the internal motions within the membrane and afford a direct correspondence to the results of molecular dynamics (MD) simulations. Typically, one can assume that the NMR relaxation rates are orientationally averaged as described above (for either SUVs or MLVs). The final result appropriate to molecular dynamics (MD) simulations can then be written explicitly as:

$$\begin{aligned} R_{1Z} = \frac{3}{20}\pi^2\chi_Q^2\,\{&J_0^{\mathrm{dir}}(\omega_0) + 4J_0^{\mathrm{dir}}(2\omega_0) \\ &+2[J_1^{\mathrm{dir}}(\omega_0) + 4J_1^{\mathrm{dir}}(2\omega_0)] \\ &+2[J_2^{\mathrm{dir}}(\omega_0) + 4J_2^{\mathrm{dir}}(2\omega_0)]\}\,, \end{aligned} \qquad \text{(S15)}$$

where:

$$J_p^{\mathrm{dir}}(\omega) = \mathrm{Re}\int_{-\infty}^{\infty} G_p^{\mathrm{dir}}(t)e^{-i\omega t}\,dt\,, \qquad \text{(S16)}$$

and $G_p^{\mathrm{dir}}(t)$ is given by Eq. S9. The value of the numerical pre-factor is $(3/20)\pi^2(1.70\ x\ 10^5\ \mathrm{s}^{-1})^2 = 4.2785\ x\ 10^{10}\ \mathrm{s}^{-2}$.

The above correlation function decays to a zero value because the fluctuations occur about to the average values of the Winger rotation matrix elements. The director-frame correlation functions can also be written by subtracting the modulus-squared of the average value in which case $G_p^{\mathrm{dir}}(t)$ reads as in Eq. S10. For a cylindrically symmetric distribution the last term on the right of Eq. S10 becomes: $|\langle D_{0p}^{(2)}(\Omega_{\mathrm{PD}})\rangle|^2\delta_{0p}$ where δ_{0p} is the Kronecker delta function. In the correlation function the term on the left decays to a non-zero value as given by $|\langle D_{0p}^{(2)}(\Omega_{\mathrm{PD}})\rangle|^2$, which is then subtracted. These formulas lend themselves directly to molecular dynamics (MD) simulations.

Orientationally averaged relaxation rates in terms of spherical-harmonic spectral densities. For completeness, the results for the orientationally averaged relaxation rates can also be expressed in terms of the spherical-harmonic correlation functions (see above). Here we have the substitutions (see above): $(3/4)\pi^2\chi_Q^2 \rightarrow (3/10)\pi\tilde{\chi}_Q^2$ and $J_m(\omega) \rightarrow \tilde{J}_m(\omega)$ to obtain the equivalent results in terms of the spherical-harmonic correlation functions and spherical-harmonic spectral densities (indicated by the tilde on the right that is to be noted). Everything else is the same. The result is:

$$R_{1Z} = \frac{3}{50}\pi\tilde{\chi}_Q^2 \{\tilde{J}_0^{\mathrm{dir}}(\omega_0) + 4\tilde{J}_0^{\mathrm{dir}}(2\omega_0) + 2[\tilde{J}_1^{\mathrm{dir}}(\omega_0) + 4\tilde{J}_1^{\mathrm{dir}}(2\omega_0)] + 2[\tilde{J}_2^{\mathrm{dir}}(\omega_0) + 4\tilde{J}_2^{\mathrm{dir}}(2\omega_0)]\},$$

(S17)

where the tildes on the right are to be noted. The spherical harmonic-correlation functions are given by:

$$\tilde{G}_p^{\mathrm{dir}}(t) = \langle [Y_{2p}(\Omega_{\mathrm{PD}}; t) - \langle Y_{2p}(\Omega_{\mathrm{PD}})\rangle]^* \, [Y_{2p}(\Omega_{\mathrm{PD}}; 0) - \langle Y_{2p}(\Omega_{\mathrm{PD}})\rangle]\rangle \, .$$

.(S18)

In the above formula $\Omega_{\mathrm{PD}} = (0, \beta_{\mathrm{PD}}, \gamma_{\mathrm{PD}}) = (-\theta, -\phi)$ are now the angles (either Euler or spherical polar) for the transformation from the PAS to director frame which are isomorphous to those in Fig. S1. The director-frame correlation functions can also be written by subtracting the modulus-squared of the average value:

$$\tilde{G}_p^{\mathrm{dir}}(t) = \langle Y_{2p}^*(\Omega_{\mathrm{PD}}; t) Y_{2p}(\Omega_{\mathrm{PD}}; 0)\rangle - |\langle Y_{2p}(\Omega_{\mathrm{PD}})\rangle|^2 \, .$$

(S19)

where for a cylindrically symmetric distribution, the last term on the right becomes $|\langle Y_{2p}(\Omega_{\mathrm{PD}})\rangle|^2 \delta_{0p}$ where δ_{0p} is the Kronecker delta function. Note that Eqs. S20 and S21 are distinctly different from the correlation function obtained by application of the spherical-harmonic addition theorem (Eq. 22 in main text) which ignores the dependence on a director axis as illustrated in Fig. 8 *A* in the main text.

The results above (Eqs. S9, S15, and S16) should be used to compare MD simulations to the experimental NMR relaxation rates. In the case of MD simulations, the lipid bilayer exists as a patch while for experimental NMR studies it is the entire membrane. The lipid fluctuations are considered relative to the frame of the membrane patch, which we can assume is defined by the lamellar normal. The correlation functions correspond to the Wigner rotation matrix elements, which are listed in Ref. (11). To compare to the experimental NMR relaxation rates, the director-frame correlation functions are used together with the orientationally averaged results for the NMR spin-lattice relaxation rate, given above.

Notably, the correlation functions $G_p^{\mathrm{dir}}(t)$ and the spectral densities $J_p^{\mathrm{dir}}(\omega)$ in closed form can be factored into their mean-square amplitudes and reduced values as already indicated above. The reduced correlation functions can correspond to an exponential decay, power law, or stretched exponential decay as mentioned above, and correspondingly in the Fourier frequency domain for the reduced spectral densities. However, in the case of MD simulations the correlation functions and spectral densities are evaluated numerically. They can then be fit or tested against the simple analytical forms, both for validation and as a test of the closed-form theory.

Reduction to the isotropic solution NMR limit. Lastly, if one assumes unrestricted isotropic motion with a single correlation time, then the dependence on the projection index (*p*) due to

the molecular principal axis vanishes because of the spherical symmetry. Summing over all the reduced spectral densities leads to the well-known isotropic solution NMR result, which reads:

$$R_{1Z} = \frac{3}{20}\pi^2\chi_Q^2\left[j(\omega_0) + 4j(2\omega_0)\right].$$

(S20)

Here $j(\omega) = 2\tau_C/(1+\omega^2\tau_C^2)$ is a Lorentzian reduced spectral density for the molecular motions with τ_C as the single correlation time. Equivalently, the above result can be expressed using angular frequency units for the coupling constant and one-sided Lorentzian spectral densities, giving:

$$R_{1Z} = \frac{3}{40}\tilde{\chi}_Q^2\left[\tilde{j}(\omega_0) + 4\tilde{j}(2\omega_0)\right].$$

(S21)

where $\tilde{j}(\omega) = (1/2)j(\omega) = \tau_C/(1+\omega^2\tau_C^2)$ and where the invisible tilde is again to be noted. The numerical value of the prefactor is $(3/40)(4\pi^2)(1.70\ x\ 10^5\ s^{-1})^2 = 8.5570\ x\ 10^{10}\ s^{-2}$ as stated in Ref. (14). Note that compared to solid-state NMR results (see above), the solution NMR formulas consider unrestricted rotations of the molecule, i.e., in the absence of a director axis or orientational order parameters.

SI References

1. Venable, R. M., F. L. Brown, and R. W. Pastor. 2015. Mechanical properties of lipid bilayers from molecular dynamics simulation. *Chem. Phys. Lipids*. 192:60-74, doi: 10.1016/j.chemphyslip.2015.07.014, https://www.ncbi.nlm.nih.gov/pubmed/26238099.
2. Nagle, J. F. 2017. Experimentally determined tilt and bending moduli of single-component lipid bilayers. *Chem Phys Lipids*. 205:18-24, doi: 10.1016/j.chemphyslip.2017.04.006, https://www.ncbi.nlm.nih.gov/pubmed/28412174.
3. Fernandez-Puente, L., I. Bivas, M. D. Mitov, and Meleard, P. 1994. Temperature and Chain-Length Effects on Bending Elasticity of Phosphatidylcholine Bilayers. *Europhys Lett*. 28(3):181-186, doi: Doi 10.1209/0295-5075/28/3/005
4. Chakraborty, S., M. Doktorova, T. R. Molugu, F. A. Heberle, H. L. Scott, B. Dzikovski, M. Nagao, L. R. Stingaciu, R. F. Standaert, F. N. Barrera, J. Katsaras, G. Khelashvili, M. F. Brown, and R. Ashkar. 2020. How cholesterol stiffens unsaturated lipid membranes. *Proc. Natl. Acad. Sci. U.S.A.* 117(36):21896-21905, doi: 10.1073/pnas.2004807117, https://www.ncbi.nlm.nih.gov/pubmed/32843347.
5. Zgorski, A., R. W. Pastor, and E. Lyman. 2019. Surface Shear Viscosity and Interleaflet Friction from Nonequilibrium Simulations of Lipid Bilayers. *J. Chem. Theory Comput.* 15(11):6471-6481, doi: 10.1021/acs.jctc.9b00683, https://www.ncbi.nlm.nih.gov/pubmed/31476126.
6. Kumarage, T., J. Nguyen, and R. Ashkar. 2021. Neutron Spin Echo Spectroscopy as a Unique Probe for Lipid Membrane Dynamics and Membrane-Protein Interactions. *J Vis Exp*.(171), doi: 10.3791/62396, https://www.ncbi.nlm.nih.gov/pubmed/34125098.

7. Azuah, R. T., L. R. Kneller, Y. Qiu, P. L. Tregenna-Piggott, C. M. Brown, J. R. Copley, and R. M. Dimeo. 2009. DAVE: A Comprehensive Software Suite for the Reduction, Visualization, and Analysis of Low Energy Neutron Spectroscopic Data. *J Res Natl Inst Stand Technol*. 114(6):341-358, doi: 10.6028/jres.114.025, https://www.ncbi.nlm.nih.gov/pubmed/27504233.
8. Nevzorov, A., and M. Brown. 1997. Dynamics of lipid bilayers from comparative analysis of ^{2}H and ^{13}C nuclear magnetic resonance relaxation data as a function of frequency and temperature. *Chem. Phys.* 107(23):10288-10310, doi: 10.1063/1.474169
9. Brown, M. F. 1982. Theory of spin-lattice relaxation in lipid bilayers and biological membranes. ^{2}H and ^{14}N quadrupolar relaxation. *J. Chem. Phys.* 77(3):1576-1599, doi: 10.1063/1.443940
10. Brown, M. F. 1979. Deuterium relaxation and molecular dynamics in lipid bilayers. *J. Magn. Reson. (1969)*. 35(2):203-215, doi: 10.1016/0022-2364(79)90229-4
11. Molugu, T. R., S. Lee, and M. F. Brown. 2017. Concepts and Methods of Solid-State NMR Spectroscopy Applied to Biomembranes. *Chem. Rev.* 117(19):12087-12132, doi: 10.1021/acs.chemrev.6b00619, https://www.ncbi.nlm.nih.gov/pubmed/28906107.
12. Rose, M. E. 1995. Elementary theory of angular momentum. Courier Corporation.
13. Pastor, R. W., R. M. Venable, M. Karplus, and A. Szabo. 1988. A simulation based model of NMR T 1 relaxation in lipid bilayer vesicles. *J. Chem. Phys.* 89(2):1128-1140, doi: 10.1063/1.455219
14. Lindahl, E., and O. Edholm. 2001. Molecular dynamics simulation of NMR relaxation rates and slow dynamics in lipid bilayers. *Chem. Phys.* 115(10):4938-4950, doi: 10.1063/1.1389469
15. Yano, Y., S. Hanashima, T. Yasuda, H. Tsuchikawa, N. Matsumori, M. Kinoshita, M. A. Al Sazzad, J. P. Slotte, and M. Murata. 2019. Sphingomyelin Stereoisomers Reveal That Homophilic Interactions Cause Nanodomain Formation. *Biophysical journal*. 116(8):1575-1576, doi: 10.1016/j.bpj.2019.03.031, https://www.ncbi.nlm.nih.gov/pubmed/30955848.
16. Brown, M. F., and J. H. Davis. 1981. Orientation and frequency dependence of the deuterium spin-lattice relaxation in multilamellar phospholip1d dispersions: implications for dynamic models of membrane structure. *Chem. Phys. Lett*. 79(3):431-435, doi: 10.1016/0009-2614(81)85008-7
17. Leftin, A., and M. F. Brown. 2011. An NMR database for simulations of membrane dynamics. *Biochim Biophys Acta*. 1808(3):818-839, doi: 10.1016/j.bbamem.2010.11.027, https://www.ncbi.nlm.nih.gov/pubmed/21134351.